





Cite this: *Sustainable Energy Fuels*,  
2020, 4, 4902

Received 18th June 2020  
Accepted 20th July 2020

DOI: 10.1039/d0se00897d

rs.li/sustainable-energy

## Recent advances in vanadium-based nanomaterials and their composites for supercapacitors

Huizhen Qin,<sup>a</sup> Shunfei Liang,<sup>a</sup> Lingyun Chen,<sup>b</sup> \*<sup>a</sup> Yang Li,<sup>a</sup> Ziyang Luo<sup>a</sup>  
and Shaowei Chen \*<sup>b</sup>

In recent years, supercapacitors (SCs) have attracted considerable attention in the field of energy storage, and the design and engineering of effective electrode materials represent a critical part of research efforts. Consequently, vanadium(V)-based nanocomposites are of particular interest, primarily because V possesses a variety of valence states (*i.e.*, V<sup>2+</sup>, V<sup>3+</sup>, V<sup>4+</sup>, and V<sup>5+</sup>) and is cost efficient. In this review article, vanadium oxides, vanadium nitrides, vanadium sulfides, and mixed metal vanadates are primarily studied as V-based materials. Further, these compounds exhibit unique properties. In addition, recent advances in the preparation and electrochemical activity of V-based nanocomposites for SC applications are summarized with regard to synthesis methods, nanocomposite morphologies, and electrochemical performances. This review is concluded with a perspective, where promises and challenges of functional nanocomposites for SC applications are highlighted.

### 1 Introduction

The ever-increasing energy depletion and environmental deterioration issues have prompted researchers to conduct in-depth investigations into the development of new energy and environmentally benign energy storage systems. In recent years, with increasing progress in society, lithium-ion batteries have become the most widely used energy storage system due to their advantages of high energy density, long service life, no memory effect, and low cost.<sup>1</sup> However, lithium resources (used in lithium-ion batteries) are limited in nature. Developing innovative energy storage equipment as far as possible is the current research focus. Supercapacitors (SCs), also known as electrochemical capacitors, gold capacitors, and Faraday capacitors, are new type of energy storage devices with performances between those of batteries and plate capacitors. SCs, a new generation of energy storage equipment, have been broadly used in applications such as communication equipment, hybrid electric vehicles, and portable electronics, due to their high specific power (>10 kW kg<sup>-1</sup>), rapid charge/discharge capability (within seconds), long cycling lifetimes (>100 000 cycles), and environment-friendliness.<sup>2–4</sup> According to the charge storage mechanism, SCs can be classified into two categories: electrochemical double-layer capacitors (EDLCs) and pseudocapacitors (PCs) (which exhibit much higher capacitance). Mechanistically, charge/discharge arises from the adsorption/desorption of ions, respectively, at the electrode–

electrolyte interface in the former, whereas it is primarily due to faradaic redox reactions of the electroactive materials in the latter.<sup>5,6</sup> In addition, a hybrid capacitor, assembled with electrode materials of EDLCs and PCs, has also been proposed. Its energy storage mechanism is relatively complicated, and is generally considered to have the mechanisms of both EDLCs and PCs. The use of electroactive electrode materials with high surface area and redox-active mediators represents a critical strategy to enhance the capacitive performance, as the energy density ( $E$ ) of a SC depends on the capacitance ( $C$ ) as well as the operating potential window ( $V$ ), namely,  $E = 1/2CV^2$ .

To meet the ever-increasing demand for high-performance SCs, a range of electrode materials have been developed, such as oxides,<sup>7</sup> sulfides,<sup>8</sup> nitrides,<sup>9</sup> and tellurides of transition metals;<sup>10</sup> conductive polymers;<sup>11</sup> and carbon-based materials.<sup>12</sup> Their corresponding advantages and disadvantages are listed in Table 1. For example, Theerthagiri *et al.* discussed the recent progresses and emerging challenges in transition metal sulfides, and summarized the corresponding electrode materials for use in electrochemical supercapacitive energy storage.<sup>8</sup> Shi *et al.* emphasized on the current evolution of transition metal nitrides and transition metal nitrides/carbon nanocomposites.<sup>9</sup> As mentioned above, transition metal oxides (TMOs) as electrode materials in energy storage devices, particularly in SCs, have attracted great attention from researchers, such as RuO<sub>2</sub>, MnO<sub>2</sub>, Co<sub>3</sub>O<sub>4</sub>, and so on.<sup>13</sup> However, RuO<sub>2</sub> used in traditional TMOs has practical applications in SCs because of its low abundance, toxicity, and high cost. Therefore, the electrode materials for TMOs for wider use in SCs by researchers should have the advantages of high theoretical capacity, environment-friendliness, low cost, and abundant resources.

<sup>a</sup>School of Chemistry and Chemical Engineering, Chongqing University, Chongqing 400044, China. E-mail: lychen@cqu.edu.cn

<sup>b</sup>Department of Chemistry and Biochemistry, University of California, 1156 High Street, Santa Cruz, California 95060, USA. E-mail: shaowei@ucsc.edu

Table 1 Advantages and disadvantages of electrode materials for use in SCs

Materials	Advantage	Disadvantage
Metal nitride	Small resistance, high chemical stability and thermal stability, and low cost	Low specific capacity
Metal sulfide	Large electrical conductivity, mechanical and thermal durability, and high specific capacity	Poor stability
Metal telluride	High conductivity, and special physical and chemical properties	Complex synthesis
Carbon material	Large specific surface area, long cycle stability, high conductivity, and chemical stability	Low specific capacitance, large resistance
Conducting polymer	High conductivity	Poor stability
Traditional metal oxides	Great mechanical strength, high thermal and chemical stability, bio- and environmental compatibility, and flexible surface chemistry and architecture	High internal resistance and cost
V-based materials	Unique layered structure, various valence, low cost, and easy availability	Poor thermal stability

Vanadium(v) comprises about 0.02% of the earth's crust, and it is a widely distributed trace element. Due to the existence of multiple valence states of V, many materials exist in nature. For example, vanadium oxide has several forms, such as vanadium dioxide, vanadium trioxide, vanadium pentoxide, and so on. Further, most V-based materials are nontoxic or slightly toxic, and they are relatively cheap. Furthermore, V-based materials have been applied as electrode materials in SCs due to their different oxidation states. In addition, V-based materials, which have several merits, such as unique layered structure, low cost, easy availability, wide potential window, high energy density, and novel physical and chemical properties, are ideal as energy storage materials.

However, V-based materials are unstable during charging and discharging and can get easily converted into other substances, affording nonoptimal electrochemical and cycling performances. It is well known that the composition, crystal phase, and morphology of V-based materials have a significant influence on the electrochemical properties. Some effective approaches, such as elemental doping, metal/metal compound combination, use of carbon materials, use of conductive polymers, or nanostructure design, have been adopted to compensate for the aforementioned limitations of V-based materials. In addition, V-based materials have been extensively studied, and their synthesis methods include the hydrothermal method, coprecipitation, solvothermal method, sol-gel method, electrodeposition, chemical vapor deposition (CVD), electrospinning, spray drying, wet impregnation, and so on. This review discusses the current situation as well as the development of V-based materials in the future.

## 2 Crystal structures of V-based materials and corresponding electrochemical reactions

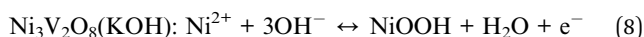
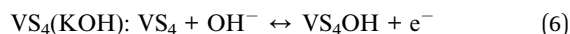
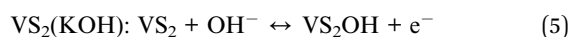
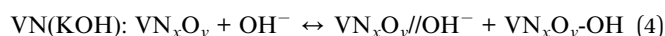
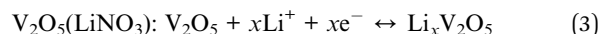
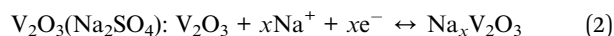
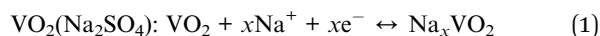
Vanadium(IV) dioxide (VO<sub>2</sub>) has different polymorphs, such as VO<sub>2</sub>(B), VO<sub>2</sub>(M), VO<sub>2</sub>(R), and VO<sub>2</sub>(A), which can be converted into each other at near room temperature. In VO<sub>2</sub>, the

transformation of the first-order monoclinic (M) insulator phase into the rutile (R) metallic phase was found, and its electrical and optical properties were considerably changed.<sup>14–16</sup> Fig. 1a shows the crystal structure of VO<sub>2</sub>(M) (space group *P2<sub>1</sub>/c* (no. 14)), with the unit cell parameters of  $a = 0.575$  nm,  $b = 0.452$  nm,  $c = 0.538$  nm, and  $\beta = 122.6^\circ$ ; further, for V–V bonds, the long distance is 0.312 nm and short space is 0.265 nm. The crystal structure of VO<sub>2</sub>(R) with the space group *P2<sub>1</sub>/m* (no. 136) is shown in Fig. 1b, and its cell parameters are as follows:  $a = b = 0.455$  nm,  $c = 0.286$  nm, and the distance between the nearest V–V atoms is 0.287 nm. The d electrons of each V atom in VO<sub>2</sub>(R) are bound to these V–V bonds, resulting in insulating properties. Vanadium(III) trioxide (V<sub>2</sub>O<sub>3</sub>) exhibits a rhombohedral corundum-type structure at ambient temperatures, due to the formation of three-dimensional (3D) V–V chains and a twisted octahedron composed of oxygen atoms around the V sites (Fig. 1f). Because V<sup>3+</sup> on the V<sub>2</sub>O<sub>3</sub> surface can be easily oxidized into V<sup>4+</sup> or V<sup>5+</sup> in air, V<sub>2</sub>O<sub>3</sub> shows low stability. Vanadium pentoxide (V<sub>2</sub>O<sub>5</sub>) can be crystallized, and it is another common oxide of V; it typically crystallizes into a layered structure, exhibiting an orthorhombic unit cell with the *Pmnm* space group and lattice constants of  $a = 1.1512$  nm,  $b = 1.3564$  nm, and  $c = 0.4368$  nm.<sup>17–21</sup> It consists of distorted VO<sub>5</sub> square pyramids periodically arranged up and down by sharing the edges and corners, as shown in Fig. 1e. Due to weak van der Waals forces, the layered structure can easily accommodate metal ions, a unique feature conducive for energy storage. In addition, Fig. 1d shows the structure of V<sub>2</sub>O<sub>5</sub>·*n*H<sub>2</sub>O with specific properties, which is different from V<sub>2</sub>O<sub>5</sub>.

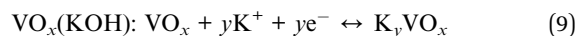
With regard to other V compounds, vanadium nitride (VN) is a cubic structure (space group *Fm $\bar{3}$ m* (225);  $a = 4.1328(3)$  Å;  $V = 70.588(9)$  Å<sup>3</sup>;  $Z = 4$ ) (Fig. 1c), and it has lower electronic conductivity than other transition metal nitrides.<sup>22–24</sup> Primary vanadium sulfides are VS<sub>2</sub> and VS<sub>4</sub>. VS<sub>2</sub> exhibits a layered structure and metallic conductivity.<sup>25</sup> VS<sub>2</sub> exhibits a two-dimensional (2D) sandwiched S–V–S layer with interlayer spacing of 0.576 nm (Fig. 1g).<sup>26</sup> VS<sub>4</sub> has a chain-like structure, where the V atom is bridged to S<sub>2</sub><sup>2–</sup>, as shown in Fig. 1h.<sup>27</sup> Co<sub>2</sub>V<sub>2</sub>O<sub>8</sub> as well as Ni<sub>2</sub>V<sub>2</sub>O<sub>8</sub> exhibit an orthorhombic structure

with somewhat different cell parameters:  $a = 8.24 \text{ \AA}$ ,  $b = 11.38 \text{ \AA}$ , and  $c = 5.906 \text{ \AA}$  for the former, and  $a = 8.3 \text{ \AA}$ ,  $b = 11.50 \text{ \AA}$ , and  $c = 6.030 \text{ \AA}$  for the latter.<sup>28</sup>

When used as a SC electrode, these materials can undergo electrochemical reactions in different electrolytes, as listed below (Fig. 1i shows the reactions of  $\text{VO}_2$ ):



During electrochemical tests, V-based materials (vanadium oxides or VNs) may get oxidized or dissolved into an oxide in the aqueous electrolyte, and these oxides are represented as  $\text{VO}_x$ . The possible electrochemical reactions are as follows:



In order to prevent the dissolution or oxidation of V-based materials, various strategies have been proposed: (1) synthetic composites, that is, nanostructured materials synthesized with carbon materials and/or conductive polymers; (2) gel electrolytes; and (3) adding a layer of protective film (carbonaceous thin film).

However, the electrochemical reaction of V-based materials in SCs is similar to those in batteries, and they can be easily confused. In fact, their reaction mechanism is completely different. In SCs, the highly reversible faradaic reaction stores charge on or near the surface of the electrode active material, that is, the electrode material does not undergo a phase change. In batteries, the active electrode or ions in the electrolyte react reversibly to store and release charge. In other words, SCs necessitate delocalized electron transfer, and the battery behavior entails valence electron transfer.<sup>29</sup>

## 3 Syntheses

The syntheses of V-based materials depend on the required morphology and structure. Various synthesis techniques have been developed to meet the preparation needs of materials. We mainly introduce several commonly used synthesis methods.

### 3.1 Hydrothermal and solvothermal methods

The hydrothermal method involves the dissolving and recrystallizing of insoluble substances at high temperatures and high pressures in a closed reaction container with an aqueous solution as the reaction medium.<sup>19</sup> The reaction conditions can be

adjusted to control the crystal structure, crystal morphology, and crystal purity of the materials. When compared with other methods, the main differences are in the temperature (130–250 °C) and pressure (0.3–4 MPa). The solvothermal technique, similar to the hydrothermal method, involves the reaction of the raw materials in a closed system at a certain temperature and pressure. The biggest difference between the two methods is that the solvent in the hydrothermal method is water, and the solvothermal method is an organic solvent or nonaqueous solvent.<sup>30</sup> Most V-based materials can be fabricated by the hydrothermal method, such as  $\text{VO}_2$  nanosheets,<sup>31</sup>  $\text{VO}_2(\text{B})$  hollow spheres,<sup>32</sup>  $\text{V}_2\text{O}_3@C$  core-shell nanorods,<sup>33</sup> porous VN nanowires (NWs),<sup>34</sup>  $\text{NiCo}_2\text{S}_4@V\text{S}_2$ ,<sup>35</sup> and  $\text{Co}_3\text{V}_2\text{O}_8\text{-Ni}_3\text{V}_2\text{O}_8$  nanocomposites.<sup>36</sup> Some of them can be synthesized by the solvothermal technique.

### 3.2 Sol-gel method

The sol-gel method is a low-temperature wet chemistry method, in which the raw materials are uniformly mixed to synthesize new materials (metal oxides); here, the chemical solution is initially converted into a sol and then into a gel.<sup>37</sup> Generally, the typical raw materials that include metal alkoxides and metal chlorides are mixed in the liquid phase and the mixture undergoes hydrolysis and condensation reactions, forming a stable, transparent sol system. After aging, a gel with a 3D network structure is formed. In this method, metal oxides can be fabricated by connecting metal centers to oxo (M–O–M) or hydroxo (M–OH–M) to generate metal-oxo or metal-hydroxo polymers. Then, the polymer is deposited on the substrate to form a specific structure. Kiruthiga *et al.* successfully prepared  $\text{V}_2\text{O}_5@r\text{GO}$  nanorods by combining  $\text{V}_2\text{O}_5$  obtained by the sol-gel method and rGO obtained by the modified Hummers' method.<sup>38</sup> Wu *et al.* were the first to synthesize  $\text{V}_2\text{O}_5$  sol; then, an aqueous dispersion of multi-walled carbon nanotubes (MWCNTs) was added to this sol to afford 3D  $\text{V}_2\text{O}_5/\text{MWCNTs}$  hybrid aerogel.<sup>39</sup>

### 3.3 CVD

CVD is a common industrial method in which one or more volatile precursors react and/or decompose in the gas phase or at the gas–solid interface, thereby generating deposits.<sup>40</sup> There are different types of CVDs, namely, atmospheric-pressure, low-pressure, ultrahigh-vacuum, laser, metal-organic, and plasma-enhanced CVDs. Further, the techniques with gases at different pressures and specific flows have been successfully applied to various fields. Many scientists have devoted themselves toward the development of high-quality materials by CVD, and they have found the following main factors: (1) selection of the partial pressure of the reaction mixture and its relative ratio; (2) deposition temperature; (3) substrate material; (4) total pressure and total gas flow rate in the system; (5) devices for the reaction gas (sealing, reaction tube, gas pipeline material, *etc.*); and (6) purity of raw materials. The CVD technique for fabricating V-based materials that are based on organometallic precursors is called organometallic CVD or metal-organic CVD. Basu *et al.* reported the formation of a nanoporous structure of  $\text{VO}_2$  using carbon paper (an open mesh of carbon fibers (CFs)) as the substrate for different Ar flows.<sup>41</sup> VN-graphene foams were reported by Yu

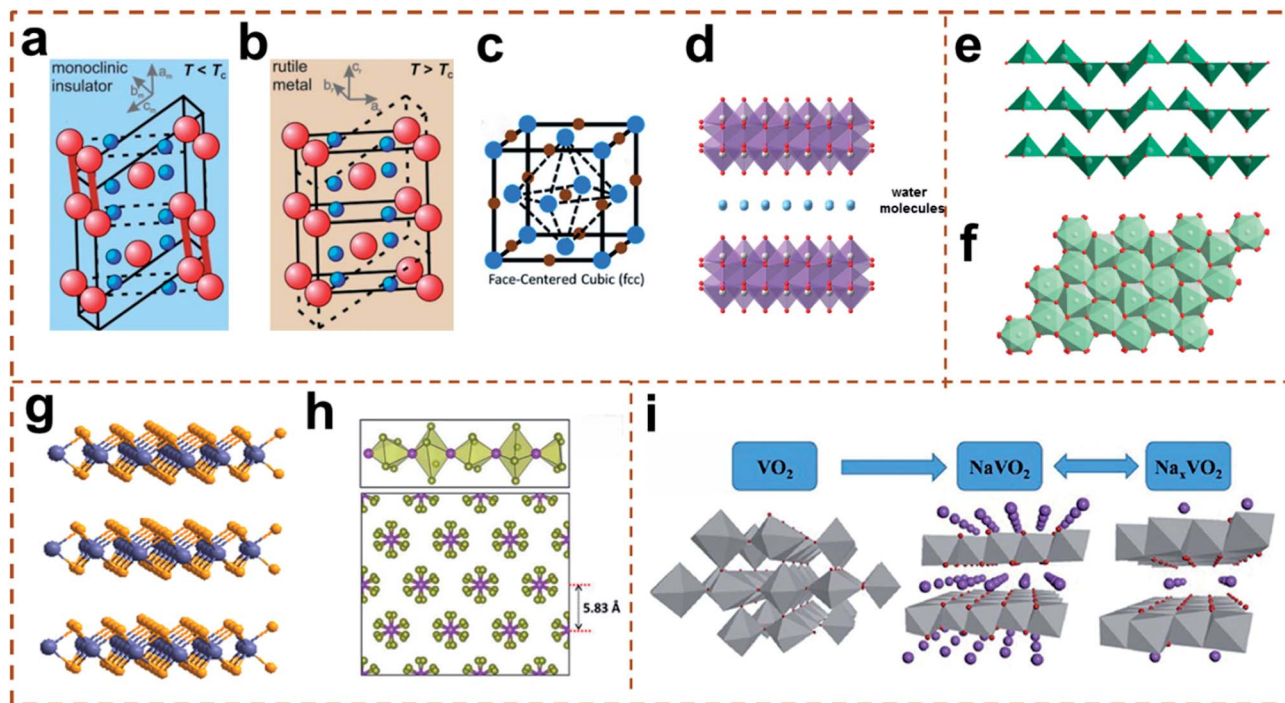


**Fig. 1** (a) Monoclinic insulator in the  $\text{VO}_2$  crystal structure. (b) Rutile metal. (c) Common crystal structures in VN compounds. (d) Crystal structures of  $\text{V}_2\text{O}_5 \cdot \text{H}_2\text{O}$ . (e)  $\text{V}_2\text{O}_5$ . (f)  $\text{V}_2\text{O}_3$ . (g)  $\text{VS}_2$ . (h) Schematic illustration of the chain-like structure of  $\text{VS}_4$ . (i) Schematic illustration of the sodium storage mechanisms of  $\text{VO}_2(\text{B})$ . (a and b) Reprinted with permission.<sup>16</sup> Copyright 2015, Elsevier. (c) Reprinted with permission.<sup>24</sup> Copyright 2016, Wiley-VCH. (g and h) Reprinted with permission.<sup>27</sup> Copyright 2013, American Chemical Society. (i) Reprinted with permission.<sup>14</sup> Copyright 2014, Elsevier.

*et al.*;<sup>42</sup> here, the graphene synthesized *via* the CVD technique used Ni foam as the growth substrate and methane as the carbon source and employed the following gas flow recipe:  $\text{CH}_4$  (30 standard cubic centimeter per minute (sccm)),  $\text{H}_2$  (50 sccm), and Ar (150 sccm) under ambient pressure at 1000 °C for 30 min.

### 3.4 Electrospinning method

Electrospinning technology is a continuous and universal method to fabricate superfine fibers below the micron level. An electrospinning device mainly comprises three sections: a high-voltage DC power supply, a spinning device, and the target electrode. The power supply provides high voltage for the high-power stretching of the charged polymer. The as-prepared fibers have small diameter, large specific surface area, high porosity, and consistent fineness. Therefore, electrospinning technology plays an important role in biomedical materials, filtration and protection, catalysis, energy, optoelectronics, food engineering, cosmetics, and other fields. In addition, it can also be used for the preparation of V-based materials (such as  $\text{V}_2\text{O}_5$  nanofibers<sup>43</sup> and VN nanofibers<sup>34</sup>).

## 4 Vanadium oxide

### 4.1 $\text{VO}_2$ and its composite materials

**4.1.1  $\text{VO}_2$  materials.** In the past few decades,  $\text{VO}_2(\text{B})$ , as a promising material for use in SCs, has attracted considerable interest than the other polymorphs ( $\text{VO}_2(\text{M})$ ,  $\text{VO}_2(\text{R})$ , and

$\text{VO}_2(\text{A})$ ) due to its peculiar optical and electrical properties. However, its performance is limited because of its low rate capability and cycling stability; these can be improved using two strategies. First, the structure of the materials can be deliberately engineered. Zhang *et al.* developed a template-free method to prepare a 3D  $\text{VO}_2(\text{B})$  solid sphere, which was then converted into hollow spherical cages by hydrothermal and calcination treatments.<sup>32</sup> As electrode materials,  $\text{VO}_2(\text{B})$  hollow cages exhibited specific capacitance of  $1175 \text{ mF cm}^{-2}$  ( $336 \text{ F g}^{-1}$ ), which was apparently higher than that of its solid counterpart ( $951 \text{ mF cm}^{-2}$ ,  $272 \text{ F g}^{-1}$ ) at  $2 \text{ mA cm}^{-2}$ . Further,  $\text{VO}_2(\text{B})$  hollow spheres exhibited enhanced stability, with 68% capacitance retention after 10 000 cycles as compared to only 49% for the solid spheres. Using the same method to synthesize different morphologies of  $\text{VO}_2$  is helpful to compare which morphology can increase the ion-accessible area, reduce the ion transmission resistance, and improve the electrochemical performance. Ndiaye *et al.* prepared  $\text{VO}_2$  with different morphologies (nanospheres and nanosheets) by a solvothermal method for different periods of time, *i.e.*, 2.5, 4, 6, and 12 h, at a temperature of 200 °C.<sup>44</sup>  $\text{VO}_2(\text{A})$  samples prepared at 2.5 and 12 h revealed a yolk-shell structure with a less dense interior, whereas  $\text{VO}_2(\text{B})$  samples prepared at longer hydrothermal times of 4 and 6 h exhibited a double-shell structure. In electrochemical tests comprising a three-electrode cell using 6 M KOH aqueous electrolyte, the resulting  $\text{VO}_2(\text{B})$  nanosheets (6 h) possessed a higher specific discharge capacity than those of the

other samples, with a specific capacitance of  $663 \text{ F g}^{-1}$  at a scan rate of  $5 \text{ mV s}^{-1}$  and excellent cycling stability after 5000 cycles at a current density of  $10 \text{ A g}^{-1}$ . This shows that nanosheets have a higher research value than nanospheres.

One of the unique properties of 2D nanosheets is their large specific surface area, which reduces the ion diffusion path and can effectively carry out the redox reaction. Rakhi *et al.* prepared  $\text{VO}_2$  nanosheets (lateral dimensions in the range of 60 nm to 2 mm) and investigated their electrochemical behaviors in an organic gel electrolyte (1 M  $\text{LiClO}_4$  in propylene carbonate (PPC)).<sup>31</sup> Then, ultrathin nanosheets were used to fabricate electrodes for use in SCs by drop-casting a suspension of  $\text{VO}_2$  nanosheets, conducting carbon, and sodium carboxymethylcellulose (CMC) binder in water onto carbon paper, as shown in Fig. 2a, which afforded specific capacitance of about  $405 \text{ F g}^{-1}$  at a current density of  $1 \text{ A g}^{-1}$ . The  $\text{VO}_2$ -based organic symmetric capacitor retained nearly 82% of its maximum capacitance (more than 95% of the initial capacitance) even after 6000 charge/discharge cycles. Ndiaye *et al.* developed a solvothermal method for the large-scale production of polycrystalline, monoclinic  $\text{VO}_2$  nanosheets and used these materials to assemble an asymmetric SC (ASC) with the structure of carbonized iron-polyaniline (C-FP)/6 M  $\text{KOH}/\text{VO}_2$ , which exhibited a specific capacity of  $47 \text{ mA h g}^{-1}$  and specific energy of  $30 \text{ W h kg}^{-1}$  with corresponding specific power density of

$713 \text{ W kg}^{-1}$  at a gravimetric current density of  $1 \text{ A g}^{-1}$  in the potential window of 1.6 V.<sup>45</sup> Meanwhile, the development of porous materials is a trend in energy storage research. Nanosheets have high research value; at the same time, it is important to emphasize the diverse morphologies in the experimental process; therefore, investigating only nanosheets should be avoided.

Moreover,  $\text{VO}_2$  thin film, a nanostructured semiconductor film, possesses novel physical and chemical properties and is suitable for various new applications. Basu *et al.* prepared monoclinic thin films of  $\text{VO}_2$  nanorods *via* the CVD technique and coated a porous structure of  $\text{VO}_2$  on CF.<sup>41</sup> Field-emission scanning electron microscopy (FESEM) analysis revealed a porous structure in the obtained thin films with an average pore diameter of approximately 200 nm (Fig. 2b and c). Electrochemically, the  $\text{VO}_2$  arrays exhibited specific capacitance of  $20.7 \text{ mF cm}^{-2}$  at a current density of  $0.3 \text{ mA cm}^{-2}$ , capacitance retention of 93.7%, and coulombic efficiency of 98.2% for 5000 charge/discharge cycles. This suggests excellent rate capability, reversibility, and durability. Reddy *et al.* employed radiofrequency-reactive magnetron sputtering to deposit thin films of monoclinic  $\text{VO}_2(\text{M})$  nanorods onto indium tin oxide (ITO)-coated glass substrates at  $300 \text{ }^\circ\text{C}$  and under various  $\text{O}_2$  flow rates ranging from 2 to 6 sccm.<sup>46</sup> The film coated on the ITO-coated glass substrates were treated at a substrate

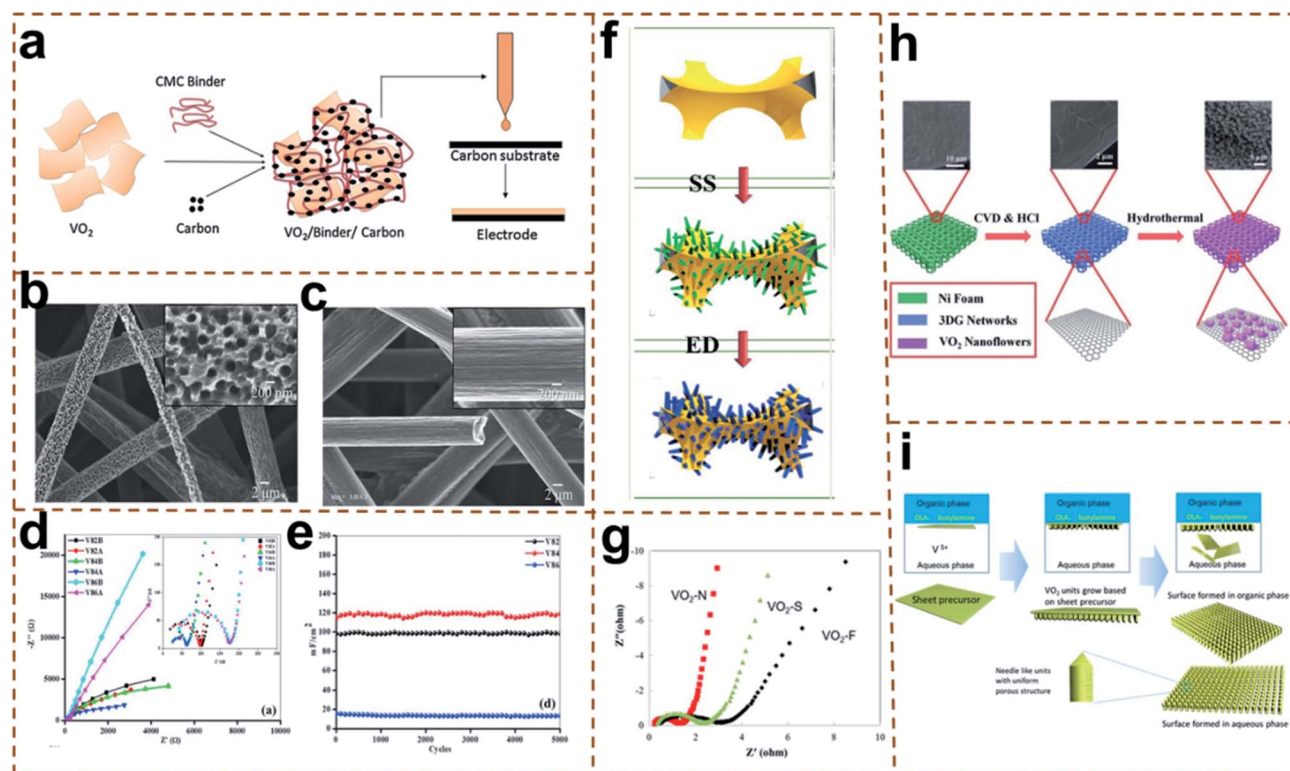


Fig. 2 (a) Schematic of the preparation of a  $\text{VO}_2$  nanosheet electrode with a CMC binder on graphitized carbon paper. (b) SEM image of a  $\text{VO}_2$  nanoporous structure grown on carbon paper. (c) Bare CF. (d) Nyquist plots of  $\text{VO}_2$  thin films. (e) Specific capacitance vs. number of cycles at a constant scan rate of  $100 \text{ mV s}^{-1}$ . (f) Schematic illustration of the fabrication of GF-supported  $\text{VO}_2$ /HMB. (g) EIS spectra of 2D  $\text{VO}_2$  microarrays. (h) Schematic diagram of the preparation of  $\text{VO}_2$  NF@3DG hybrid. (i) Illustration of the formation process of 2D  $\text{VO}_2$  mesoporous microarrays. (a) Reprinted with permission.<sup>31</sup> Copyright 2016, Elsevier. (b and c) Reprinted with permission.<sup>41</sup> (d and e) Reprinted with permission.<sup>46</sup> Copyright 2019, Elsevier. (f) Reprinted with permission.<sup>55</sup> Copyright 2015, The Royal Society of Chemistry. (g and i) Reprinted with permission.<sup>56</sup> Copyright 2017, Nano Express. (h) Reprinted with permission.<sup>52</sup> Copyright 2017, The Royal Society of Chemistry.

Table 2 Comparison of various types of VO<sub>2</sub> and its nanocomposites as electrode materials for use in SCs

Nano-structures (dimension)	Synthetic method	Electrolyte	Potential window (V)	Maximum SC	Current density	Cycling stability (%)	Ref.
VO <sub>2</sub> -6 h nanosheets (2D)	Solvothermal method	6 M KOH	0.0–0.5	663 F g <sup>-1</sup>	5 mV s <sup>-1</sup>	99.4% (9000 cycles)	44
VO <sub>2</sub> nanosheet (2D)	Hydrothermal method	1 M LiClO <sub>4</sub> /PPC	–0.3–1.1	405 F g <sup>-1</sup>	1 A g <sup>-1</sup>	82% (6000 cycles)	31
VO <sub>2</sub> monoclinic nanosheets (2D)	Solvothermal method	6 M KOH	0.0–0.5	47 mA h g <sup>-1</sup>	1 A g <sup>-1</sup>	89% (10 000 cycles)	45
Monoclinic VO <sub>2</sub> nanorod thin films (2D)	Radio-frequency reactive magnetron sputtering	0.1 M NaOH	0.0–0.8	486 mF cm <sup>-2</sup>	10 mV s <sup>-1</sup>	100% (5000 cycles)	46
VO <sub>2</sub> nanoporous structure (2D)	CVD technique.	Na <sub>2</sub> SO <sub>4</sub>	0.0–0.5	20.7 mF cm <sup>-2</sup>	0.3 mA cm <sup>-2</sup>	93.7% (5000 cycles)	41
VO <sub>2</sub> (B) hollow spheres (3D)	Hydrothermal method	1 M Na <sub>2</sub> SO <sub>4</sub> /CMC	–0.5–1.0	336 F g <sup>-1</sup>	2 mA cm <sup>-2</sup>	68% (10 000 cycles)	32
VO <sub>2</sub> (B)/C core-shell composites	Hydrothermal method	1 M Na <sub>2</sub> SO <sub>4</sub>	–0.6–0.8	203 F g <sup>-1</sup>	0.2 A g <sup>-1</sup>	10.4% (100 cycles)	51
VO <sub>2</sub> NFs@3DG	CVD-hydrothermal method	0.5 M K <sub>2</sub> SO <sub>4</sub>	–0.6–0.6	507 F g <sup>-1</sup>	3 mA cm <sup>-2</sup>	63.5% (3000 cycles)	52
VO <sub>2</sub> (B) nanobelts/rGO composite	Hydrothermal method	0.5 M K <sub>2</sub> SO <sub>4</sub>	–1.0–0.0	353 F g <sup>-1</sup>	1 A g <sup>-1</sup>	78% (10 000 cycles)	53
VO <sub>2</sub> nanoparticle/EOGF	Hydrothermal method	5 M LiCl	0.0–0.8	119 mF cm <sup>-2</sup>	2 mV s <sup>-1</sup>	70% (1500 cycles)	54
GF + VO <sub>2</sub> /HMB	The chemical vapour deposition method	1 M K <sub>2</sub> SO <sub>4</sub>	–0.3–1.5	485 F g <sup>-1</sup>	2 A g <sup>-1</sup>	97.5% (5000 cycles)	55
Hydrogen treated VO <sub>2</sub>	Thermal treatment method	1 M Na <sub>2</sub> SO <sub>4</sub>	0.0–0.8	300 F g <sup>-1</sup>	1 A g <sup>-1</sup>	96% (1000 cycles)	57
VO <sub>2</sub> -N microarray	An organic–inorganic liquid interface	1 M Na <sub>2</sub> SO <sub>4</sub>	0.0–0.6	265 F g <sup>-1</sup>	1 A g <sup>-1</sup>	100% (3000 cycles)	56

temperature of 300 °C and various O<sub>2</sub> flow rates ranging from 2 to 6 sccm. The thin films of VO<sub>2</sub>(M) nanorods prepared at the flow rate of 6 sccm revealed specific capacitance of ~486 mF cm<sup>-2</sup> at the scan rate of 10 mV s<sup>-1</sup>, and the specific capacitance remained virtually invariant at ~118 mF cm<sup>-2</sup> after 5000 cycles at the scan rate of 100 mV s<sup>-1</sup>. In addition, the sample grown at the argon/oxygen flow ratio of 8 : 4 (V84, Fig. 2d) exhibited low resistance and excellent cycling stability (Fig. 2e). The electrochemical properties of the same morphology synthesized by means of different methods are completely different, which is mainly due to the differences in the specific surface area and pore size. This mainly affects the ion transport path.

Different morphologies can be synthesized by using the same method or the same morphology can be synthesized by using different methods (Table 2); in all of this, the contact area and ion transmission channel between the electrode materials and electrolyte are primarily changed, thereby improving the electrochemical performances.

**4.1.2 VO<sub>2</sub> hybrid materials.** Second, functional nanocomposites can be fabricated to improve the electrochemical performance of VO<sub>2</sub> materials (Table 2). Mainly, the pseudocapacitance is increased, ion-accessible area is increased, and ion transmission resistance is decreased. Carbon materials (graphene, activated carbon, and carbon nanotubes (CNTs)/carbon nanofibers (CNFs)) have been proven to be good electrode materials for use in SCs due to their excellent chemical stability, low cost, high power density, and long cycling life. Further, they are often used as a substrate for materials used in energy storage, such as VO<sub>2</sub>/carbon onion hybrid materials,<sup>47</sup> Fe<sub>3</sub>O<sub>4</sub>/carbon nanocomposites,<sup>48</sup> RuO<sub>2</sub>/rGO nanocomposites,<sup>49</sup> and rGO/beta-Cu<sub>2</sub>V<sub>2</sub>O<sub>7</sub>/TiO<sub>2</sub> nanorods composites.<sup>50</sup> A combination of VO<sub>2</sub> and carbon materials can compensate for the disadvantages of low conductivity and poor cycling stability of VO<sub>2</sub>, as well as prevent its agglomeration and improve its electrical conductivity. Zhang *et al.* prepared a VO<sub>2</sub>(B) and carbon core-shell structure by a facile hydrothermal method. When tested as the electrodes for use in SCs, these VO<sub>2</sub>(B)/C core-shell composites exhibited specific capacitance of 203 F g<sup>-1</sup> at a current density of 0.2 A g<sup>-1</sup> and an excellent energy density of 198.9 W h kg<sup>-1</sup> at a power density of 504.5 W kg<sup>-1</sup>.<sup>51</sup> However, the cycling stability of these VO<sub>2</sub>(B)/C core-shell composites was poor in 1 M Na<sub>2</sub>SO<sub>4</sub> aqueous solutions.

Lightweight and high-conductivity graphene materials facilitate the transport of electrons and ions and enhance the electrochemical performance. Highly porous and highly stable VO<sub>2</sub> NF@3DG hybrids comprising VO<sub>2</sub> nanoflowers (NFs) grown on 3D graphene (3DG) networks were prepared by Wang *et al.*<sup>52</sup> The synthesis of these hybrids is shown in Fig. 2h. The mass of the VO<sub>2</sub> NFs on 3DG was around 0.91 mg cm<sup>-2</sup>, and 3DG had a mass density of 8.22 mg cm<sup>-2</sup> after the hydrothermal reaction. VO<sub>2</sub> NF@3DG hybrid electrodes were found to exhibit large specific capacitance of 466 mF cm<sup>-2</sup> and capacitance retention of 63.5% after 3000 cycles in 0.5 M K<sub>2</sub>SO<sub>4</sub> aqueous electrolyte. Furthermore, VO<sub>2</sub> NF@3DG hybrids provided high energy density (279.6 mW h m<sup>-2</sup>) and high power density (60 000 mW m<sup>-2</sup>). Lv *et al.* utilized a simple method to prepare VO<sub>2</sub>(B) nanobelts/rGO composites with a porous framework.<sup>53</sup>

Combining the amorphous structure of rGO with VO<sub>2</sub> nanobelts is beneficial to improve the stability of VO<sub>2</sub> in electrochemical measurements. When tested as the electrode of all-solid-state symmetrical SCs (SSCs), this composite was measured with a three-electrode system in a 0.5 M K<sub>2</sub>SO<sub>4</sub> aqueous solution as the electrolyte. The electrochemical impedance spectroscopy (EIS) data showed that the resistance of VO<sub>2</sub>/rGO was smaller when compared with that of the VO<sub>2</sub> nanobelts, which implied that the VO<sub>2</sub>/rGO composites had a highly interconnected porous structure and could easily diffuse electrolyte ions and electrons. For the assembled all-solid-state SSC, the VO<sub>2</sub>/rGO composites exhibited good energy storage performance with a power density of 7152 W kg<sup>-1</sup> at an energy density of 3.13 W h kg<sup>-1</sup>. After 10 000 cycles, the specific capacitance retention was 78% at 10 A g<sup>-1</sup>.

More importantly, edge-oriented graphene foam (EOGF) is a continuous conductive frame for growing graphene on Ni foam by the CVD method, which can minimize the ion diffusion length, increase the electrolyte–electrode interface, and provide a fast electron conduction path as well as strong mechanical support. Ren *et al.* synthesized VO<sub>2</sub> nanoparticles/EOGF composites to enhance the specific capacitance.<sup>54</sup> The electrochemical performance was investigated by cyclic voltammetry (CV) measurements, which showed a desirable quasi-rectangular profile due to the high rate capability arising from the synergistic effect of EOGF and VO<sub>2</sub> nanoparticles. The VO<sub>2</sub>/EOGF electrode exhibited capacitance of 119 mF cm<sup>-2</sup> at a scan rate of 2 mV s<sup>-1</sup>, about two orders of magnitude higher than that of bare EOGF. At a high scan rate of 1000 mV s<sup>-1</sup>, capacitance of 26 mF cm<sup>-2</sup> could be obtained and capacitance retention of 70% could be achieved after 1500 cycles.

Hydrogen molybdenum bronze (HMB) is not only an n-type semiconductor with high electrical conductivity (10<sup>3</sup> to 10<sup>5</sup> S m<sup>-1</sup>) but also a fast ionic conductor with ionic conductivity of 0.001–0.01 S m<sup>-1</sup>. Meanwhile, it is also a kind of shell material that can be used to fabricate core–shell nanoarray electrodes based on metal oxides and enhance the electrochemical performances. Xia *et al.* employed the hydrothermal and CVD methods to synthesize VO<sub>2</sub>-based core–shell composites (Fig. 2f), where HMB was first electrochemically deposited onto graphene foam (GF) surface and then VO<sub>2</sub> nanoflakes were grown on the hybrid surface.<sup>55</sup> When applied as the electrode,

the GF + VO<sub>2</sub>/HMB composites afforded better electrochemical performance with weaker polarization, higher specific capacitance, and better cycling life than those obtainable from GF + VO<sub>2</sub>. After 500 cycles, a high reversible capacity of 305 mA h g<sup>-1</sup> could be obtained at 5C (capacity retention: 91.8%) and 209 mA h g<sup>-1</sup> at 30C (capacity retention: 95.4%). The GF + VO<sub>2</sub>/HMB electrode showed stable capacitance of 473 F g<sup>-1</sup> at 2 A g<sup>-1</sup> after 5000 cycles and 340 F g<sup>-1</sup> at 12 A g<sup>-1</sup> after 11 000 cycles.

By means of an organic–inorganic liquid interface, Fan *et al.* prepared 2D mesoporous VO<sub>2</sub> microarrays with needle-like particles.<sup>56</sup> According to differences in the aqueous phase, VO<sub>2</sub>-N (organic phase), VO<sub>2</sub>-S (ultrapure water), and VO<sub>2</sub>-F (hydrazine added in an aqueous solution) can be synthesized, as shown in Fig. 2i. A VO<sub>2</sub>-N microarray could afford specific capacitance of 265 F g<sup>-1</sup> at 1 A g<sup>-1</sup>, with higher retention rate at high current density (182 F g<sup>-1</sup> at 10 A g<sup>-1</sup>) than those obtainable from VO<sub>2</sub>-S and VO<sub>2</sub>-F (Fig. 2g). Pan *et al.* reported that the hydrogen treatment of VO<sub>2</sub> powder resulted in an increase in the electrical conductivity, specific discharge capacitance of 300 F g<sup>-1</sup>, and specific energy density of 17 W h kg<sup>-1</sup>, along with excellent stability, which can be attributed to the formation of oxygen vacancies, slightly reduced valence state of V, and their synergetic effects.<sup>57</sup>

In investigations, there are two main strategies for improving the electrochemical performance of VO<sub>2</sub>: (1) synthesis of novel structures and (2) synthesis of VO<sub>2</sub> hybrid materials. However, only a little amount of research has been done on doping elements and changing the type of electrolyte. Doping elements in the material is a promising research trend.

#### 4.2 V<sub>2</sub>O<sub>3</sub> and its composite materials

V<sub>2</sub>O<sub>3</sub>, like other TMOs, is also an ideal energy storage material. For example, the conductivity of V<sub>2</sub>O<sub>3</sub> is 10<sup>3</sup> Ω<sup>-1</sup> cm<sup>-1</sup>, which is much higher than that of V<sub>2</sub>O<sub>5</sub> (10<sup>-3</sup> Ω<sup>-1</sup> cm<sup>-1</sup>) and monoclinic VO<sub>2</sub> (4 Ω<sup>-1</sup> cm<sup>-1</sup>). However, nanostructured V<sub>2</sub>O<sub>3</sub> materials suffer from poor cycling stability and can form soluble species in aqueous solutions.<sup>58,59</sup> It has been proven that a combination of nanostructured vanadium oxides and carbon can not only protect them from dissolution and structural deterioration but also improve their electron transfer efficiency and prevent the agglomeration of nanoparticles.<sup>60</sup> Further, V<sub>2</sub>O<sub>3</sub>/carbon composites (Table 3) can have different morphologies, such as

Table 3 Comparison of various types of V<sub>2</sub>O<sub>3</sub>/C nanocomposites as electrode materials for use in SCs

Nano-structures	Synthetic method	Electrolyte	Potential window (V)	Maximum SC	Current density	Cycling stability (%)	Ref.
V <sub>2</sub> O <sub>3</sub> @C core–shell composites	Heat treatment	1 M Na <sub>2</sub> SO <sub>4</sub>	–0.2–0.8	223 F g <sup>-1</sup>	0.1 A g <sup>-1</sup>	39.7% (100 cycles)	62
V <sub>2</sub> O <sub>3</sub> @C core–shell nanorods	Hydrothermal	5 M LiCl	–1.0–0.3	228 F g <sup>-1</sup>	0.5 A g <sup>-1</sup>	86% (1000 cycles)	33
V <sub>2</sub> O <sub>3</sub> nanofoam@activated carbon composites	Solvothermal	1 M NaNO <sub>3</sub>	–0.4–0.6	185 F g <sup>-1</sup>	0.05 A g <sup>-1</sup>	49% (100 cycles)	63
V <sub>2</sub> O <sub>3</sub> /C nanocomposites	Hydrothermal	5 M LiCl	–1.0–0.4	458.6 F g <sup>-1</sup>	0.5 A g <sup>-1</sup>	86% (1000 cycles)	64
V <sub>2</sub> O <sub>3</sub> /N-rGO nanoflakes	Hydrothermal	1 M Na <sub>2</sub> SO <sub>4</sub>	–0.2–0.6	216 mF cm <sup>-2</sup>	1 mA cm <sup>-2</sup>	81% (10 000 cycles)	65

fiber,<sup>61</sup> core-shell structures,<sup>33,62</sup> nanofoam,<sup>63</sup> nanoparticles,<sup>64</sup> and nanoflakes,<sup>65</sup> depending on the synthesis method. Some  $V_2O_3/C$  nanocomposites with good electrochemistry performance can be prepared by the hydrothermal reaction. For example, Hu *et al.* developed  $V_2O_3@C$  core-shell nanorods (Fig. 3a) with porous structures and large specific surface areas ( $246 \text{ m}^2 \text{ g}^{-1}$ ), affording specific capacitances of 228, 221, 207, 158, and  $127 \text{ F g}^{-1}$  at current densities of 0.5, 1, 2, 5, and  $10 \text{ A g}^{-1}$ , respectively.<sup>33</sup> In addition,  $V_2O_3@C//C$  SC afforded capacitance retention of 86% after 1000 cycles.  $V_2O_3@C$  exhibited good cycling performance for SC applications.  $V_2O_3/C$  nanocomposites (specific surface area:  $106.8 \text{ m}^2 \text{ g}^{-1}$ ; Fig. 3d) synthesized by Zheng *et al.* exhibited high specific intercalation pseudocapacitance of  $458.6 \text{ F g}^{-1}$  at  $0.5 \text{ A g}^{-1}$  with a retention rate of 86% after 1000 cycles in an aqueous electrolyte.<sup>64</sup> Notably, in some other studies, the electrochemical performances were unremarkable. Zheng *et al.* showed that the specific capacitances of the as-obtained  $V_2O_3@C$  core-shell composites (specific surface area:  $83.2 \text{ m}^2 \text{ g}^{-1}$ ; Fig. 3c) were 146, 128, 83, and  $58 \text{ F g}^{-1}$  in the 1st, 10th, 50th, and 100th cycle, respectively, and the corresponding retentions were 87.7, 56.8, and 39.7% of the initial discharge capacity.<sup>62</sup> The composites prepared by the same method exhibited different morphologies

(different specific surface areas) due to their different reactants and reaction conditions. At the same time, different electrolytes, test methods, environments, and personnel resulted in completely different electrochemical performances.

Zhang *et al.* produced a  $V_2O_3$  nanofoam@activated carbon composite (specific surface area:  $42.6 \text{ m}^2 \text{ g}^{-1}$ ) by the solvothermal method, which exhibited specific capacitance of  $185 \text{ F g}^{-1}$  at  $0.05 \text{ A g}^{-1}$ .<sup>63</sup> The capacitance was found to rapidly decrease in the first 30 cycles, and only 49% of the initial value was retained after 100 cycles. In addition, a self-supported film electrode ( $V_2O_3/N$ -rGO) was fabricated where nitrogen-doped rGO was intertwined with  $V_2O_3$  nanoflakes, as shown in Fig. 3f; evidently, areal capacitance of  $216 \text{ mF cm}^{-2}$  could be obtained at a current density of  $1 \text{ mA cm}^{-2}$  with excellent cycling stability with capacitance retention of 81% after 10 000 cycles.<sup>65</sup> Different methods and reactants used to prepare different nanomaterials afford different electrochemical properties.

Nowadays, the study of  $V_2O_3$  and its composites for use in SCs has been superficial; nanocomposites, such as  $V_2O_3$  with a novel structure,  $V_2O_3$ /conducting polymers,  $V_2O_3$ /transition metal compounds, and elemental doping, should be explored in

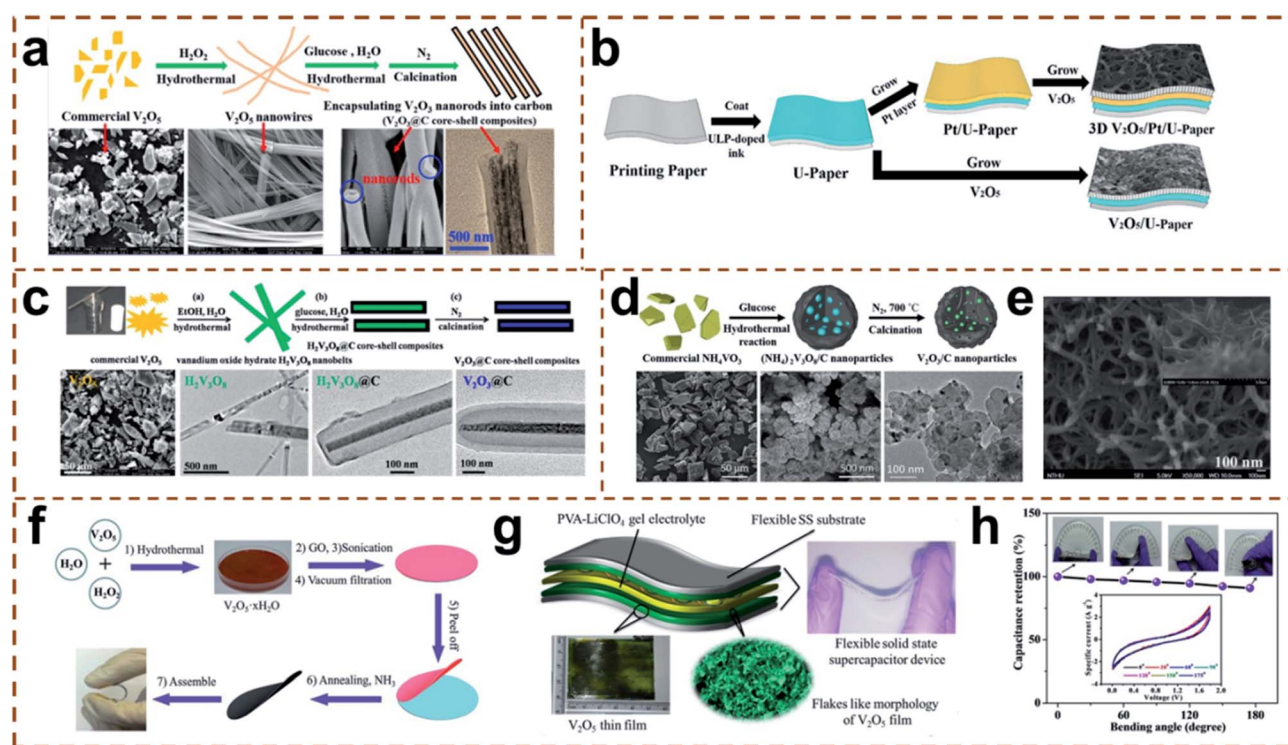


Fig. 3 (a) Schematic illustration of the encapsulation of  $V_2O_3$  nanorods into carbon core-shell-structured composites. (b) Schematic illustration of the fabrication of porous  $V_2O_5/U$ -paper and 3D network  $V_2O_5/Pt/U$ -paper electrodes. (c) Schematic illustration of the synthesis of  $V_2O_3@C$  core-shell-structured composites. (d) Schematic illustration of the synthesis of highly dispersed VO-C. (e) SEM image of 3D network  $V_2O_5/Pt/U$ -paper. (f) Schematic of the fabrication of flexible and self-supported  $V_2O_3/N$ -rGO film electrodes and the assembly of all-solid-state flexible SC devices. (g) Schematic representation of the fabricated FASC device based on  $V_2O_5$  electrodes with PVA- $\text{LiClO}_4$  gel electrolyte. (h) Capacitance retention for altered bending angles; inset shows the CVs with various bending angles at a scan rate of  $20 \text{ mV s}^{-1}$ . (a) Reprinted with permission.<sup>33</sup> Copyright 2017, Elsevier. (b and e) Reprinted with permission.<sup>70</sup> Copyright 2019, American Chemical Society. (c) Reprinted with permission.<sup>62</sup> Copyright 2017, Elsevier. (d) Reprinted with permission.<sup>64</sup> Copyright 2019, Elsevier. (f) Reprinted with permission.<sup>65</sup> Copyright 2017, The Royal Society of Chemistry. (g and h) Reprinted with permission.<sup>71</sup> Copyright 2017, Elsevier.



Table 4 Comparison of various types of V<sub>2</sub>O<sub>5</sub> and its nanocomposites as electrode materials for use in SCs

Nano-structures (dimension)	Synthetic method	Electrolyte	Potential window (V)	Maximum SC	Current density	Cycling stability (%)	Ref.
V <sub>2</sub> O <sub>5</sub> nanofibers (1D)	Electrospinning method	2 M KCl	-0.2-0.7	190 F g <sup>-1</sup>	0.1 A g <sup>-1</sup>	—	43
V <sub>2</sub> O <sub>5</sub> nanoporous network (2D)	Capping-agent-assisted precipitation technique	1 M LiClO <sub>4</sub> /PPC 0.5 M K <sub>2</sub> SO <sub>4</sub>	0.0-3.0 0.0-1.0	250 F g <sup>-1</sup> 304 F g <sup>-1</sup>	100 mA g <sup>-1</sup>	76% (600 cycles)	66
V <sub>2</sub> O <sub>5</sub> ·H <sub>2</sub> O (2D)	Hydrothermal method	2 M KCl	-0.2-0.8	349 F g <sup>-1</sup>	5 mV s <sup>-1</sup>	—	68
V <sub>2</sub> O <sub>5</sub> complex (2D)	CBD	2 M LiClO <sub>4</sub>	0.0-1.0	735 F g <sup>-1</sup>	1 mV s <sup>-1</sup>	71% (1000 cycles)	71
Hollow spherical V <sub>2</sub> O <sub>5</sub> (3D)	Solvothermal method	5 M LiNO <sub>3</sub>	-0.2-0.8	479 F g <sup>-1</sup>	5 mV s <sup>-1</sup>	43% (100 cycles)	67
Hollow spherical V <sub>2</sub> O <sub>5</sub> /PPy (3D)	—	—	—	566 F g <sup>-1</sup>	—	70% (100 cycles)	70
V <sub>2</sub> O <sub>5</sub> nanofibers (3D)	Sol-gel method	1 M KCl	0.0-1.6	—	—	72.2% (5000 cycles)	70
rGO/V <sub>2</sub> O <sub>5</sub> hybrid aerogel composite	Modified Hummer's method	ULP gel	0.0-4.0	160 F g <sup>-1</sup>	1 A g <sup>-1</sup>	91% (5000 cycles)	74
VNF/graphene nanohybrid	Hydrothermal and <i>in situ</i> chemical method	1 M LiClO <sub>4</sub> /PPC 1 M LiTFSI in acetonitrile	-0.8-0.8 -0.4-1.2	384 F g <sup>-1</sup> 218 F g <sup>-1</sup>	0.1 A g <sup>-1</sup> 1 A g <sup>-1</sup>	82.2% (10 000 cycles) 87% (700 cycles)	74 75
rGO/V <sub>2</sub> O <sub>5</sub> nanobelts hybrid	Hydrothermal method	0.5 M K <sub>2</sub> SO <sub>4</sub>	-0.5-0.5	310.1 F g <sup>-1</sup>	1 A g <sup>-1</sup>	90.2% (5000 cycles)	76
rGO/V <sub>2</sub> O <sub>5</sub> nanosheet	Modified Hummers method	1 M KCl	0.0-0.8	635 F g <sup>-1</sup>	1 A g <sup>-1</sup>	94% (3000 cycles)	77
V <sub>2</sub> O <sub>5</sub> -graphene hybrid	Modified Hummers method	1 M Na <sub>2</sub> SO <sub>4</sub>	0.0-1.6	484 F g <sup>-1</sup>	0.6 A g <sup>-1</sup>	80% (10 000 cycles)	78
V <sub>2</sub> O <sub>5</sub> @rGO nanorods	Sol-gel method/modified Hummers method	0.75 M NaPF <sub>6</sub> in ethylene carbonate (EC)-diethyl carbonate (DEC) (1 : 1 in volume)	0.0-3.0	289 F g <sup>-1</sup>	0.01 A g <sup>-1</sup>	85% (1000 cycles)	38
3DG-wrapped V <sub>2</sub> O <sub>5</sub> nanospheres	Hydrothermal method	1 M Na <sub>2</sub> SO <sub>4</sub>	0.0-0.8	612.5 F g <sup>-1</sup>	1 A g <sup>-1</sup>	89.6% (10 000 cycles)	79
rGO/V <sub>2</sub> O <sub>5</sub>	Modified Hummers method	1 M LiClO <sub>4</sub> /PPC	-0.8-0.8	129.7 F g <sup>-1</sup>	0.1 A g <sup>-1</sup>	85% (8000 cycles)	80
Carbon coated flower V <sub>2</sub> O <sub>5</sub>	Co-precipitation method	1 M K <sub>2</sub> SO <sub>4</sub>	-0.1-0.8	417 F g <sup>-1</sup>	0.5 A g <sup>-1</sup>	100% (2000 cycles)	81
V <sub>2</sub> O <sub>5</sub> /C (HPVC) nanocomposites	—	2 M LiNO <sub>3</sub>	0.0-1.0	492.1 F g <sup>-1</sup>	5 mV s <sup>-1</sup>	93% (10 000 cycles)	82
MCM/V <sub>2</sub> O <sub>5</sub>	Spray drying and wet impregnation method	1 M Al <sub>2</sub> (SO <sub>4</sub> ) <sub>3</sub>	0.0-1.6	290 F g <sup>-1</sup>	0.5 A g <sup>-1</sup>	88% (10 000 cycles)	83
CNT/V <sub>2</sub> O <sub>5</sub> nanocomposite	Hydrothermal method	1 M LiClO <sub>4</sub> /PPC	1.6-4.0	228 C g <sup>-1</sup>	20 mV s <sup>-1</sup>	80% (10 000 cycles)	84
V <sub>2</sub> O <sub>5</sub> /carbon nanofiber composites	Electrospinning method	6 M KOH	0.0-1.0	150 F g <sup>-1</sup>	1 mA cm <sup>-2</sup>	—	85
V <sub>2</sub> O <sub>5</sub> /MWCNT core/shell hybrid aerogels	Sol-gel method	1 M Na <sub>2</sub> SO <sub>4</sub>	-0.1-1.0	625 F g <sup>-1</sup>	0.5 A g <sup>-1</sup>	120% (20 000 cycles)	39
Ultrathin V <sub>2</sub> O <sub>5</sub> anchored MWCNTs and graphene composites	LBL technique	2 M KCl	-0.6-0.6	2590 F g <sup>-1</sup>	1 mV s <sup>-1</sup>	96% (5000 cycles)	86
MWNT/V <sub>2</sub> O <sub>5</sub> NW composites	Sol-gel method	PVA-LiCl	0.0-0.8	80 F cm <sup>-3</sup>	10 mV s <sup>-1</sup>	82% (10 000 cycles)	87
3D N-GNFs/V <sub>2</sub> O <sub>5</sub> aerogels	—	1 M Na <sub>2</sub> SO <sub>4</sub>	-1.0-1.0	595.1 F g <sup>-1</sup>	0.5 A g <sup>-1</sup>	97% (12 000 cycles)	88
V <sub>2</sub> O <sub>5</sub> NW/3D N-GA	Solvothermal method	8 M LiCl	-0.3-0.7	710 F g <sup>-1</sup>	0.5 A g <sup>-1</sup>	95% (20 000 cycles)	89
3D V <sub>2</sub> O <sub>5</sub> /PPy core/shell nanostructures	—	5 M LiNO <sub>3</sub>	-0.2-0.8	448 F g <sup>-1</sup>	0.5 A g <sup>-1</sup>	81% (1000 cycles)	90
V <sub>2</sub> O <sub>5</sub> @PPy core-shell NW	Hydrothermal and <i>in situ</i> interfacial synthesis approach	1 M Na <sub>2</sub> SO <sub>4</sub>	-0.4-0.5	344 F g <sup>-1</sup>	0.2 A g <sup>-1</sup>	82.5% (2000 cycles)	91
V <sub>2</sub> O <sub>5</sub> -conductive polymer nanocables	—	1 M Na <sub>2</sub> SO <sub>4</sub>	-1.0-1.0	614 F g <sup>-1</sup>	0.5 A g <sup>-1</sup>	111% (15 000 cycles)	92
V <sub>2</sub> O <sub>5</sub> /TiO <sub>2</sub> composites	Hydrothermal method	1 M LiNO <sub>3</sub>	-0.2-0.8	587 F g <sup>-1</sup>	0.5 A g <sup>-1</sup>	92% (1000 cycles)	98

Table 4 (Contd.)

Nano-structures (dimension)	Synthetic method	Electrolyte	Potential window (V)	Maximum SC	Current density	Cycling stability (%)	Ref.
V <sub>2</sub> O <sub>5</sub> -doped- $\alpha$ -Fe <sub>2</sub> O <sub>3</sub> composite nanotubes	Electrospinning method	3 M KOH	-0.1-0.6	183 F g <sup>-1</sup>	1 A g <sup>-1</sup>	81.5% (200 cycles)	100
V <sub>2</sub> O <sub>5</sub> /Ni <sub>3</sub> S <sub>2</sub> nanoflakes	Hydrothermal method	2 M NaOH	0.0-0.5	3060 F g <sup>-1</sup>	1 mV s <sup>-1</sup>	85% (2500 cycles)	101
V <sub>2</sub> O <sub>5</sub> @Ni <sub>3</sub> S <sub>2</sub> hybrid nanoarray	Hydrothermal method	1 M KOH	0.0-0.6	854 F g <sup>-1</sup>	1 A g <sup>-1</sup>	60% (1000 cycles)	102
V <sub>2</sub> O <sub>5</sub> /Na <sub>0.33</sub> V <sub>2</sub> O <sub>5</sub>	Co-precipitation technique	1 M LiClO <sub>4</sub>	-0.2-0.6	334 F g <sup>-1</sup>	1 A g <sup>-1</sup>	96% (1000 cycles)	103
SnO <sub>2</sub> -V <sub>2</sub> O <sub>5</sub> -CNT	Solid-state and hydrothermal method	0.1 M KCl	0.0-0.8	121.39 F g <sup>-1</sup> (anodic) 119.85 F g <sup>-1</sup> (cathodic)	100 mV s <sup>-1</sup> 100 mV s <sup>-1</sup>	85.8% (100 cycles) (anodic) 87.2% (100 cycles) (cathodic)	104
V <sub>2</sub> O <sub>5</sub> /PEDOT/MnO <sub>2</sub> nanosheets	Hydrothermal method	1 M Na <sub>2</sub> SO <sub>4</sub>	0.0-0.8	266.4 F g <sup>-1</sup>	2 mV s <sup>-1</sup>	93.5% (3000 cycles)	105

the future, which deserves more time and energy to be spent by several researchers.

### 4.3 V<sub>2</sub>O<sub>5</sub> and its composites

**4.3.1 V<sub>2</sub>O<sub>5</sub> materials.** There are many factors affecting the electrochemical properties of materials, such as morphology, electrolytes, surfactants, and so on. Achieving excellent electrochemical performance requires active electrode materials, such as TMOs, carbon-based materials, and conducting polymers, which can help in improving the energy storage of the equipment. V<sub>2</sub>O<sub>5</sub> TMOs are another promising candidate as electrode materials for use in SCs (Table 4), with a high theoretical specific capacity (2120 F g<sup>-1</sup>), economic feasibility, and natural abundance. However, V<sub>2</sub>O<sub>5</sub> has a low surface area, poor electrical conductivity, and low structural stability, and its nanostructures typically exhibit only a relatively low energy density. Therefore, to enhance its electrochemical properties, the use of structural engineering, unique shapes, and suitable electrolytes are effective strategies.

The porosity of nanomaterials facilitates the diffusion of ions and electrons and prolongs the material life in energy storage systems. Excellent electrode materials are needed to achieve higher specific capacitance. Saravanakumar *et al.* developed a simple capping-agent-assisted precipitation technique to synthesize V<sub>2</sub>O<sub>5</sub> nanoporous networks.<sup>66</sup> When utilized as an electrode material in a three-electrode system, the V<sub>2</sub>O<sub>5</sub> nanoporous network achieved higher specific capacitance of 316 F g<sup>-1</sup> as compared to those of the as-prepared samples with annealing. When the annealing temperature increased to 300 °C, the specific capacitance correspondingly decreased to 135 F g<sup>-1</sup> due to the shrinking pores of the sample. In addition, this material exhibited comparatively excellent capacity retention. Hollow V<sub>2</sub>O<sub>5</sub> spheres, as a class of porous material, were fabricated by a solvothermal process by Yang *et al.*<sup>67</sup> When used as an electrode for use in SCs in a solution of 5 M LiNO<sub>3</sub>, these materials showed a tremendous pseudocapacitance effect with high capacitance of 479 F g<sup>-1</sup> at 5 mV s<sup>-1</sup>. When polypyrrole (PPy) was deposited onto the surface of these hollow V<sub>2</sub>O<sub>5</sub> spheres, the capacitance was increased to 566 F g<sup>-1</sup> at 5 mV s<sup>-1</sup> with a capacity retention rate of 70% after 100 cycles. As mentioned above, materials with porous structures retain a higher specific area and more active sites, which can facilitate ion transport and improve the electrochemical performance.

Surfactants can change the morphology of the materials to enhance the specific surface area and electrochemical properties. Yang *et al.* synthesized V<sub>2</sub>O<sub>5</sub>·H<sub>2</sub>O by the hydrothermal method in several surfactants, such as polyethylene glycol 6000 (PEG-6000), sodium dodecylbenzene sulfonate (SDBS), and Pluronic P-123 (P123).<sup>68</sup> As an electrode, V<sub>2</sub>O<sub>5</sub>·H<sub>2</sub>O NWs in the presence of PEG-6000 exhibited the highest capacitance of 349 F g<sup>-1</sup> at a scan rate of 5 mV s<sup>-1</sup> than those with the surfactants of SDBS (flower-like stacks of flakes) and P123 (perforated networks with curly, bundled NWs), which may be due to the smooth migration of electrons along the homogeneous and straight NWs. However, a symmetric P123 electrode showed specific capacitance of 127 F g<sup>-1</sup> in comparison with a PEG-6000

electrode ( $45 \text{ F g}^{-1}$ ) after 200 cycles, which can be ascribed to their morphologies. Therefore, the morphology has a positive impact on the specific capacitance, which does not mean that it also has a good impact on the cycling performance.

In addition, the variability of vanadium oxide in aqueous solutions can be ascribed to material dissolution and weak structural stability during electrochemical measurements.<sup>59,69</sup> Deng *et al.* synthesized a 3D  $\text{V}_2\text{O}_5$  network by electrodeposition and tested its electrochemical performance in gel electrolytes.<sup>70</sup> The synthesis routes and structures of porous  $\text{V}_2\text{O}_5$ /conductive printing paper (U-paper) and 3D network  $\text{V}_2\text{O}_5$ /Pt/U-paper are shown in Fig. 3b. Fig. 3e shows the 3D network  $\text{V}_2\text{O}_5$ /Pt/U-paper with a high surface area of  $\sim 122 \text{ m}^2 \text{ g}^{-1}$  and pore size distribution containing 21.3% micropores ( $< 2 \text{ nm}$ ), 70.1% mesopores (2–50 nm), and 8.6% macropores ( $> 50 \text{ nm}$ ). When an inorganic electrolyte (1 M KCl solution) was used, porous  $\text{V}_2\text{O}_5$ /U-paper, 3D network  $\text{V}_2\text{O}_5$ /Pt/U-paper, and  $\text{V}_2\text{O}_5$ /carbon cloth (CC) as the symmetric pseudocapacitor (SPC) electrodes were examined: the 3D network  $\text{V}_2\text{O}_5$ /Pt/U-paper electrode (operating voltage ranging from 0.0 to 1.6 V) showed higher capacitance retention (72% after 5000 cycles). This implied that the nanostructures from the 3D network of the  $\text{V}_2\text{O}_5$ /Pt/U-paper-based SPC were uniform and the novel 3D network of the  $\text{V}_2\text{O}_5$  and Pt layer could reduce the dissolution of  $\text{V}_2\text{O}_5$  and improve the structural stability. Interestingly, with urea- $\text{LiClO}_4$ -polyvinyl alcohol (PVA) (ULP) gel electrolytes, wearable SPCs (WSPCs) based on porous  $\text{V}_2\text{O}_5$ , 3D network  $\text{V}_2\text{O}_5$  (operating voltage ranging from 1.0 to 4.0 V), and  $\text{V}_2\text{O}_5$ /CC exhibited excellent retention levels of  $\sim 80.1$ , 91.1, and 77.6% after 5000 cycles, respectively. Electrospinning method, considered to be a simple, one-step, and cost-effective method, can be used to control the structure, morphology, and diameter (from tens of nanometers to several micrometers) of the nanofiber. Wee *et al.* fabricated  $\text{V}_2\text{O}_5$  nanofibers by using this method and measured it using different electrolytes (aqueous electrolytes at different pH values and organic electrolytes).<sup>43</sup> When this material was annealed at  $400^\circ\text{C}$ , the specific capacitance was  $190 \text{ F g}^{-1}$  in an aqueous electrolyte (2 M KCl; operating voltage window: 0.0–0.9 V) and  $250 \text{ F g}^{-1}$  in an organic electrolyte (1 M  $\text{LiClO}_4$  in PPC; operating voltage window: 0.0–3.0 V). As mentioned above, the gel electrolytes in  $\text{V}_2\text{O}_5$  WSPCs not only enhanced the mechanical stability but also minimized the chemical dissolution of  $\text{V}_2\text{O}_5$ . Further, organic electrolytes have excellent ionic transfer rates and can contribute toward higher operating voltages and excellent cycling stability as compared to those obtainable using inorganic electrolytes, which confirms the solubility and structural instability of this material in aqueous solutions.

Thin films are generally synthesized *via* vacuum evaporation, sputter deposition, pulsed laser deposition, CVD, thermal oxidation, and sol-gel processes. Pandit *et al.* formulated a simple and inexpensive chemical bath deposition (CBD) method to grow  $\text{V}_2\text{O}_5$  on a pliable stainless steel substrate and used the resulting nanocomposites as an electrode for use in SCs. This electrode exhibited high specific capacitance of  $735 \text{ F g}^{-1}$  at  $1 \text{ mV s}^{-1}$  in 2 M  $\text{LiClO}_4$  electrolyte and good capacitance retention of 71% after 1000 cycles.<sup>71</sup> Fig. 3g shows a schematic

representation of a completely flexible solid-state SC device. It consists of PVA- $\text{LiClO}_4$  gel electrolyte as the separator and two symmetric  $\text{V}_2\text{O}_5$  electrodes. The flexibility test (Fig. 3h) was performed by CV measurements at  $20 \text{ mV s}^{-1}$  at different bending angles from  $0^\circ$  to  $175^\circ$ . The device showed capacitance retention of 91% even at bending angles as high as  $175^\circ$ , demonstrating exceptional flexibility.

**4.3.2  $\text{V}_2\text{O}_5$ /carbon-based materials.** Carbon-based SCs in acid media can only provide low operating voltages between 1.0 and 3.0 V, which limits their energy and power densities.<sup>72,73</sup> Generally, carbon-based materials necessitate alkaline electrolytes during their electrochemical activity. The hydrothermal method is one of the most promising methods and can provide high vapor pressure and suitable temperature in closed vessels, thereby resulting in optimal structures of as-fabricated electrodes for high-performance SCs. Further, rGO/ $\text{V}_2\text{O}_5$  compounds were synthesized by using this method and a subsequent annealing process by Liu *et al.*<sup>74</sup> Fig. 4a shows the synthesis of holey graphene oxide (HGO) and rGO/ $\text{V}_2\text{O}_5$ . When rGO/ $\text{V}_2\text{O}_5$  composites were used as the electrode, the working potential values in the CV curves ranged from  $-0.8$  to  $0.8 \text{ V}$  in 1 M  $\text{LiClO}_4$ /PPC electrolyte. For the rGO/ $\text{V}_2\text{O}_5$  composites prepared at  $300^\circ\text{C}$  (RGV-300), the specific capacitances were 386, 338, 294, 241, and  $197 \text{ F g}^{-1}$  at 0.1, 0.2, 0.5, 1, and  $2 \text{ A g}^{-1}$ , respectively. An asymmetric system composed of RGV-300 and rGO as the cathode and anode, respectively, exhibited excellent performance, with specific capacitance retention of almost 82.2% after 10 000 cycles. Later, Choudhury *et al.* developed a simple, hydrothermal method and *in situ* chemical process to prepare  $\text{V}_2\text{O}_5$  nanofiber/exfoliated graphene nanohybrid at mass ratios of 1 : 0.25 and 1 : 0.5 (the as-prepared nanohybrids were denoted as  $\text{V}_1\text{G}_{0.25}$  and  $\text{V}_1\text{G}_{0.5}$ , respectively).<sup>75</sup> When the CV test was performed in the voltage range from  $-0.4$  to  $1.2 \text{ V}$  at the scan rate of  $25 \text{ mV s}^{-1}$ ,  $\text{V}_1\text{G}_{0.5}$  showed a larger area than those of  $\text{V}_1\text{G}_{0.25}$  and  $\text{V}_2\text{O}_5$  nanofibers. Evidently,  $\text{V}_1\text{G}_{0.5}$  afforded a higher charge storage capacity. Besides,  $\text{V}_1\text{G}_{0.5}$  nanohybrids in acetonitrile electrolyte of 1 M LiTFSI exhibited the best capacitance among the series, with specific capacitance of  $218 \text{ F g}^{-1}$  at  $1 \text{ A g}^{-1}$ , energy density of  $22 \text{ W h kg}^{-1}$ , and power density of  $3594 \text{ W kg}^{-1}$ . In addition, it is a challenge to realize the strong interactions between modified materials and graphene aerogel. Here, the rGO nanosheet/ $\text{V}_2\text{O}_5$  nanobelt (VNB) hybrid prepared by a hydrothermal process was reported by Yao *et al.*<sup>76</sup> They successfully obtained hybrid nanobelts and revealed their porous structures (Fig. 4b). Further, the resultant rGO/ $\text{V}_2\text{O}_5$  hybrid aerogel electrode retained high specific capacitance of  $310 \text{ F g}^{-1}$  at scan rates of  $1 \text{ A g}^{-1}$ . Moreover, SSCs based on rGO/ $\text{V}_2\text{O}_5$  hybrid aerogel were assembled, which recorded high gravimetric capacitance of  $225.6 \text{ F g}^{-1}$  ( $0.5 \text{ A g}^{-1}$ ), high energy density of  $31.3 \text{ W h kg}^{-1}$  ( $249.7 \text{ W kg}^{-1}$ ), and excellent long-term cycling stability (90.2% after 5000 cycles).

Different morphologies (nanosheets,<sup>77,78</sup> nanonords,<sup>38</sup> and nanospheres<sup>79</sup>) can provide larger surface areas, shorten the ion/electron diffusion distances, offer more active sites, and alleviate the concentration polarization of electrode materials, resulting in different electrochemical performances. Nagaraju *et al.* reported the 2D heterostructures of  $\text{V}_2\text{O}_5$ /rGO nanosheets that were

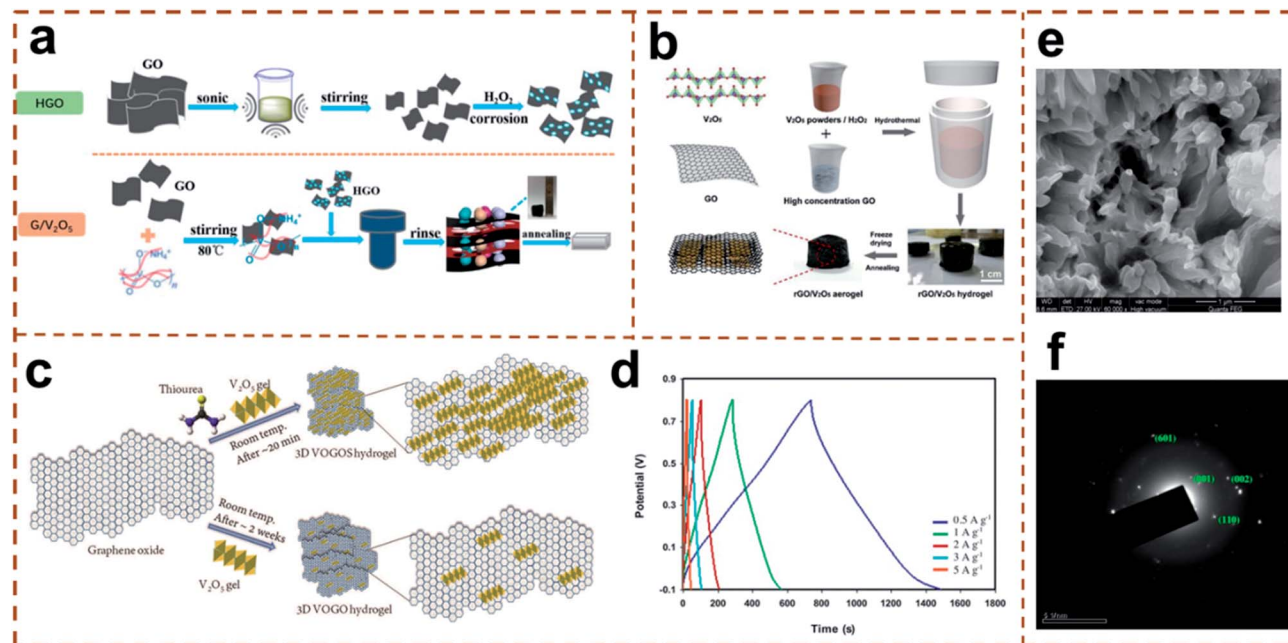


Fig. 4 (a) Diagrams of the syntheses of HGO and rGO/V<sub>2</sub>O<sub>5</sub>. (b) Schematic illustration of the synthesis of rGO/V<sub>2</sub>O<sub>5</sub> hybrid aerogels. (c) Schematic illustration of the assembly process. (d) Charge and discharge curves of carbon coated flowery V<sub>2</sub>O<sub>5</sub> electrode at different current densities. (e) FESEM images of carbon-coated flowery V<sub>2</sub>O<sub>5</sub>. (f) SAED pattern of carbon-coated flowery V<sub>2</sub>O<sub>5</sub>. (a) Reprinted with permission.<sup>74</sup> Copyright 2018, Elsevier. (b) Reprinted with permission.<sup>76</sup> Copyright 2018, Elsevier. (c) Reprinted with permission.<sup>78</sup> Copyright 2017, The Royal Society of Chemistry. (d) Reprinted with permission.<sup>80</sup> Copyright 2014, Wiley-VCH. (d–f) Reprinted with permission.<sup>81</sup> Copyright 2015, Elsevier.

obtained by growing 2D heterostructures of V<sub>2</sub>O<sub>5</sub> nanosheets on rGO flakes.<sup>77</sup> This material exhibited relatively high specific capacity (653 F g<sup>-1</sup> at 1 A g<sup>-1</sup>) and cycling stability (94% after 3000 cycles). Moreover, Yilmaz *et al.* successfully crosslinked a V<sub>2</sub>O<sub>5</sub>-graphene hybrid, affording surface area of up to 83.4 m<sup>2</sup> g<sup>-1</sup> using a V-thiourea redox system (Fig. 4c).<sup>78</sup> After the initial 5000 cycles, this system could retain 85% of the initial capacitance, while only 5% capacitance was lost between 5000 and 10 000 cycles, revealing good long-term cycling stability. Moreover, Kiruthiga *et al.* embedded V<sub>2</sub>O<sub>5</sub> nanorods into rGO as a high-energy-density battery-type Faradaic anode, and they used activated porous carbon as the high-power-density SC-type non-Faradaic cathode, which delivered specific capacitances of 289 and 224 F g<sup>-1</sup> at 0.01 A g<sup>-1</sup>, respectively.<sup>38</sup> A sodium-ion capacitor assembled with an anode made of V<sub>2</sub>O<sub>5</sub>@rGO and cathode made of activated porous carbon exhibited an energy density of 65 W h kg<sup>-1</sup>, power density of 72 W kg<sup>-1</sup> at 0.03 A g<sup>-1</sup>, and capacity retention of 74% after 1000 cycles at a current density of 0.06 A g<sup>-1</sup>. Meanwhile, Ghaly *et al.* summarized the results obtained earlier and successfully synthesized 3DG-wrapped V<sub>2</sub>O<sub>5</sub> nanospheres as the positive electrode and Fe<sub>3</sub>O<sub>4</sub>@3DG electrode as the negative electrode, which exhibited the maximum energy density of 54.9 W h kg<sup>-1</sup> with a power density of 898 W kg<sup>-1</sup> at an extended voltage of 1.8 V in 1.0 M Na<sub>2</sub>SO<sub>4</sub> aqueous electrolyte.<sup>79</sup> Furthermore, the ASC device demonstrated excellent cycling stability with 89.6% capacitance retention over 10 000 cycles.

Fabricating a freestanding graphene electrode for use in SCs can reduce the equivalent series resistance (ESR) and allow

higher loading density. To obtain lower ESR, the ionic resistance of the electrolyte, intrinsic resistance of the active material, and contact resistance between the active material and electrode in the SC system were adjusted by Too *et al.*<sup>80</sup> Experimentally, a V<sub>2</sub>O<sub>5</sub>-rGO freestanding electrode was synthesized *via* the modified Hummers' method, and high areal capacitance (511.7 mF cm<sup>-2</sup>) could be achieved. Fig. 4d shows the CV curves of the asymmetric device at 25 mV s<sup>-1</sup>. The specific capacitance of this composite was 417 F g<sup>-1</sup> at a current density of 0.5 A g<sup>-1</sup> (Fig. 4d). More importantly, the assembly of an asymmetric flexible device based on rGO/V<sub>2</sub>O<sub>5</sub>-rGO, which had an active mass of about 20 mg, exhibited a low ESR value of 3.36 Ω with excellent cycling stability.

Further, V<sub>2</sub>O<sub>5</sub>/carbon composite materials with many advantages were recently discussed (Table 4). The carbon-coated V<sub>2</sub>O<sub>5</sub> flower as the electrode materials for use in SCs have been reported by Balasubramanian *et al.*<sup>81</sup> The morphology of carbon-coated V<sub>2</sub>O<sub>5</sub> was examined by SEM, as shown in Fig. 4e, exhibiting flowerlike architecture with a well-resolved urchin-like structure. Moreover, the selected area electron diffraction (SAED, Fig. 4f) measurements revealed the amorphous nature of the carbon layer. The specific capacitance of this composite was 417 F g<sup>-1</sup> at a current density of 0.5 A g<sup>-1</sup>. However, the capacitance of the material gradually increased due to the activation process and attained the maximum capacitance (100%) at around 2000 cycles and decreased to 92.3% after 2250 cycles. Zhu *et al.* developed a simple "liquid-phase impregnation template" to hierarchically fabricate

porous  $V_2O_5/C$  (HPVC) nanocomposites using commercial  $V_2O_5$  and phenol-formaldehyde (PF) resol as the precursors and polystyrene opal microspheres as the template.<sup>82</sup> The preparation route for synthesizing HPVC is shown in Fig. 5a. Hierarchical porous HPVC nanocomposites with a high surface area ( $645 \text{ m}^2 \text{ g}^{-1}$ ) exhibited high specific capacitance of up to  $492.1 \text{ F g}^{-1}$  at a scan rate of  $5 \text{ mV s}^{-1}$  in  $2 \text{ M LiNO}_3$  electrolyte solution. Besides, the assembled symmetric electrode based on HPVC achieved an energy density as high as  $87.6 \text{ W h kg}^{-1}$  at a power density of  $210 \text{ W kg}^{-1}$ , as well as excellent cycling stability (93% after 10 000 cycles). Tian *et al.* fabricated nanostructured- $V_2O_5$ -impregnated mesoporous carbon microspheres (MCM/ $V_2O_5$ ) by a facile wet impregnation method (Fig. 5b), which entailed three steps, namely, spray drying, carbonization, and wet impregnation.<sup>83</sup> The electrochemical performances of the capacitors were evaluated by means of their CV curves using a symmetrical two-electrode system in Na-ion, Mg-ion, and Al-ion capacitors. When compared with Na-ion and Mg-ion capacitors, the Al-ion capacitor induced more effective reactions and higher capacitance enhancement, with specific capacitance of  $290 \text{ F g}^{-1}$  at  $0.5 \text{ A g}^{-1}$ , high energy density of up to  $18.0 \text{ W h kg}^{-1}$  at  $147 \text{ W kg}^{-1}$ , and promising cycling stability with up to 88% capacitance retention after 10 000 cycles.

CNTs have hierarchically porous structures that enhance ion transport. Chen *et al.* synthesized CNT/ $V_2O_5$  nanocomposites through a one-pot hydrothermal process. For pseudocapacitive materials composed of CNTs and  $V_2O_5$  NW interpenetrating networks, a capacity of  $86 \text{ C g}^{-1}$  could be obtained between 1.8 and 4.0 V in  $1 \text{ M LiClO}_4$  in a PPC solution, with an energy density of  $40 \text{ W h kg}^{-1}$  and a power density of  $210 \text{ W kg}^{-1}$  at a current density of  $0.5 \text{ mA cm}^{-2}$ .<sup>84</sup> Using the electrospinning method, Kim *et al.* prepared the  $V_2O_5$ /carbon nanofiber composites (CNFCs) at different  $V_2O_5$  concentrations (5, 10, and 20%), which were referred to as  $V_2O_5$ -5,  $V_2O_5$ -10, and  $V_2O_5$ -20, respectively. Here,  $V_2O_5$ -20 afforded the highest specific capacitance.<sup>85</sup> MWCNTs have been commonly used as electrode materials and composite materials for enhancing the porous structure, conductivity, and surface area.  $V_2O_5$ /MWCNT core-shell hybrid aerogels at different MWCNT contents using the sol-gel method have been reported by Wu *et al.*<sup>39</sup> Fig. 5c shows the mixed growth and self-assembly methodology for the controlled synthesis of 3D  $V_2O_5$ /MWCNT core-shell hybrid aerogels. The charge transfer resistance ( $R_{ct}$ ) values of the as-prepared aerogels and other samples were obtained from the EIS measurements (Fig. 5d). The hybrid aerogel exhibited the maximum specific capacitance ( $625 \text{ F g}^{-1}$ ) and outstanding

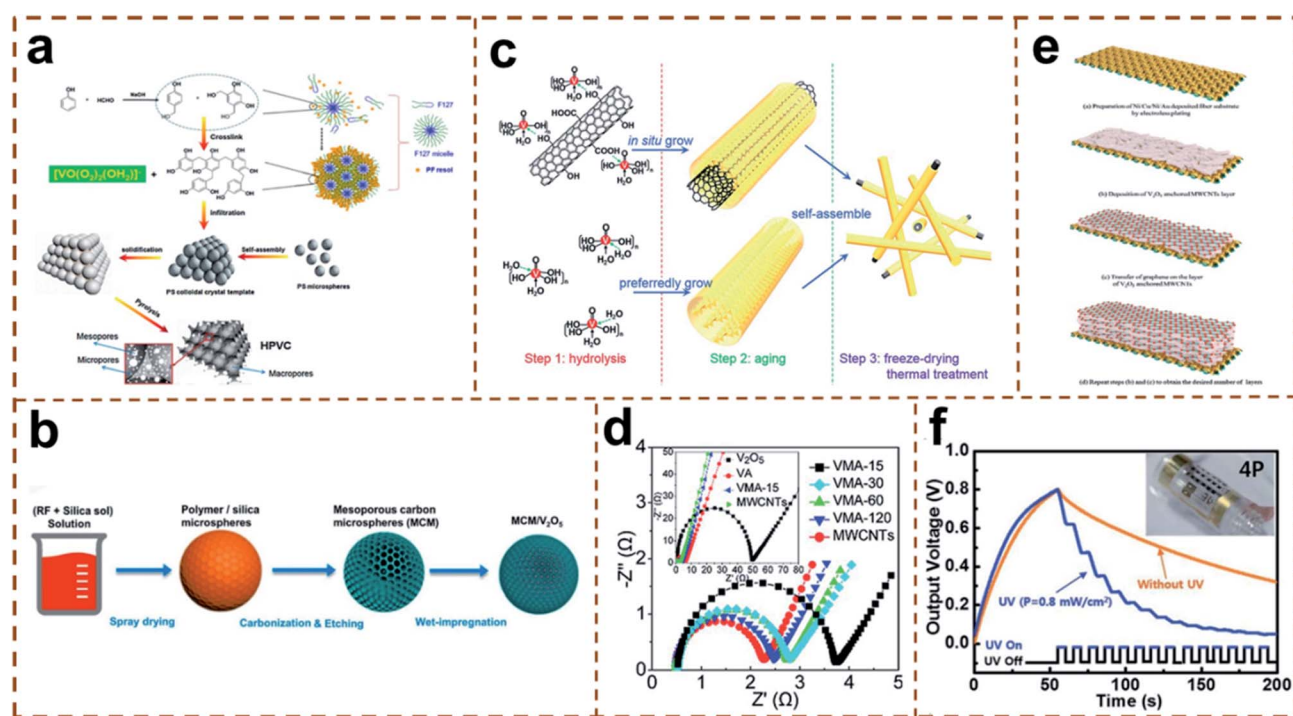


Fig. 5 (a) Schematic illustration of the preparation route of HPVC. (b) Synthesis of MCM/ $V_2O_5$  composites with spray drying for MCM preparation followed by wet impregnation to obtain the composites. (c) Illustration of the mixed growth and self-assembly methodology for the controlled synthesis of 3D  $V_2O_5$ /MWCNT core-shell hybrid aerogels. (d) EIS spectra of raw  $V_2O_5$  powder,  $V_2O_5$  aerogel,  $V_2O_5$ /MWCNT hybrid aerogels, and MWCNTs. (e) Schematic illustration of the fabrication of the LBL assembly of ultrathin  $V_2O_5$ -anchored MWCNTs and graphene on Ni/Cu/Ni/Au-coated textile fiber fabrics for flexible SC applications. (f) Charge/discharge curves of MSC arrays where four MSC arrays are connected in parallel (4P) with periodic irradiation of UV light (254 nm) onto the integrated  $SnO_2$  NW UV sensor during discharge (blue). The duration and period of UV pulse are 5 s. For comparison, the self-discharge curve without periodic UV irradiation is shown (orange). (a) Reprinted with permission.<sup>82</sup> Copyright 2017, Elsevier. (b) Reprinted with permission.<sup>83</sup> Copyright 2019, American Chemical Society. (c and d) Reprinted with permission.<sup>39</sup> Copyright 2015, The Royal Society of Chemistry. (e) Reprinted with permission.<sup>86</sup> Copyright 2014, The Royal Society of Chemistry. (f) Reprinted with permission.<sup>87</sup> Copyright 2014, The Royal Society of Chemistry.

cycling performance (>20 000 cycles) because of its high specific surface area, favorable electrical conductivity, and unique 3D and core-shell structures. Shakir *et al.* reported a composite made by the layer-by-layer assembly (LBL) technique and consisted of ultrathin  $V_2O_5$  anchored on MWCNTs and graphene, in which a graphene layer was alternatively inserted between the MWCNT films coated with ultrathin (3 nm)  $V_2O_5$  (Fig. 5e).<sup>86</sup> Such a structure mitigated the issues of low surface area and poor electrical conductivities of nanostructured  $V_2O_5$  when used in electrochemical SCs. When investigating LBL-assembled electrodes composed of MWCNTs coated with a 3 nm-thick  $V_2O_5$  layer and graphene in a three-electrode system using KCl as the aqueous electrolyte, specific capacitance of  $2590 \text{ F g}^{-1}$  could be achieved at a scan rate of  $1 \text{ mV s}^{-1}$  when compared with that obtained when using a 20 nm-thick  $V_2O_5$  layer on MWCNTs ( $510 \text{ F g}^{-1}$ ). In addition, the energy density reached  $96 \text{ W h kg}^{-1}$  at a power density of  $800 \text{ W kg}^{-1}$  and reduced to  $28 \text{ W h kg}^{-1}$  at a power density of  $9 \text{ kW kg}^{-1}$  when the SC electrode assembled by LBL was tested in an organic electrolyte ( $\text{LiClO}_4$ ). Kim *et al.* prepared MWNT/ $V_2O_5$  NW composites by using the sol-gel method for the assembly of a flexible micro-SC (MSC) with a solid electrolyte.<sup>87</sup> The MSC using MWNT/ $V_2O_5$  NW composites of the hybrid electrodes with 10 vol% of  $V_2O_5$  NWs exhibited excellent electrochemical

performance with high volume capacitance of  $80 \text{ F cm}^{-3}$  at a scan rate of  $10 \text{ mV s}^{-1}$  in PVA-LiCl electrolyte and afforded good cycling performance with capacitance retention of 82% after 10 000 cycles at a current density of  $11.6 \text{ A cm}^{-3}$ . Fig. 5f shows that the rate of voltage drop ( $dV/dt$ ) with UV was initially accelerated ( $30.8 \text{ mV s}^{-1}$  vs.  $9.8 \text{ mV s}^{-1}$ ) but later became almost the same as that without UV ( $3 \text{ mV s}^{-1}$  vs.  $2.8 \text{ mV s}^{-1}$ ). That is, the photosensitivity estimated from the ratio of  $dV/dt$  with and without UV was  $\sim 5$  in the initial 25 s and then became saturated to 1. These results showed the potential applications of MSCs as a power supply for the operation of nanodevices (including NW sensors). MWCNTs are a good supporting material; after combining with  $V_2O_5$ , they afford superb specific capacitance.

To overcome the extreme hydrophobicity of carbonaceous materials and strengthen the connection between the carbon host and  $V_2O_5$ , it is necessary to introduce additional heteroatoms, particularly nitrogen atoms, into the carbon framework. Sun *et al.* reported the fabrication of self-assembled 3D N-CNFs/ $V_2O_5$  aerogels, affording stable and homogeneous core-shell morphology (Fig. 6a and b).<sup>88</sup> In addition, the specific capacitance of N-CNFs/ $V_2O_5$  aerogels was always higher than that of CNFs/ $V_2O_5$  aerogels and CNFs@ $V_2O_5$  aerogels. From Fig. 6f, it is evident that the semicircle ( $R_{ct}$ ) of N-CNFs/ $V_2O_5$  aerogels ( $1.04 \Omega$ ) was much smaller than that of CNFs/ $V_2O_5$  aerogels ( $2.72 \Omega$ ).

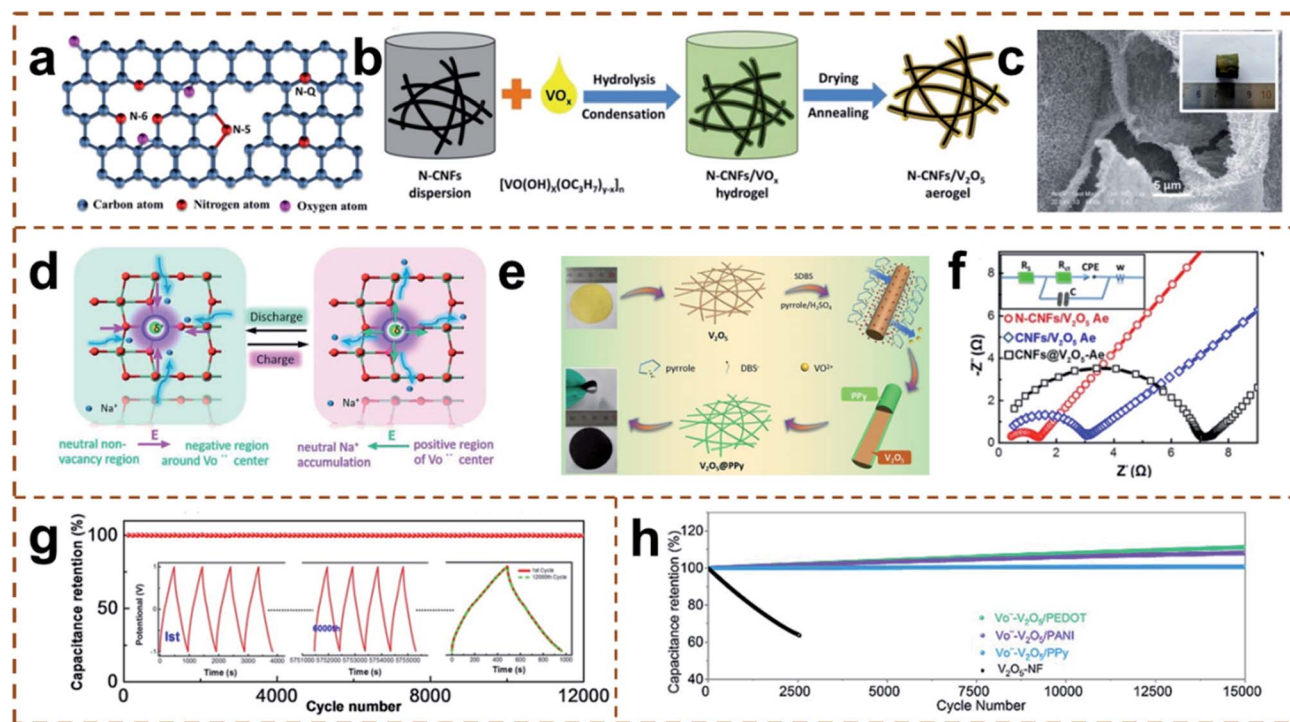


Fig. 6 (a) Schematic model of N-containing surface functional groups on N-CNFs. (b) Schematic illustration of the fabrication process and structure of N-CNF/ $V_2O_5$  aerogels. (c) SEM images and photographs of N-GA@ $V_2O_5$  NWAs. (d) Schematic illustration of the enhanced ionic transfer kinetics around  $V\ddot{o}$  by the formation of E. (e) Schematic illustration of the *in situ* interfacial synthesis of  $V_2O_5$ @PPy NW membranes. (f) Nyquist plots of the experimental impedance and their equivalent circuit analysis. (g) Cycling stability measurements at a current density of  $0.5 \text{ A g}^{-1}$  and the initial profiles for the first four charge/discharge cycles, charge/discharge profiles after 6000 cycles, and triangular shapes of the first and 12 000th cycle. (h) Cycling performances of  $V\ddot{o}$ - $V_2O_5$ /CPs and  $V_2O_5$ -NFs at  $10 \text{ A g}^{-1}$ . (a, b, f, and g) Reprinted with permission.<sup>88</sup> Copyright 2018, Elsevier. (c) Reprinted with permission.<sup>89</sup> Copyright 2018, The Royal Society of Chemistry. (d and h) Reprinted with permission.<sup>92</sup> Copyright 2019, The Royal Society of Chemistry. (e) Reprinted with permission.<sup>91</sup> Copyright 2018, American Chemical Society.

After 12 000 cycles, the specific capacitance was  $575.6 \text{ F g}^{-1}$  and 97% of the initial capacitance was retained (Fig. 6g). Further, Sun *et al.* synthesized hierarchical nanocomposites of  $\text{V}_2\text{O}_5$  nanowire arrays (NWAs) on a 3D N-doped graphene aerogel (N-GA) with different reaction intervals.<sup>89</sup> The scanning electron microscopy (SEM) image of this material with a porous structure is shown in Fig. 6c. When used as the electrode materials for use in SCs in an aqueous solution of 8 M LiCl, the specific capacitance of N-GA@ $\text{V}_2\text{O}_5$  NWAs was calculated to be  $710 \text{ F g}^{-1}$ , which was much higher than that of GA@ $\text{V}_2\text{O}_5$  ( $320 \text{ F g}^{-1}$ ) at a current density of  $0.5 \text{ A g}^{-1}$ . Furthermore, the N-GA@ $\text{V}_2\text{O}_5$  NWAs exhibited outstanding rate performance and good cycling behavior, with specific capacitance retention of 95% after 20 000 cycles. Nitrogen atoms were introduced into carbon-based materials, and their hydrophobicity was considerably limited, because of which the specific capacitance and cycling performance of the composite materials could be improved.

**4.3.3  $\text{V}_2\text{O}_5$ /conducting polymers.** The combination of  $\text{V}_2\text{O}_5$  and carbon materials is an effective method to improve the performance of SCs, but its structure is unstable, that is, it cannot prevent V from dissolving, resulting in the loss of active sites. To mitigate this issue, conducting polymers, such as

poly(3,4-ethylenedioxythiophene) (PEDOT), PPy, and polyaniline (PANI) have been integrated into  $\text{V}_2\text{O}_5$  to enhance the electrical conductivity, storage capacity, and chemical stability. Qian *et al.* successfully prepared interconnected 3D  $\text{V}_2\text{O}_5$ /PPy network nanostructures by an *in situ* polymerization process, which afforded high specific capacitance of  $448 \text{ F g}^{-1}$  as compared to stacked  $\text{V}_2\text{O}_5$ .<sup>90</sup> When an all-solid-state SSC device was assembled, the  $\text{V}_2\text{O}_5$ /PPy core-shell 3D network maintained good cycling stability (capacitance retention of 81% after 1000 cycles) and high energy density ( $14.2 \text{ W h kg}^{-1}$ ) at a power density of  $250 \text{ W kg}^{-1}$ . Wang *et al.* synthesized  $\text{V}_2\text{O}_5$ @PPy core-shell NWs by a facile *in situ* interfacial synthesis approach (Fig. 6e).<sup>91</sup> As binder- and additive-free SC electrodes, they could achieve specific capacitance of  $334 \text{ F g}^{-1}$ , along with superior rate capability. Moreover, as the entire lattice remained unchanged, the electronic structure could be adjusted such that oxygen vacancies appear in the  $\text{V}_2\text{O}_5$  conductive polymer, thereby effectively improving the electrochemical performance. Bi *et al.* developed  $\text{V}_2\text{O}_5$ -conductive polymer nanocables with oxygen vacancies.<sup>92</sup> The schematic illustration of the enhanced ionic transfer kinetics around the oxygen vacancies ( $\ddot{\text{O}}$ ) by the formation of a local electric field ( $E$ ) is shown in Fig. 6d. When

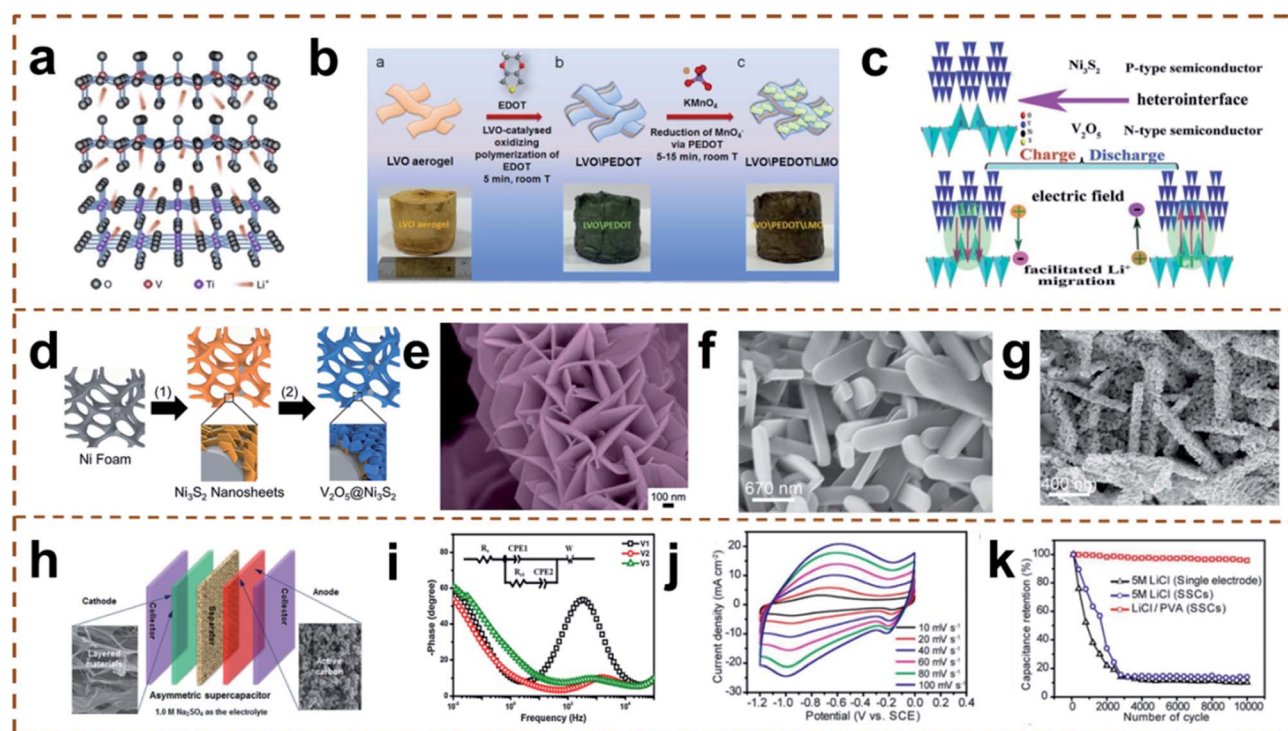


Fig. 7 (a) Crystal structure and charge/discharge processes of hierarchical VNB/TNF heterojunction composite. (b) Schematic and digital photographs showing the fabrications of LVO aerogel, LVO/PEDOT, and LVO/PEDOT/LMO. (c) Diagram of the charge transport in  $\text{V}_2\text{O}_5$ / $\text{Ni}_3\text{S}_2$  nanoflake nanostructures. (d) Schematic illustration of the two-step method for the synthesis of hierarchical  $\text{V}_2\text{O}_5$ @ $\text{Ni}_3\text{S}_2$  nanomaterials. (e) FESEM images of hierarchical VNB/TNF heterojunction composite. (f) SEM images of  $\text{V}_2\text{O}_5$  nanorods. (g) SEM images of the resulting porous nanorods of VN. (h) Configuration of ASCs. (i) Bode plots for V1, V2, and V3 electrodes (inset shows the equivalent circuit of the fit). (j) CV curves of the VN NW electrode collected at various scan rates. (k) Cycling performance of single VN electrode and symmetric VN SC devices collected at a scan rate of  $100 \text{ mV s}^{-1}$  for 10 000 cycles in 5 M LiCl aqueous electrolyte and PVA-LiCl gel electrolyte. (a and e) Reprinted with permission.<sup>98</sup> Copyright 2018, Elsevier. (b and h) Reprinted with permission.<sup>105</sup> Copyright 2014, Elsevier. (c) Reprinted with permission.<sup>101</sup> Copyright 2014, The Royal Society of Chemistry. (d) Reprinted with permission.<sup>102</sup> Copyright 2017, The Royal Society of Chemistry. (f and g) Reprinted with permission.<sup>106</sup> Copyright 2009, American Chemical Society. (i) Reprinted with permission.<sup>103</sup> Copyright 2017, Elsevier. (j and k) Reprinted with permission.<sup>34</sup> Copyright 2013, American Chemical Society.

tested as an electrode for use in SCs, the specific capacitance of  $\text{V}_2\text{O}_5/\text{PEDOT}$  ( $614 \text{ F g}^{-1}$ ) was higher than that of  $\text{V}_2\text{O}_5/\text{PANI}$  ( $523 \text{ F g}^{-1}$ ) and  $\text{V}_2\text{O}_5/\text{PPy}$  ( $437 \text{ F g}^{-1}$ ). From Fig. 6h, it is evident that  $\text{V}_2\text{O}_5/\text{PEDOT}$ ,  $\text{V}_2\text{O}_5/\text{PANI}$ , and  $\text{V}_2\text{O}_5/\text{PPy}$  exhibited capacitance retentions of 111, 108, and 101%, respectively, after 15 000 cycles.

**4.3.4  $\text{V}_2\text{O}_5$ /transition metal composites.** Since transition metal compounds have the advantages of multivalent structures, various crystal structures, and different morphologies, they typically afford high theoretical specific capacitance (such as  $\text{V}_2\text{O}_5$  ( $2020 \text{ F g}^{-1}$ ),<sup>93</sup>  $\text{RuO}_2$  ( $1358 \text{ F g}^{-1}$ ),<sup>94</sup>  $\text{MnO}_2$  ( $1370 \text{ F g}^{-1}$ ),<sup>95</sup>  $\text{TiO}_2$  ( $1260 \text{ F g}^{-1}$ ),<sup>96</sup> and  $\text{MnS}_2$  ( $1504 \text{ F g}^{-1}$ )<sup>97</sup>). A combination of transition metal compounds and  $\text{V}_2\text{O}_5$  can further improve the electrochemical properties. Xu *et al.* grew VNB/ $\text{TiO}_2$  nanoflake (TNF) composites directly on Ni foam *via* a two-step hydrothermal process.<sup>98</sup> Fig. 7e shows that TNFs perpendicularly intersected one another in a hierarchical VNB/TNF heterojunction composite, which exhibited high porosity, high specific surface area, and better capacitive performance. Notably, the morphology of VNB/TNF composites could be readily manipulated from nanoparticles and nanoflakes into nanoflake spheres and thick nanoflakes within 1–8 h. When used as an electrode for use in SCs in 1 M  $\text{LiNO}_3$  electrolyte, the obtained crystal structure and charge/discharge processes are shown in Fig. 7a. The composites afforded high specific capacitance ( $587 \text{ F g}^{-1}$  at  $0.5 \text{ A g}^{-1}$ ) and good cycling stability (97% after 5000 cycles). Yang *et al.* reported the fabrication of  $\text{V}_2\text{O}_5\text{-TiO}_2$  nanotubes by self-organizing the anodization of Ti–V alloys, thermally annealing at  $300 \text{ }^\circ\text{C}$ , and then using the material as electrodes in SCs.<sup>99</sup> The specific capacitance of the nanotubes was  $220 \text{ F g}^{-1}$  with an energy density of  $19.56 \text{ W h kg}^{-1}$  and was found to be very stable in repeated cycles.  $\text{V}_2\text{O}_5$ -doped  $\alpha\text{-Fe}_2\text{O}_3$  composites were prepared *via* a simple one-step electrospinning technique followed by calcination treatment by Nie *et al.*<sup>100</sup> The weight ratio of 1.0% of the composites with mesoporous structures provided capacitance retention of  $150 \text{ F g}^{-1}$  over 200 cycles at  $6 \text{ A g}^{-1}$ . Wang *et al.* fabricated  $\text{V}_2\text{O}_5/\text{Ni}_3\text{S}_2$  nanoflakes by a simple one-step hydrothermal method.<sup>101</sup>  $\text{V}_2\text{O}_5$  is an n-type semiconductor, while  $\text{Ni}_3\text{S}_2$  is a p-type semiconductor;  $\text{Ni}_3\text{S}_2/\text{V}_2\text{O}_5$  can constitute a p–n heterojunction, leading to improved energy storage performance with better charge transfer kinetics and high rate capability. Fig. 7c shows the charge transport in  $\text{V}_2\text{O}_5/\text{Ni}_3\text{S}_2$  nanoflake nanostructures. As a SC electrode, the nanoflakes exhibited specific capacitances of 3060, 2676, 2089.6, and  $1520 \text{ F g}^{-1}$  at scan rates of 1, 2, 5, and  $10 \text{ mV s}^{-1}$ , respectively, and maintained 85% of their capacitance after 2500 cycles. Meanwhile, Zhong *et al.* reported hierarchical  $\text{V}_2\text{O}_5@/\text{Ni}_3\text{S}_2$  hybrid nanoarrays supported on Ni foam synthesized by a hydrothermal method.<sup>102</sup> The synthesis of hierarchical  $\text{V}_2\text{O}_5@/\text{Ni}_3\text{S}_2$  hybrid nanoarrays is shown in Fig. 7d. When galvanostatic charge/discharge (GCD) measurements are performed on a  $\text{V}_2\text{O}_5@/\text{Ni}_3\text{S}_2$  electrode at various current densities, the calculated capacitances are close to each other, indicating good rate capability. After 1000 cycles,  $\text{V}_2\text{O}_5@/\text{Ni}_3\text{S}_2$  retained 60% of its initial capacitance in comparison to 85% for  $\text{Ni}_3\text{S}_2$ . However, the capacitance was higher for the former than that for the

latter. Manikandan *et al.* employed a simple coprecipitation technique to prepare polycrystalline  $\text{V}_2\text{O}_5/\text{Na}_{0.33}\text{V}_2\text{O}_5$  with different molar ratios of  $\text{VOSO}_4 \cdot x\text{H}_2\text{O}$  and  $\text{NaOH} : \text{V1}$  (1 : 2),  $\text{NaOH} : \text{V2}$  (1 : 1), and  $\text{NaOH} : \text{V3}$  (1 : 0.1).<sup>103</sup> The capacitive behaviors (phase angle) of V1 ( $-60^\circ$ ), V2 ( $-55^\circ$ ), and V3 ( $-62^\circ$ ) were lower than that of an ideal capacitor ( $-90^\circ$ ) in the low-frequency region. In the high-frequency region, the electrode showed a broad peak, representing a decrease in the diffusion resistance of the ions into the electrode, further indicating V2 exhibited low resistance, as shown in Fig. 7i. However, the V2 electrode showed comparatively low cycling stability (62%) than V1 (96%) and V3 (85%) electrodes in the GCD cycles.

Nowadays, the synthesis of two materials cannot meet the needs of researchers. The development of high-performance materials has been attempted by compounding materials with good properties. Jayalakshmi introduced  $\text{SnO}_2\text{-V}_2\text{O}_5$  composites by a hydrothermal method in an autoclave, while  $\text{SnO}_2\text{-V}_2\text{O}_5\text{-CNT}$  composites were prepared by the simple mixture of CNTs and the oxides.  $\text{SnO}_2\text{-V}_2\text{O}_5\text{-CNT}$  composites exhibited the highest specific capacitance when compared with those of CNT,  $\text{V}_2\text{O}_5$ , and  $\text{V}_2\text{O}_5\text{-CNT}$  at a scan rate of  $100 \text{ mV s}^{-1}$  either as anodic or cathodic materials.<sup>104</sup> The presence of  $\text{SnO}_2$  improved the electronic and redox properties of  $\text{V}_2\text{O}_5$  in the composites. More importantly, there were synergistic interactions among the three structural components, namely,  $\text{SnO}_2$ ,  $\text{V}_2\text{O}_5$ , and CNT. Guo *et al.* synthesized  $\text{V}_2\text{O}_5/\text{PEDOT}/\text{MnO}_2$  nanosheets, consisting of layered  $\text{V}_2\text{O}_5$ , PEDOT as the conducting polymer, and layered  $\text{MnO}_2$ .<sup>105</sup> The fabrication of these composites is shown in Fig. 7b. In ASCs (Fig. 7h) with  $\text{V}_2\text{O}_5/\text{PEDOT}/\text{MnO}_2$  nanosheets as the cathode and activated carbon as the anode in 1 M  $\text{Na}_2\text{SO}_4$  aqueous electrolyte, capacitance retention of 93.5% could be observed with an energy density of  $39.2 \text{ W h kg}^{-1}$ . When  $\text{V}_2\text{O}_5$  was combined with metal oxides and carbon materials or conducting polymer, its electrochemical performance was considerably improved.

Recently, nanocomposites in which  $\text{V}_2\text{O}_5$  has been combined with various materials (carbon materials, conductive polymers, or metal compounds) have seen improvements in several aspects such as material structure, flexibility, and electrochemical performance. Further, the  $\text{V}_2\text{O}_5$  system is relatively complete as compared to other vanadium oxides ( $\text{VO}_2$  and  $\text{V}_2\text{O}_3$ ). However, practical applications are the subject of our research, and fabricating high-performance products is our pursuit.

## 5 VN and its composite materials

### 5.1 VN materials

Transition-metal-nitrite-based SCs electrodes have garnered considerable attention as high-capacity energy storage materials, wide potential range (1.2 V), and low cost as compared to those obtained from traditional TMOs (Table 5). The impressive electrochemical performance of VNs can be attributed to the combination of its high electronic conductivity and redox reactions provided by a few layers of vanadium oxides or oxynitrides on the surface. The former is responsible for fast electronic transmission and the latter, high pseudocapacitance.



Table 5 Comparison of various types of VN and its nanocomposites as electrode materials for use in SCs

Nano-structures (dimension)	Synthetic method	Electrolyte	Potential window (V)	Maximum SC	Current density	Cycling stability (%)	Ref.
VN (0D)	Temperature-programmed method	1 M KOH	-0.2-0.6	186 F g <sup>-1</sup>	1 A g <sup>-1</sup>	—	106
VN (0D)	Temperature-programmed reaction method	0.1 M KOH	-1.1-0.1	—	—	93% (2700 cycles)	107
Porous VN NW (1D)	Hydrothermal method	LiCl/PVA gel	-1.2-0.0	298.5 F g <sup>-1</sup>	10 mV s <sup>-1</sup>	95% (10 000 cycles)	34
VN nanofibers (1D)	Electrospinning method	LiCl/PVA gel	0.0-1.0	110.8 F g <sup>-1</sup>	5 mV s <sup>-1</sup>	75.1% (2000 cycles)	108
Nano-VN/IPC	Surface-initiated electrochemical mediated ATRP and heat-treatment approach	2 M KOH	-1.2-0.0	284 F g <sup>-1</sup>	0.5 A g <sup>-1</sup>	65% (10 000 cycles)	109
m-IPC@VN	Ultra-concentrated emulsion polymerization technology	6 M KOH	-1.2-0.0	260 F g <sup>-1</sup>	0.5 A g <sup>-1</sup>	91.1% (1000 cycles)	110
VNNDs/CNSs	Hydrothermal method	KOH/PVA	-1.0-0.1	1203.6 F cm <sup>-3</sup>	1.1 A cm <sup>-3</sup>	90% (10 000 cycles)	111
VN/CNT	ECR-PECVD	0.5 M K <sub>2</sub> SO <sub>4</sub>	-1.0-0.4	37.5 mF cm <sup>-2</sup>	2 mV s <sup>-1</sup>	85% (20 000 cycles)	112
Porous VN NWs/CNTF	One-step hydrothermal process	PVA-KOH	-1.2~-0.2	196.43 mF cm <sup>-2</sup>	1 mA cm <sup>-2</sup>	87.9% (4000 cycles)	113
VN-MWCNT materials	Chemical method	0.5 M Na <sub>2</sub> SO <sub>4</sub>	-0.9-0.0	160 F g <sup>-1</sup>	2 mV s <sup>-1</sup>	80% (1000 cycles)	114
VN/CF	Hydrothermal and annealing method	6 M KOH	-1.2-0.0	800 F g <sup>-1</sup>	4 A g <sup>-1</sup>	92.9% (10 000 cycles)	116
VN@CNWAs/CNT fiber	Two-step approach	1 M Na <sub>2</sub> SO <sub>4</sub>	-1.2~-0.2	715 mF cm <sup>-2</sup>	1 mA cm <sup>-2</sup>	90% (6000 cycles)	117
VN/NC nanocomposites	—	2 M KOH	-1.2-0.0	299 F g <sup>-1</sup>	1 A g <sup>-1</sup>	74.8% (5000 cycles)	118
VN-G	CVD	PVA/KOH gel	0.0-1.0	53 F g <sup>-1</sup>	10 mV s <sup>-1</sup>	90% (3000 cycles)	42
VN/GO composites	SI-eATRP technique	2 M KOH	-1.2-0.0	109.7 F g <sup>-1</sup>	1 A g <sup>-1</sup>	93% (5000 cycles)	119
VN/N-doped graphene nanocomposites	Two-step heating method	2 M KOH	-1.0-0.2	342.1 F g <sup>-1</sup>	0.5 A g <sup>-1</sup>	—	120
VN/NG composite	Modified Hummers method	6 M KOH	-1.0-0.0	445 F g <sup>-1</sup>	1 A g <sup>-1</sup>	98.66% (10 000 cycles)	121
Ni/VN HHMS	Solvothermal and annealing method	2 M KOH	-1.0-0.0	143.2 F g <sup>-1</sup>	0.5 A g <sup>-1</sup>	87% (1000 cycles)	122
3-Ni/VN/NGs-7 composite	Calcining method	2 M KOH	-1.2-0.0	236 F g <sup>-1</sup>	1 A g <sup>-1</sup>	85.8% (5000 cycles)	123
Core-shell TiN-VN fibers	Electrospinning and annealing method	1 M KOH	-1.2~-0.2	262 F g <sup>-1</sup>	2 mV s <sup>-1</sup>	88% (500 cycles)	124
TiVN composite	Solvothermal method	6 M KOH	-0.6-0.2	729 F g <sup>-1</sup>	2 A g <sup>-1</sup>	85.9% (300 cycles)	125

Glushenkov *et al.* prepared porous, nanocrystalline VN by the temperature-programmed  $\text{NH}_3$  reduction of  $\text{V}_2\text{O}_5$ .<sup>106</sup> The SEM image of the initial  $\text{V}_2\text{O}_5$  nanorods is shown in Fig. 7f. Fig. 7g shows porous VN nanorods with a pore size ranging from 15 to 110 nm. VN exhibited acceptable rate capabilities in three aqueous electrolytes (1 M  $\text{H}_2\text{SO}_4$ , 1 M KOH, and 3 M NaCl solutions). The highest capacitance was  $186 \text{ F g}^{-1}$  at the current density of  $1 \text{ A g}^{-1}$  in 1 M KOH electrolyte. Moreover, Djire *et al.* fabricated nanostructured VN using the same method.<sup>107</sup> The capacitance retention of VN materials in 0.1 M KOH/ $\text{H}_2\text{O}$  was over 93% after 2700 cycles, indicating good electrochemical stability. VN, as an anode material for use in SCs, undergoes irreversible electrochemical oxidation reaction to generate vanadium oxide ( $\text{VO}_x$ ) in aqueous solutions. Lu *et al.* proposed a strategy to improve the stability of NWs by using PVA-LiCl gel electrolytes for asymmetric quasi-solid-state SCs with VN NW anodes and  $\text{VO}_x$  NW cathodes.<sup>34</sup> VN NWs, uniformly interlaced with  $\text{VO}_x$  NWs after nitridation, exhibits a high specific area. Fig. 7j shows essentially the same shape as the scan rate increases from 10 to  $100 \text{ mV s}^{-1}$ , indicating good capacitive behavior of VN NWs. Evidently, the PVA-LiCl gel electrolyte prominently improves the stability of the VN electrode when compared with the 5 M LiCl aqueous electrolyte, with extremely high capacitance retention of 95.3% after 10 000 cycles, as

shown in Fig. 7k. Zhang *et al.* synthesized polyporous VN nanofibers by a facile electrospinning method and calcination at  $550 \text{ }^\circ\text{C}$  (specific capacitance:  $110.8 \text{ F g}^{-1}$ ) for symmetric all-solid-state SCs, which had higher cycling stability and exhibited higher specific capacitance than those of VN nanofibers synthesized at  $600 \text{ }^\circ\text{C}$  (specific capacitance:  $71.5 \text{ F g}^{-1}$ ) and  $650 \text{ }^\circ\text{C}$  (specific capacitance:  $76.0 \text{ F g}^{-1}$ ).<sup>108</sup>

## 5.2 VN/carbon-based materials

The small specific surface area limits the number of electroactive sites for capacitive storage, resulting in compromised capacitance. Ran *et al.* successfully developed a novel method combining surface-initiated electrochemically mediated atom transfer radical polymerization (ATRP) technology and heat treatment process to synthesis a material for use as the negative electrode in nano-VN/interconnected porous carbon (Nano-VN/IPC), affording a specific surface area of  $483 \text{ m}^2 \text{ g}^{-1}$ .<sup>109</sup> This electrode retained high specific capacitance of  $284 \text{ F g}^{-1}$  at  $0.5 \text{ A g}^{-1}$ , with an ultrahigh energy density of  $35.6 \text{ Wh kg}^{-1}$  and power density of  $362.5 \text{ W kg}^{-1}$  in 2 M KOH. The hybrid composite of IPC@VN consisting of VN nanoparticles (VNNPs) on the surface of porous carbon was reported by Zhang *et al.*<sup>110</sup> The m-IPC@VN was obtained by thermal treatment at a temperature of  $600 \text{ }^\circ\text{C}$  for 90 min under a constant heating

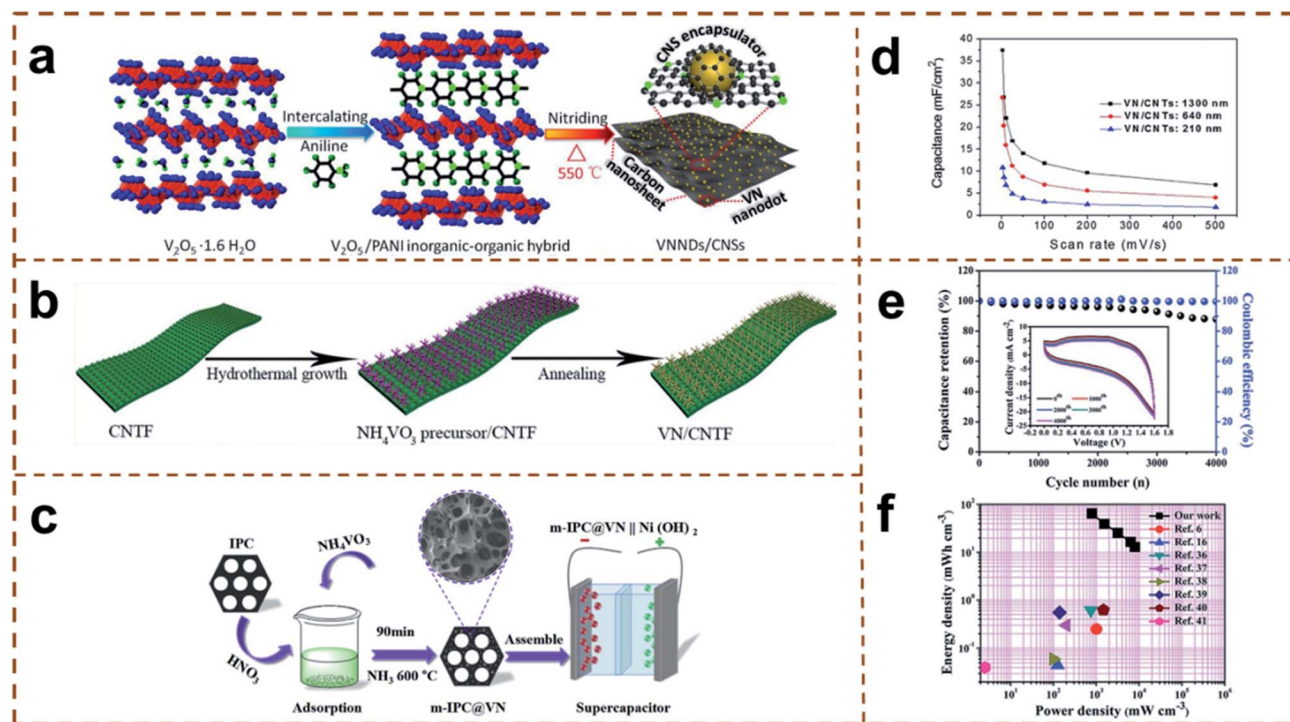


**Fig. 8** (a) Schematic illustration of the preparation procedures of VNNDs/CNSs from PANI-intercalated organic-inorganic  $\text{V}_2\text{O}_5 \cdot 1.6\text{H}_2\text{O}$  hybrid nanosheets. (b) Schematic of the process used to fabricate porous VN NWs on a CNTF substrate. (c) Schematic illustration of the adsorption of vanadate ions and preparation of electrode materials for use in SCs. (d) Normalized areal capacitance vs. scan rate of VN/CNTs with different thicknesses of VN coatings. (e) Cycling stability (black-ball line) and Coulombic efficiency (blue-ball line) of a  $\text{ZnCo}_2\text{O}_4/\text{VN}$  ASC device over 4000 cycles; inset shows the CV curves obtained for different numbers of cycles at a scan rate of  $100 \text{ mV s}^{-1}$ . (f) Ragone plot (power density vs. energy density) of the assembled ASC device. (a) Reprinted with permission.<sup>111</sup> Copyright 2018, Elsevier. (b, e, and f) Reprinted with permission.<sup>112</sup> Copyright 2017, Elsevier. (c) Reprinted with permission.<sup>110</sup> Copyright 2019, Elsevier. (d) Reprinted with permission.<sup>113</sup> Copyright 2017, The Royal Society of Chemistry.

rate of  $5\text{ }^{\circ}\text{C min}^{-1}$  in an ammonia atmosphere. Fig. 8c shows the process of vanadate ion adsorption and electrode preparation. An ASC was assembled with  $\text{Ni}(\text{OH})_2$  and m-VN/IPC electrodes as the positive and negative electrodes, respectively, and exhibited high specific capacitance of  $129\text{ F g}^{-1}$  at a current density of  $1\text{ A g}^{-1}$ . Li *et al.* synthesized spatially confined composites of VN nanodots intercalated with carbon nanosheets (VNNDS/CNSs).<sup>111</sup> The preparation procedure is shown in Fig. 8a. The VNNDS/CNS electrode showed ultrahigh volumetric capacitance of  $1203.6\text{ F cm}^{-3}$  at  $1.1\text{ A cm}^{-3}$  and high rate capability of  $703.1\text{ F cm}^{-3}$  at  $210\text{ A cm}^{-3}$  in comparison to those of CNS and mesoporous VN nanosheet (VNNS) materials, as well as extraordinary cycling stability with 90% capacitance retention after 10 000 cycles.

Recently, it has been found that different preparation methods can affect the surface area, crystallite size, surface oxidation states, and oxygen content of the material, which directly determine the capacitance. Ouldhamadouche *et al.* used the electron cyclotron resonance (ECR)-plasma-enhanced CVD (PECVD) process to synthesize a composite of nano-tree-like VN and CNTs.<sup>112</sup> From Fig. 8d, it is evident that the capacitance increased with the thickness of the VN deposit, and only 15% capacity decayed after 15 000 and 20 000 consecutive cycles at a scan rate of  $200\text{ mV s}^{-1}$ , indicating its long-term electrochemical stability. Zhao *et al.* fabricated a porous VN NW/CNT film (CNTF) *via* a facile one-step hydrothermal process,

followed by a thermal annealing process.<sup>113</sup> The synthesis of VN NW/CNTF is shown in Fig. 8b. The all-solid-state flexible ASC device, which comprised porous VN NWs/CNTF as the negative electrode material, cabbage-like  $\text{ZnCo}_2\text{O}_4/\text{CNTF}$  as the positive electrode material, and PVA/KOH gel electrolyte as the separator, exhibited capacity retention of 87.9% and Coulombic efficiency of 100% after 4000 cycles, as shown in Fig. 8e. Fig. 8f shows that the energy density of the device can reach as high as  $64.76\text{ mW h cm}^{-3}$  at a power density of  $800\text{ mW cm}^{-3}$ . Composite materials, containing fibrous VNNPs and MWCNTs, were developed by Su *et al.* using a chemical method.<sup>114</sup> They found that VNNPs coated on the MWCNT matrix enhanced the electrochemical performance.<sup>115</sup> However, the capacitance decreased with an increase in the VN mass loading. A hybrid cell assembled with VN-MWCNT as the negative electrode and  $\text{MnO}_2$ -MWCNT as the positive electrode afforded an energy density of  $38.7\text{ W h g}^{-1}$  ( $19.4\text{ mW h cm}^{-3}$ ) and power density of  $7.3\text{ W kg}^{-1}$  ( $\text{mW cm}^{-3}$ ) in a voltage window of 1.8 V in 0.5 M  $\text{Na}_2\text{SO}_4$  aqueous electrolyte.

During cycling, the instability of transition metal nitrides can be attributed to the presence of oxygen- and/or water-containing electrolytes, which leads to lowered capacitance. An *et al.* proposed a novel structure comprising VN-encapsulated CF networks with furrowed porous surfaces prepared by electrospinning followed by optimal stabilization and carbonization treatments (Fig. 9h).<sup>116</sup> Commercial VNs have

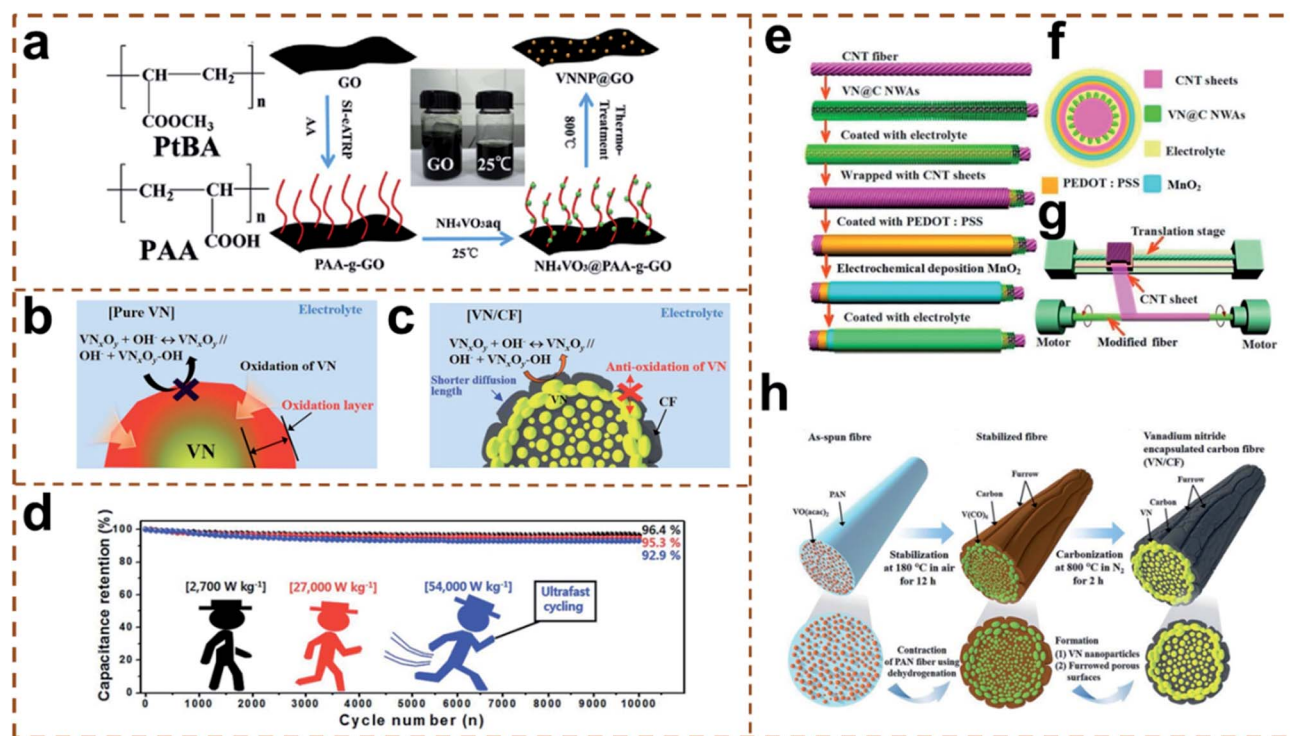


Fig. 9 (a) Schematic illustration of the VNNP@GO fabrication strategy. (b) Illustration of electrochemical reactions for a commercial VN. (c) VN/CF. (d) Cycling stabilities at different current densities of 4, 40, and  $80\text{ A g}^{-1}$  ( $2700$ ,  $27\text{ }000$ , and  $54\text{ }000\text{ W kg}^{-1}$ ) over 10 000 cycles. (e) Schematic illustration of the fabrication of ACFSS. (f) Cross-sectional structure of the ACFSS. (g) Wrapping of an aligned CNT sheet around modified CNT fiber. (h) Schematic illustrations of the syntheses of as-spun fibers, stabilized fibers, and VN/CF. (a) Reprinted with permission.<sup>119</sup> Copyright 2018, Elsevier. (b–d, and h) Reprinted with permission.<sup>116</sup> Copyright 2017, The Royal Society of Chemistry. (e–g) Reprinted with permission.<sup>117</sup> Copyright 2017, American Chemical Society.

low specific capacitances, because they can be easily oxidized in oxygen and/or water; this impedes the electrochemical reaction of VNs, as shown in Fig. 9b. Meanwhile, as shown in Fig. 9c, a CF coating prevents the oxidation of VN. When tested as an electrode for use in SCs, a VN-CF electrode exhibited excellent cycling stability with superb capacitance retentions of 96.4, 95.3, and 92.9% at current densities of 4, 40, and 80 A g<sup>-1</sup>, respectively, even after 10 000 cycles, as shown in Fig. 9d. Zhang *et al.* developed a facile and effective approach to directly grow well-aligned 3D VN NWAs on CNT fibers for assembling fiber-shaped SCs (FSSs).<sup>117</sup> The areal specific capacitance of the VN@C NWA/CNT electrode was 715 mF cm<sup>-2</sup> at a current density of 1 mA cm<sup>-2</sup>. When manufacturing a prototype asymmetric coaxial FSS (ACFSS) (Fig. 9e–g) with the maximum operating voltage of 1.8 V, the CNT fiber core coated with VN@C NWAs was used as the negative electrode, achieving 90% capacitance retention after 6000 cycles. In addition, the ACFSS device was woven into the flexible powering textile, which demonstrated favorable stitchability.

Nitrogen-doped carbon (NC) has attracted great attention due to its excellent hydrophilic properties as well as high electrical conductivity and electrochemical stability. As a supporting skeleton, NC nanosheets (NCS) are beneficial to prevent the aggregation of VNNPs and improve the cycling life and electrical conductivity of the composites. Jiang *et al.* prepared VN/NC nanocomposites using g-C<sub>3</sub>N<sub>4</sub> as the nitrogen source by a facile one-step annealing process.<sup>118</sup> For X-VN/NCB, X-VN/NCS2, X-VN/

NCS4, and X-VN/NCS6, NCB refers to NCS synthesized from bulk g-C<sub>3</sub>N<sub>4</sub>; NCS2, NCS4, and NCS6 indicate NCS obtained from g-C<sub>3</sub>N<sub>4</sub> nanosheets with different thickness *via* thermal exfoliation of bulk g-C<sub>3</sub>N<sub>4</sub> for 2, 4, and 6 h, respectively; and “X” denotes the mass of NH<sub>4</sub>VO<sub>3</sub>. The specific capacitances of 0.06-VN/NCS2, 0.04-VN/NCS2, 0.03-VN/NCS2, NCS2, and commercial VN electrodes at a current density of 1 A g<sup>-1</sup> were 137, 299, 187, 28, and 16 F g<sup>-1</sup>, respectively. Even after 5000 cycles, 72% of the initial capacitance of the 0.04-VN/NCS2 composite electrode could be retained, suggesting an exceptional cycling life.

Recently, flexible quasi-/all-solid-state SCs as flexible energy storage systems have aroused considerable interest due to their high power density, long cycling life, ease of operation, excellent reliability upon deformation, and cost-effectiveness. However, a reliable, flexible electrode, an important component of SCs, should have both high electrical conductivity and excellent mechanical robustness. A composite material comprising carbon-based materials (graphene) with low specific capacitance and VN with high capacitance and high electrical conductivity was prepared by Yu *et al.* and utilized as flexible quasi-/all-solid-state SC electrodes. This VN-G electrode showed high specific capacitance and good cycling stability, with capacity retention of 90% after 3000 cycles in KOH/PVA solid electrolyte.<sup>42</sup> More importantly, the VN-G material delivered favorably high sensitivity (40 kPa<sup>-1</sup> in the range of 2–10 kPa), fast response time (~130 ms), and outstanding stability under static and dynamic pressure conditions, which indicated that it

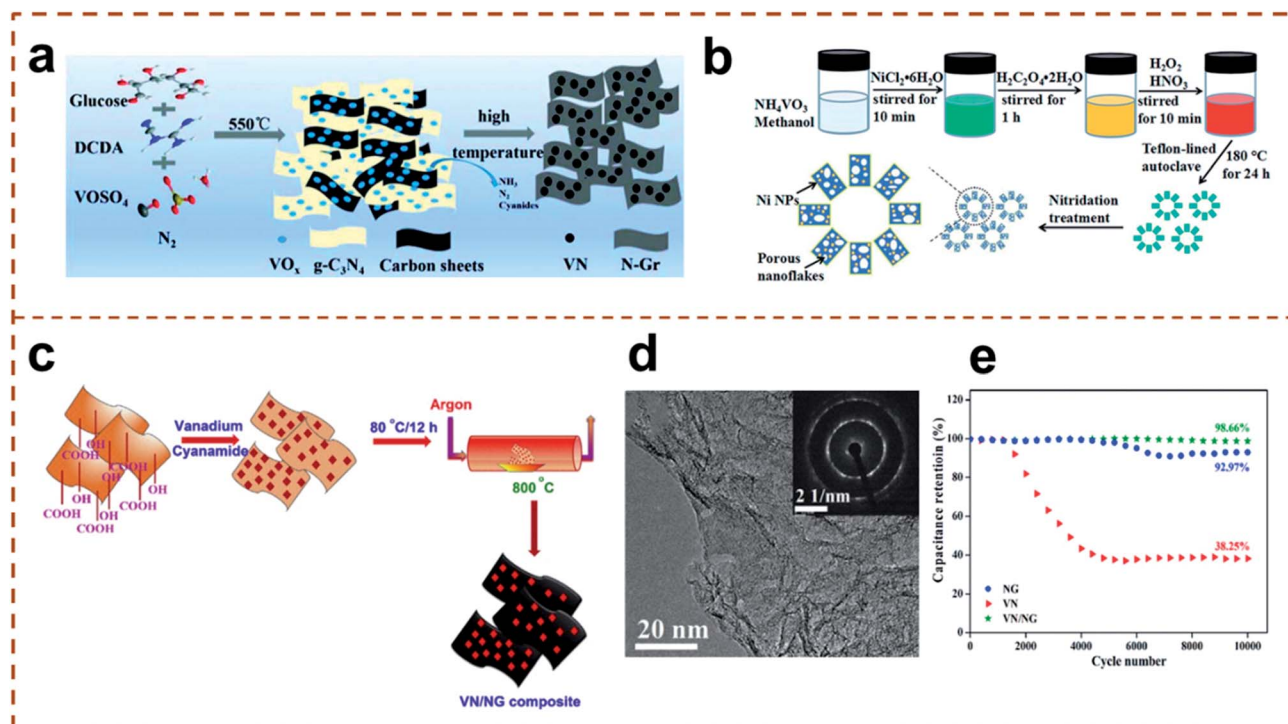


**Fig. 10** (a) Schematic illustration of the preparation of VN/N-G nanocomposites. (b) Schematic for the synthesis of Ni<sub>1-x</sub>V<sub>x</sub>O<sub>2</sub> hierarchical hollow microspheres and the subsequent nitridation process. (c) Schematic illustration of the fabrication of VN/NG composites. (d) HRTEM images of VN/NG composites. (e) Cyclic stability of the as-synthesized NG, VN and VN/NG composite as a function of cycle number. (f) TEM of Ti<sub>2</sub>V<sub>1</sub>-HMs. (a) Reprinted with permission.<sup>120</sup> Copyright 2019, The Partner Organisations. (b) Reprinted with permission.<sup>122</sup> Copyright 2016, The Royal Society of Chemistry. (c and d) Reprinted with permission.<sup>121</sup> Copyright 2016, Elsevier. (e and f) Reprinted with permission.<sup>125</sup> Copyright 2018, IOP.

could detect various physiological signals for ultrasensitive health monitoring applications.

Graphene oxide (GO), as an energy-related substrate, affords excellent electrical, mechanical, and thermal properties. He *et al.* were the first to use a method combining the electrochemically controlled surface-initiated atom transfer (SI-eATRP) technique and thermal treatment to synthesize VNNP/GO.<sup>119</sup> The fabrication process is shown in Fig. 9a. The synergistic effect of VN and GO significantly improved the electrochemical properties. The specific capacitance of VNNP@GO retained 109.7 F g<sup>-1</sup> at 1 A g<sup>-1</sup> and the capacitance retention rate still reached 93% of the initial capacity after 5000 cycles.

To improve the electrochemical performance of VN/G, N doping plays an indispensable role with regard to energy storage. Liu *et al.* reported hybrid VN/N-doped graphene (VN/N-G) nanocomposites by the pyrolysis of a mixture of GO, V(IV) oxide sulfate hydrate, and cyanamide in a N<sub>2</sub> atmosphere.<sup>120</sup> Fig. 10a shows the preparation of VN/N-G nanocomposites. By means of an *in situ* method, N could be uniformly doped in the carbon matrix; heat treatment under NH<sub>3</sub> gas could be performed only at the defect sites and/or the edges of the carbon matrix. In addition, the calcination temperature could considerably influence the structure, VN<sub>x</sub>O<sub>y</sub>, and content of N dopant in VN/N-G, as well as the corresponding electrochemical performance. It was found that VN/N-G at 700 °C exhibited high specific capacitance of 342.1 F g<sup>-1</sup> at 0.5 A g<sup>-1</sup> in 2 M KOH aqueous electrolyte. Balamurugan *et al.* synthesized a novel VN/nitrogen-doped graphene (VN/NG) composite (Fig. 10c) using a modified Hummers' method.<sup>121</sup> Fig. 10d shows the high-resolution transmission electron microscopy (HRTEM) image indicating the thin layer of porous VN nanostructure homogeneously distributed on the NG surface. When applied as an electrode, the as-prepared composites exhibited excellent storage capacity, with specific capacitance of 445 F g<sup>-1</sup> at 1 A g<sup>-1</sup>, wide operation window (-1.2 to 0 V), and capacity retention of 98.44% after 10 000 cycles at 10 A g<sup>-1</sup> (Fig. 10e).

### 5.3 VN/transition metal materials

Although VN has large theoretical specific capacitance, reversible Faradaic redox response, and low cost, its low conductivity and inefficient ionic transport are still a significant challenge. By designing 3D hierarchical architectures and performing conductive addition, it is possible to resolve this problem. Ji *et al.*, utilizing Ni nanoparticles as the conductive additive, doped Ni nanoparticles into VN 3D hierarchical hollow microspheres with 2–4 nm mesopores and surface area of 57.3 m<sup>2</sup> g<sup>-1</sup> along with the nitridation treatment of Ni<sub>1-x</sub>V<sub>x</sub>O<sub>2</sub> material.<sup>122</sup> The synthesis process is shown in Fig. 10b. Assembled Ni/VN//Ni<sub>1-x</sub>V<sub>x</sub>O<sub>2</sub> ASC exhibited excellent cycling stability, with 87% specific capacitance retention after 1000 cycles. To improve the electrochemical performance of VN materials, Jiang *et al.* synthesized the X-Ni/VN/NCs-Y (X denotes the mass percentage of Ni nanoparticles; Y indicates the mole ratios of melamine to VNNPs) composite with ultrasized Ni nanoparticles and VNNPs embedded in NC nanosheets.<sup>123</sup> The 3-Ni/VN/NCs-7 nanocomposite with a large specific area (58 m<sup>2</sup> g<sup>-1</sup>) and even pore

size (about 22 nm) afforded rapid ion/molecule transport pathways and exhibited specific capacitance of 236 F g<sup>-1</sup> at 1 A g<sup>-1</sup> along with superb cycling stability.

Transition metal nitrides are desirable candidates for use in SCs due to their low cost, high molar density, and superior chemical resistance. However, titanium nitride (TiN) showed better electronic conductivity, but with a lower capacity. Therefore, utilizing VN with high capacity and TiN *via* coaxial electrospinning and subsequent annealing in ammonia, Zhou *et al.* obtained core-shell (TiN-VN) fibers with surface area of 169 m<sup>2</sup> g<sup>-1</sup> and average pore size of 30.2 nm.<sup>124</sup> The TiN-VN fiber afforded higher specific capacitance (2 mV s<sup>-1</sup>, 247.5 F g<sup>-1</sup>) and better rate capability (50 mV s<sup>-1</sup>, 160.8 F g<sup>-1</sup>). Wei *et al.* introduced TiVN-composite-based hollow mesospheres (HMs) by combining the higher capacitance of VN and higher electronic conductivity of TiN *via* a facile solvothermal method employing nitridation by C<sub>3</sub>N<sub>4</sub>.<sup>125</sup> According to the different molar ratios of Ti/V of 1 : 1, 2 : 1, and 3 : 1, three TiVN-HM samples were prepared, which were denoted as Ti<sub>1</sub>V<sub>1</sub>-HMs, Ti<sub>2</sub>V<sub>1</sub>-HMs, and Ti<sub>3</sub>V<sub>1</sub>-HMs, respectively. Fig. 10e and f show that these nanospheres were homogeneously distributed with a diameter of about 100 nm, and displayed hollow structure with a shell thickness of 15 nm. Moreover, the Ti<sub>2</sub>V<sub>1</sub>-HM sample exhibited high specific capacitance of 729 F g<sup>-1</sup> at 2 A g<sup>-1</sup>.

In summary, various preparation methods can be used to produce VN materials with good cycling stability. Although many research mechanisms concerning VN have been put forward, various theories are still controversial, which necessitate more theoretical calculations and technical proofs. Moreover, it is very difficult to produce VN materials on a large scale because certain synthesis conditions are difficult to realize. Therefore, a preparation technique with low energy consumption and high yield should be formulated.

## 6 Vanadium sulfide and its composites

### 6.1 VS<sub>2</sub> and its composites

VS<sub>2</sub> is considered to be a promising candidate for SCs applications because it affords very high electrical conductivity, high surface area, and unique electronic structure, which can be attributed to the fact that VS<sub>2</sub> can essentially maintain a V-shaped structure and layered crystals stacked by van der Waals forces (Table 6). Pandit *et al.* successfully used the successive ionic layer adsorption and reaction (SILAR) method to deposit VS<sub>2</sub> thin films onto flexible and lightweight stainless steel substrates (Fig. 11c).<sup>126</sup> When assembled into a flexible symmetric solid-state SC device, the VS<sub>2</sub> electrode exhibited strong cycling stability by retaining 89% of its initial capacitance after 6000 cycles and affording specific energy density of 25.9 W h kg<sup>-1</sup> at a specific power density of 1.5 kW kg<sup>-1</sup>. Feng *et al.* developed a unique ammonia-assisted strategy to obtain VS<sub>2</sub> thin films with less than five S-V-S single layers for the construction of high-performance in-plane SCs.<sup>127</sup> The process of fabricating the thin film is shown in Fig. 11d-f. In the 150 nm in-plane configuration, VS<sub>2</sub> thin films can afford capacitance of

Table 6 Comparison of various types of vanadium sulfide and its nanocomposites as electrode materials for use in SCs

Nano-structures (dimension)	Synthetic method	Electrolyte	Potential window (V)				Cycling stability (%)	Ref.
			Potential window (V)	Maximum SC	Current density			
VS <sub>2</sub> thin film (2D)	SILAR	2 M KCl	-0.6-0.2	247 F g <sup>-1</sup>	0.5 mA cm <sup>-2</sup>	89% (6000 cycles)	126	
VS <sub>2</sub> nanosheets (2D)	Hydrothermal	BMIMBF <sub>4</sub> -PVA	-0.6-0.6	317 F g <sup>-1</sup>	0.1 A m <sup>-2</sup>	90% (1000 cycles)	127	
VS <sub>2</sub> nanoplates (2D)	Colloidal	1 M KOH	-0.2-0.8	2200 F g <sup>-1</sup>	1 A g <sup>-1</sup>	85% (5000 cycles)	128	
ZnO/VS <sub>2</sub> nanocomposite	A simple solution	2 M KOH	-0.3-0.7	2695.7 F g <sup>-1</sup>	1 A g <sup>-1</sup>	92.7% (5000 cycles)	130	
NiCo <sub>2</sub> S <sub>4</sub> @VS <sub>2</sub>	Hydrothermal	3 M KOH	0.0-0.6	1023.4 C g <sup>-1</sup>	0.45 A g <sup>-1</sup>	96% (2000 cycles)	35	
VS <sub>4</sub> /CNTs composite	Hydrothermal	1 M LiClO <sub>4</sub>	-1.2-1.2	330 F g <sup>-1</sup>	1 A g <sup>-1</sup>	63% (5000 cycles)	131	
VS <sub>4</sub> /rGO	Modified Hummer	1 M Na <sub>2</sub> SO <sub>4</sub>	-0.1-0.8	877 F g <sup>-1</sup>	0.5 A g <sup>-1</sup>	90% (1000 cycles)	132	
VS <sub>4</sub> /CNTs/rGO hybrid	Hydrothermal	0.5 M K <sub>2</sub> SO <sub>4</sub>	-0.8-0.8	558.7 F g <sup>-1</sup>	1 A g <sup>-1</sup>	97% (1000 cycles)	133	
VS <sub>4</sub> -CC@VS-3	Hydrothermal	1 M [EMIM] [OTf]	0.0-2.0	536 mF cm <sup>-2</sup>	1 mA cm <sup>-2</sup>	93% (1000 cycles)	134	
VS <sub>4</sub> /rGO/CoS <sub>2</sub> @Co	Hydrothermal	1 M KOH	-0.2-0.55	1353 F g <sup>-1</sup>	0.625 A g <sup>-1</sup>	89.6% (20 000 cycles)	135	

4760  $\mu\text{F cm}^{-2}$  in a PVA gel with the water-soluble ionic liquid of BMIMBF<sub>4</sub>. Meanwhile, no obvious degradation of capacitance could be observed even after 1000 charge/discharge cycles, revealing their excellent cycling behavior. Guo *et al.* prepared ultrathin VS<sub>2</sub> nanoplates by a colloidal method.<sup>128</sup> When utilized as the anode materials for a three-electrode system, these defect-rich nanoplates exhibited ultrahigh specific capacitance of 2200 F g<sup>-1</sup> at a current density of 1 A g<sup>-1</sup>. From Fig. 11g, it is evident that two ASCs (VS<sub>2</sub>//AC) can light an OUC light-emitting diode (LED) panel for at least 10 min, demonstrating its promising application potential.

However, VS<sub>2</sub> nanosheets are vulnerable to stacking and aggregating into multilayers during the drying process owing to the high surface energy and interlayer van der Waals

attraction, which leads to dramatic changes in their physical and chemical properties, particularly a decrease in the number of active sites as well as electrical conductivity. Zhang *et al.* constructed a novel type of nonaqueous Na-ion hybrid micro-supercapacitor with a wide potential window (0.01–3.5 V) and ultrahigh areal energy density using VS<sub>2</sub> nanosheets grown on electrochemically exfoliated graphene as the negative electrode and activated carbon as the positive electrode in a nonaqueous sodium-ion electrolyte.<sup>129</sup> The as-fabricated nonaqueous Na-ion hybrid MSC exhibited excellent cyclability of up to 5000 cycles without capacitance fading. Further, the areal capacitance reached 110.7 mF cm<sup>-2</sup> at 0.2 mA cm<sup>-2</sup> and the areal energy density could be as high as 188.3  $\mu\text{W h cm}^{-2}$  at 0.35 mW cm<sup>-2</sup>.

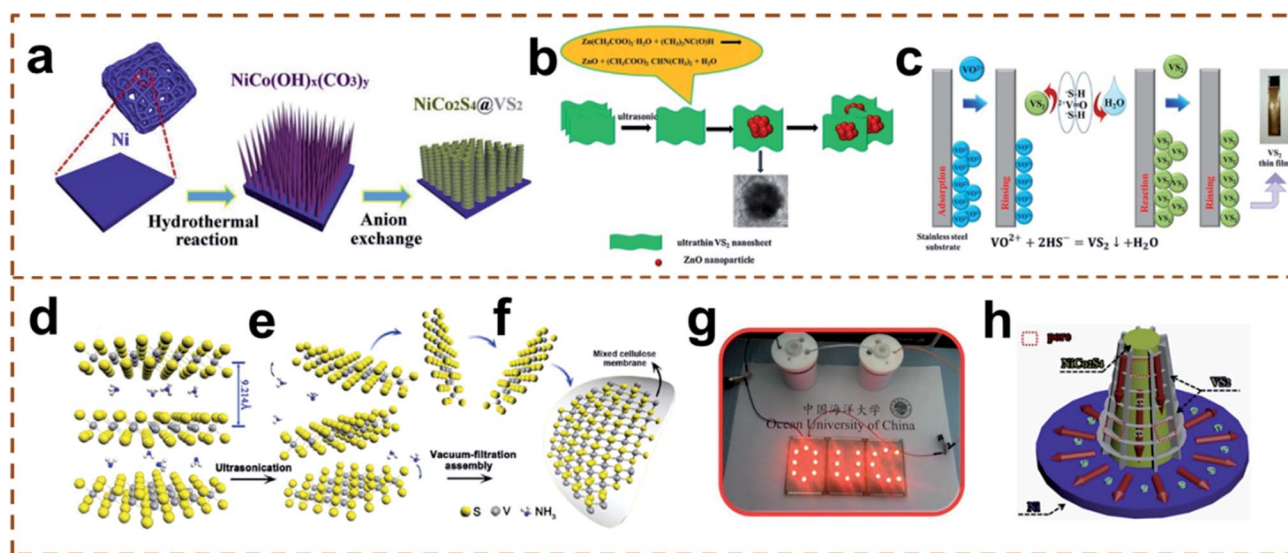


Fig. 11 (a) Schematic illustration of the synthesis of NiCo<sub>2</sub>S<sub>4</sub>@VS<sub>2</sub>. (b) Schematic illustration of the chemical synthesis of VS<sub>2</sub> by the SILAR method. (c) VS<sub>2</sub> precursor with NH<sub>3</sub> molecules intercalated into the S–V–S layers. (d) Effusion of NH<sub>3</sub> molecules away from the stacked layers, breaking down the c-axis periodicity and resulting in the formation of ultrathin VS<sub>2</sub> nanosheets. (e) Vacuum-filtration assembly of the as-synthesized VS<sub>2</sub> nanosheets into transferrable thin films on mixed cellulose membranes. (f) Schematic diagram of the formation of the ZnO/VS<sub>2</sub> nanoarchitecture. (g) Two ASCs were connected in series to light an OUC LED panel. (h) Schematic illustration of the charge storage and transfer characteristics of NiCo<sub>2</sub>S<sub>4</sub>@VS<sub>2</sub>. (a and h) Reprinted with permission.<sup>35</sup> Copyright 2018, Elsevier. (b) Reprinted with permission.<sup>126</sup> Copyright 2018, Elsevier. (c) Reprinted with permission.<sup>127,130</sup> Copyright 2016, Elsevier. (d–f) Reprinted with permission.<sup>115</sup> Copyright 2011, American Chemical Society. (g) Reprinted with permission.<sup>128</sup> Copyright 2018, The Royal Society of Chemistry.

ZnO has the advantages of high theoretical capacitance, high energy density, and low cost, but it exhibits poor conductivity and low mechanical stability. Therefore, Fang *et al.* synthesized cauliflower-like nanocomposites by growing ZnO nanospheres *in situ* on ultrathin VS<sub>2</sub> nanosheets using a facile wet chemical method.<sup>130</sup> Fig. 11b shows the schematic diagram of the formation of the ZnO/Vs<sub>2</sub> nanoarchitecture. The ZnO/Vs<sub>2</sub> nanocomposite afforded an ultrahigh specific capacity of 2695.7 F g<sup>-1</sup> at a current density of 1 A g<sup>-1</sup> with remarkable stability, where 92.7% of its capacity could be retained after 5000 cycles due to the synergetic effects. Zhang *et al.* fabricated 2D VS<sub>2</sub> nanosheets along with NiCo<sub>2</sub>S<sub>4</sub> needle arrays (NiCo<sub>2</sub>S<sub>4</sub>@VS<sub>2</sub>) *via* an *in situ* sulfurization-assisted hydrothermal process to prevent stacking as well as to increase the number of active sites.<sup>35</sup> Fig. 11a shows the synthesis route of freestanding NiCo<sub>2</sub>S<sub>4</sub>@VS<sub>2</sub> nanoneedle arrays on 3D sponge-like Ni foam. The large surface area, short ion transport path, and increased active sites for redox reactions contributed to an overall increase in capacity, as shown in Fig. 11h. NiCo<sub>2</sub>S<sub>4</sub>@VS<sub>2</sub> exhibited excellent SC performance, namely, high specific capacitance (1023.4 C g<sup>-1</sup> at a current density of 0.45 A g<sup>-1</sup>) and long-term cycling stability (96% capacitance retention after 2000 cycles).

## 6.2 VS<sub>4</sub> and its composites

VS<sub>4</sub> has a 1D crystal structure and high sulfur content when compared with transition metal sulfides such as MoS<sub>2</sub>, CoS<sub>2</sub>, and NiS<sub>2</sub>, which facilitates the charge transfer kinetics due to weak interactions between the neighboring chains, affording excellent electrochemical behavior (Table 6). Further, the interval between the atomic chains offers abundant active sites for ion diffusion and storage as well as high electric conductivity. However, the synthesis of pure VS<sub>4</sub> has not been investigated in the past. Recently, it was reported that pure VS<sub>4</sub> could be prepared by using carbon-based material as the active templates. VS<sub>4</sub>/CNT composites were reported by Wang *et al.* *via* a one-step hydrothermal reaction, whose preparation route is shown in Fig. 13d.<sup>131</sup> For 1 M LiClO<sub>4</sub> in a PPC electrolyte, the VS<sub>4</sub>/CNTs composite electrode delivered outstanding specific capacitance of 330 F g<sup>-1</sup> (924 C g<sup>-1</sup>) at 1 A g<sup>-1</sup> in the potential window from -1.4 V to 1.4 V. VS<sub>4</sub>/rGO containing 0.75, 1.5, and 3 wt% rGO were formulated by Ratha *et al.*, and they are hereafter referred to as VS<sub>4</sub>/rGO<sub>0.75</sub>, VS<sub>4</sub>/rGO<sub>1.5</sub>, and VS<sub>4</sub>/rGO<sub>3</sub>, respectively.<sup>132</sup> Among these, VS<sub>4</sub>/rGO<sub>1.5</sub> showed high specific capacitance of about 877 F g<sup>-1</sup> at a current density of 0.5 A g<sup>-1</sup> as compared to those of VS<sub>4</sub>/rGO<sub>0.75</sub> (223 F g<sup>-1</sup>) and VS<sub>4</sub>/rGO<sub>3</sub> (259 F g<sup>-1</sup>). To improve the performance of the electrode material, the VS<sub>4</sub>/CNTs/rGO hybrid was introduced by Ratha *et al.*<sup>133</sup> When compared with VS<sub>4</sub>/CNTs and VS<sub>4</sub>/rGO, the hybrid afforded excellent energy density and capacitance due to synergistic interactions between the CNTs and rGO in VS<sub>4</sub>/CNTs/rGO. In addition, binder-free flower-like patronite (VS<sub>4</sub>) nanostructures were synthesized on CC by a facile hydrothermal method; then, VS<sub>4</sub>-CC@VS-3 (mass loading of VS<sub>4</sub> on CC: 1.3 mg cm<sup>-2</sup>) was obtained by controlling the concentrations of V and sulfur sources along with the complexing agent in the growth solution, as performed by Ramu *et al.*<sup>134</sup> In addition,

the VS<sub>4</sub>-CC@VS-3 electrodes in SSCs exhibited better areal capacitance retention of ~93% even after 1000 cycles in 1 M 1-ethyl-3-methylimidazolium trifluoromethanesulfonate ([EMIM][OTf]) electrolyte. To further improve the electrochemical properties, Wang *et al.* synthesized hierarchical VS<sub>4</sub>/rGO/CoS<sub>2</sub>@Co (VRCS@Co) nanocomposite (Fig. 13a) with multidimensional structures by *in situ* synthesis on Co foam *via* a simple one-step hydrothermal process in the presence of GO.<sup>135</sup> The nanocomposite exhibited high capacitance of 274.3 mA h g<sup>-1</sup> (1353 F g<sup>-1</sup>) at 0.625 A g<sup>-1</sup> (Fig. 13e). Fig. 13f shows that the specific capacitance retention of the VRCS@Co cathode was 89.6% even after 20 000 cycles, while those of GO + NaVO<sub>3</sub>@Co (VRC@Co) and thiourea (3) + NaVO<sub>3</sub>@Co (VCS@Co) were 42% and 63.2% after 10 000 cycles. Evidently, the outstanding cycling stability could be attributed to the unique architecture of 0D CoS<sub>2</sub> spheres anchored on 2D VS<sub>4</sub> lamellae.

## 7 Metal vanadate and its composite materials

### 7.1 Cobalt vanadate and its composites

Cobalt vanadate and its composites are well-known SC materials because of their natural abundance, environment-friendliness, low cost, and better chemical properties (Table 7). A variety of morphologies and structures have been achieved, such as 3D porous hydrated cobalt pyrovanadate microflowers,<sup>136</sup> CoV<sub>2</sub>O<sub>6</sub> micron blocks,<sup>137</sup> Co<sub>3</sub>V<sub>2</sub>O<sub>8</sub> nanoparticles,<sup>137</sup> and so on. The electrochemical performance of cobalt vanadate is affected by the valence of V (conductivity), morphology, crystallinity, crystal structure, and mass loading in the composites. A cobalt-vanadate-based electrode stores electric charges *via* the pseudocapacitive mechanism. Charge storage arises from the changes in the II/III oxidation states at or near the surface of the cobalt vanadate nanostructures.

To store electric charge, a faradaic reaction occurs on the electrode surface, which is the adsorption/desorption of the electrolyte ions and/or protons on the electrode surface, whereas the bulk pseudocapacitive reaction depends on the intercalation/deintercalation process of either protons or cations into the bulk of cobalt vanadate. Sun *et al.* prepared 3D porous Co<sub>2</sub>V<sub>2</sub>O<sub>7</sub>·3.3H<sub>2</sub>O microflowers by a facile coprecipitation method.<sup>136</sup> Fig. 12a shows the fabrication of these microflowers. The specific capacitance was 351 F g<sup>-1</sup> at a current density of 1 A g<sup>-1</sup>, and an ultralong cycling lifetime could be obtained with 103% capacitance retention after 30 000 cycles (Fig. 12e). Teng *et al.* were the first to use a microwave-assisted hydrothermal method to synthesize CoV<sub>2</sub>O<sub>6</sub> micron blocks and CoV<sub>2</sub>O<sub>8</sub> nanoparticles.<sup>137</sup> When used as the electrode, CoV<sub>2</sub>O<sub>8</sub> nanoparticles exhibited a higher specific capacity as compared to that of CoV<sub>2</sub>O<sub>6</sub> micron blocks. Meanwhile, the specific capacities of CoV<sub>2</sub>O<sub>6</sub> and CoV<sub>2</sub>O<sub>8</sub> were 81.91 and 94.67% of the initial values after 1000 cycles. It was found that CoV<sub>2</sub>O<sub>8</sub> nanoparticles exhibited better cycling stability. As a new class of high-performance electrode material for use in SCs, Co<sub>3</sub>V<sub>2</sub>O<sub>8</sub> nanoparticles were designed and synthesized by Liu *et al.*, and they found that the specific capacitance was 505 F g<sup>-1</sup> at

Table 7 The comparison of various mixed metal vanadates nanostructures as electrode materials for SCs

Nano-structures (dimension)	Synthetic method	Electrolyte	Potential window (V)	Maximum SC	Current density	Cycling stability (%)	Ref.
Co <sub>3</sub> V <sub>2</sub> O <sub>8</sub> nanoparticles (0D)	Microwave-assisted hydrothermal synthesis method	6 M KOH	0.0–0.6	159.7 C g <sup>-1</sup>	1 mA cm <sup>-2</sup>	94.6% (1000 cycles)	137
Co <sub>3</sub> V <sub>2</sub> O <sub>8</sub> nanoparticles (0D)	Co-preparation method	2 M KOH	–0.2–0.6	505 F g <sup>-1</sup>	0.625 A g <sup>-1</sup>	92.6% (1000 cycles)	138
BiVO <sub>4</sub> nanoparticles (0D)	—	KOH	–0.6–0.8	1166 F g <sup>-1</sup>	1 A g <sup>-1</sup>	85% (500 cycles)	153
Zn <sub>2</sub> V <sub>2</sub> O <sub>7</sub> (1D)	Hydrothermal method	6 M KOH	0.0–0.6	427.7 F g <sup>-1</sup>	1 mA cm <sup>-2</sup>	83.71% (1000 cycles)	151
Co <sub>3</sub> V <sub>2</sub> O <sub>8</sub> thin sheets (2D)	Hydrothermal	6 M KOH	–0.2–0.7	1320 F g <sup>-1</sup>	1 A g <sup>-1</sup>	89.1% (10 000 cycles)	36
Ni <sub>3</sub> V <sub>2</sub> O <sub>8</sub> nanoflake (2D)	Dropwise	2 M KOH	–0.2–0.6	1181 F g <sup>-1</sup>	0.625 A g <sup>-1</sup>	92.6% (1000 cycles)	138
Ni <sub>3</sub> V <sub>2</sub> O <sub>8</sub> thin sheets (2D)	Hydrothermal method	6 M KOH	–0.2–0.7	1992.5 F g <sup>-1</sup>	1 A g <sup>-1</sup>	83.9% (10 000 cycles)	36
3D porous hydrated cobalt pyrovanadate microflowers (3D)	Co-preparation method	2 M KOH	–0.1–0.5	351 F g <sup>-1</sup>	1 A g <sup>-1</sup>	103% (3000 cycles)	136
CoV <sub>2</sub> O <sub>6</sub> micron blocks (3D)	Microwave-assisted hydrothermal synthesis method	6 M KOH	0.0–0.6	114.1 C g <sup>-1</sup>	1 mA cm <sup>-2</sup>	81.91% (1000 cycles)	137
Aluminum vanadate (3D)	Hydrothermal method	1.0 M Na <sub>2</sub> SO <sub>4</sub>	0.0–1.0	497 F g <sup>-1</sup>	1 A g <sup>-1</sup>	89% (10 000 cycles)	156
3D Co <sub>3</sub> O <sub>4</sub> /Co <sub>3</sub> (VO <sub>4</sub> ) <sub>2</sub> hybrid nanorods	Hydrothermal-annealing	2 M KOH	–0.2–0.5	847.2 F g <sup>-1</sup>	0.5 A g <sup>-1</sup>	99.3% (5000 cycles)	139
3D urchin-shaped Ni <sub>3</sub> (VO <sub>4</sub> ) <sub>2</sub> hollow nanospheres	Hydrothermal method	6 M KOH	0.0–0.5	402.8 C g <sup>-1</sup>	1 A g <sup>-1</sup>	88% (1000 cycles)	141
Co-incorporated NiV <sub>2</sub> O <sub>6</sub> /Ni(HCO <sub>3</sub> ) <sub>2</sub> nanoflake grown on nickel foam	Hydrothermal method	6 M KOH	–0.2–0.7	7.94 F cm <sup>-2</sup>	1 mA cm <sup>-2</sup>	106.2% (10 000 cycles)	145
NiO/Ni <sub>3</sub> V <sub>2</sub> O <sub>8</sub> nanocomposite	Solvochemical method.	—	0.0–0.6	653 F g <sup>-1</sup>	1 A g <sup>-1</sup>	96% (1000 cycles)	144
Ni <sub>3</sub> V <sub>2</sub> O <sub>8</sub> @PANI composite	Situ chemical bath method	2 M KOH	–0.2–0.6	2565.7 F g <sup>-1</sup>	5 mV s <sup>-1</sup>	88% (20 000 cycles)	142
Ni <sub>3</sub> V <sub>2</sub> O <sub>8</sub> /NG	Hydrothermal technique	3 M KOH	–0.1–0.6	1898 F g <sup>-1</sup>	1 A g <sup>-1</sup>	83.3% (20 000 cycles)	140
Co <sub>3</sub> V <sub>2</sub> O <sub>8</sub> -Ni <sub>3</sub> V <sub>2</sub> O <sub>8</sub> nanocomposite	Hydrothermal method	6 M KOH	–0.2–0.7	2617.5 F g <sup>-1</sup>	1 A g <sup>-1</sup>	91.4% (10 000 cycles)	36
Co <sub>3</sub> V <sub>2</sub> O <sub>8</sub> -Ni <sub>3</sub> V <sub>2</sub> O <sub>8</sub> thin layers@porous carbon nanofibers	Hydrothermal method	3 M KOH	–0.1–0.6	1731 F g <sup>-1</sup>	1 A g <sup>-1</sup>	85.5% (3000 cycles)	146
Graphene-Zn <sub>3</sub> V <sub>2</sub> O <sub>8</sub> nanocomposites	Solvochemical process	2 M KOH	–1.0–1.0	564 F g <sup>-1</sup>	0.8 A g <sup>-1</sup>	85% (5000 cycles)	152
GR/BiVO <sub>4</sub>	Hydrothermal method	2 M NaOH	–1.1–0.7	479 F g <sup>-1</sup>	5 A g <sup>-1</sup>	91% (2500 cycles)	154
rGO/BiVO <sub>4</sub>	Hydrothermal method	6 M KOH	–1.0–0.6	115 F g <sup>-1</sup>	0.15 mA cm <sup>-2</sup>	80.3% (2000 cycles)	155
Li <sub>3</sub> VO <sub>4</sub> /carbon nanofibers	Solid-state method	Li ion conducting gel polymer electrolyte	0.2–2.0	178 F g <sup>-1</sup>	0.6 A g <sup>-1</sup>	86% (2400 cycles)	158



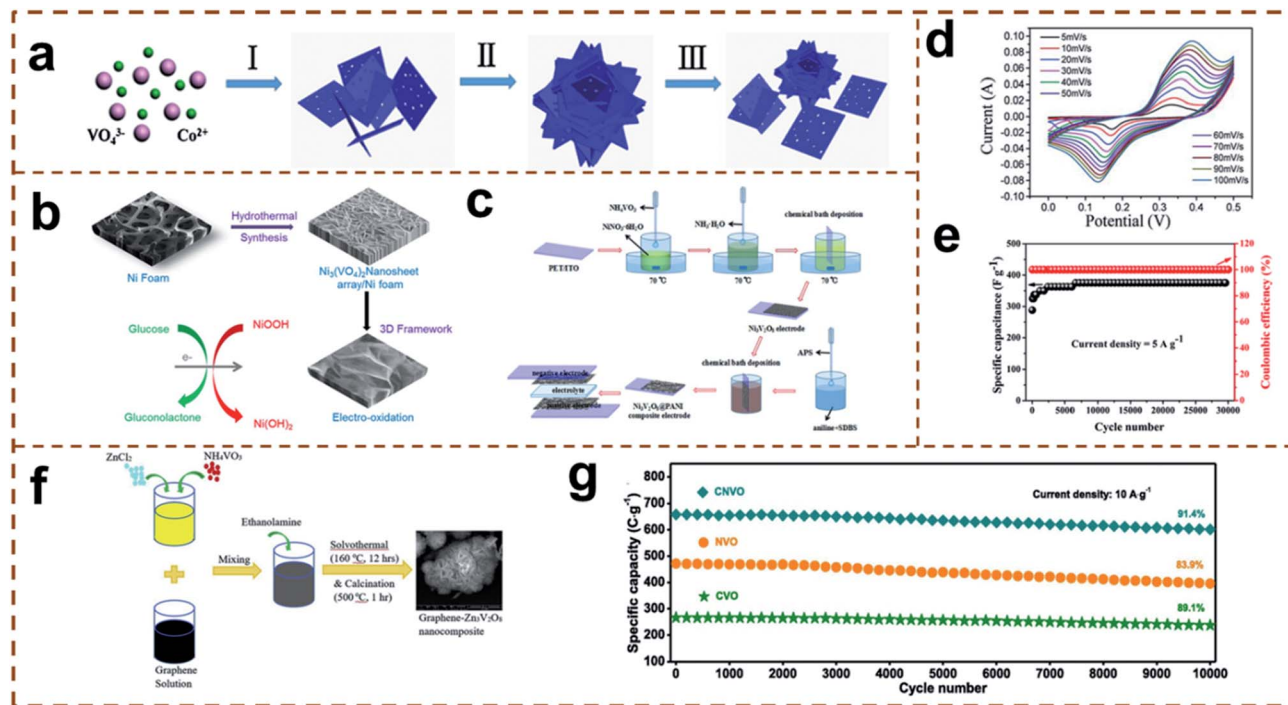


Fig. 12 (a) Schematic illustration of the formation processes of the 3D porous  $\text{Co}_2\text{V}_2\text{O}_7 \cdot 3.3\text{H}_2\text{O}$  microflowers. (b) Synthesis protocol adopted for preparation of  $\text{Ni}_3(\text{VO}_4)_2$  nanosheet arrays/Ni foam electrode and electrochemical sensing mechanism. (c) Schematic illustration of the synthesis of electrode materials and the fabrication of the device. (d) CV curve of  $\text{Ni}_3(\text{VO}_4)_2$  nanospheres at various scan rates. (e) Cycle test of the  $\text{Co}_2\text{V}_2\text{O}_7 \cdot 3.3\text{H}_2\text{O}$  microflowers at a current density of  $5 \text{ A g}^{-1}$ . (f) Schematic illustration of graphene-2D  $\text{Zn}_3\text{V}_2\text{O}_8$  hexagonal sheet nanocomposite via solvothermal approach. (g) Cycling performance over 10 000 GCD cycles at  $10 \text{ A g}^{-1}$ . (a and e) Reprinted with permission.<sup>136</sup> Copyright 2018, Elsevier. (b) Reprinted with permission.<sup>159</sup> Copyright 2018, ECS. (c) Reprinted with permission.<sup>143</sup> Copyright 2018, American Chemical Society. (d) Reprinted with permission.<sup>141</sup> Copyright 2016, The Royal Society of Chemistry. (f) Reprinted with permission.<sup>152</sup> Copyright 2019, Elsevier. (g) Reprinted with permission.<sup>36</sup> Copyright 2019, Elsevier.

a current density of  $0.625 \text{ A g}^{-1}$ .<sup>138</sup>  $\text{Co}_3\text{V}_2\text{O}_8$  thin sheets were used as the SC electrode material and were synthesized via a succinctly operated hydrothermal method by Huang *et al.*, affording a remarkable specific capacity of  $1320 \text{ F g}^{-1}$  at  $1 \text{ A g}^{-1}$  and superior cycling stability.<sup>36</sup> Zhang *et al.* synthesized 3D  $\text{Co}_3\text{O}_4/\text{Co}_3(\text{VO}_4)_2$  hybrid nanorods on the conductive substrate of Ni foam by the combination of hydrothermal synthesis and subsequent annealing treatment.<sup>139</sup> A 3D electrode of  $\text{Co}_3\text{O}_4/\text{Co}_3(\text{VO}_4)_2$  hybrid nanorod exhibited satisfactory capacitance of  $847.2 \text{ F g}^{-1}$ , outstanding rate capability, and excellent cycling stability.

## 7.2 Nickel vanadate and its composites

Nickel vanadate is a good electrochemical material for use in SCs, with a high theoretical capacity of up to  $1992.5 \text{ F g}^{-1}$ .<sup>36</sup> Nickel vanadate and its composites have long cycling stability, low cost, high electrical conductivity, and multiple oxidation states, making them a suitable candidate for SC applications.<sup>140</sup> Kumar *et al.* fabricated 3D urchin-shaped  $\text{Ni}_3(\text{VO}_4)_2$  hollow nanospheres by a facile, template-free hydrothermal method.<sup>141</sup> Fig. 12d shows the CV curves of  $\text{Ni}_3(\text{VO}_4)_2$  nanospheres at various scan rates ranging from 5 to  $100 \text{ mV s}^{-1}$ . A linear increase in the peak current with an increase in the scan rate suggests that the faradaic redox reaction kinetics and ionic and

electronic charge transports are rapid even at higher scan rates. Furthermore, the oxidation and reduction peak potentials shift toward positive and negative directions, respectively. In addition, the different morphologies of nickel vanadate show impressive electrochemical properties. Porous urchin-shaped  $\text{Ni}_3(\text{VO}_4)_2$  nanosphere electrodes exhibit a specific capacity of  $402.8 \text{ C g}^{-1}$  at  $1 \text{ A g}^{-1}$ , and they have enhanced rate capability and capacity retention of 88% after 1000 cycles. Further, 2D hierarchical porous nickel vanadate thin sheets were synthesized by Huang *et al.* via a succinctly operated hydrothermal method, affording a specific capacity of  $1992.5 \text{ F g}^{-1}$  at a current density of  $1 \text{ A g}^{-1}$  and capacity retention of 83.9% after 10 000 cycles.<sup>36</sup>  $\text{Ni}_3\text{V}_2\text{O}_8$  was synthesized by Liu *et al.*, which afforded high specific capacitance ( $1181 \text{ F g}^{-1}$ ) at a current density of  $0.625 \text{ A g}^{-1}$ , but only 73% of the capacitance could be retained after 1000 cycles.<sup>138</sup> In addition, 3D nanosheet arrays of  $\text{Ni}_3(\text{VO}_4)_2$  directly grown on Ni foam via a facile one-step hydrothermal route were used as the electrode for nonenzymatic glucose detection. The irreversible catalytic oxidation of glucose into gluconolactone was catalyzed by the  $\text{Ni}(\text{OH})_2/\text{NiOOH}$  redox couple, as shown in Fig. 13b.<sup>142</sup> The electrode possessed high sensitivity and selectivity along with long-term stability, good flexibility, and better reusability. The  $\text{Ni}_3\text{V}_2\text{O}_8@\text{PANI}$  composite prepared by Liu *et al.* using an *in situ* CBD method afforded outstanding electrochemical behaviors

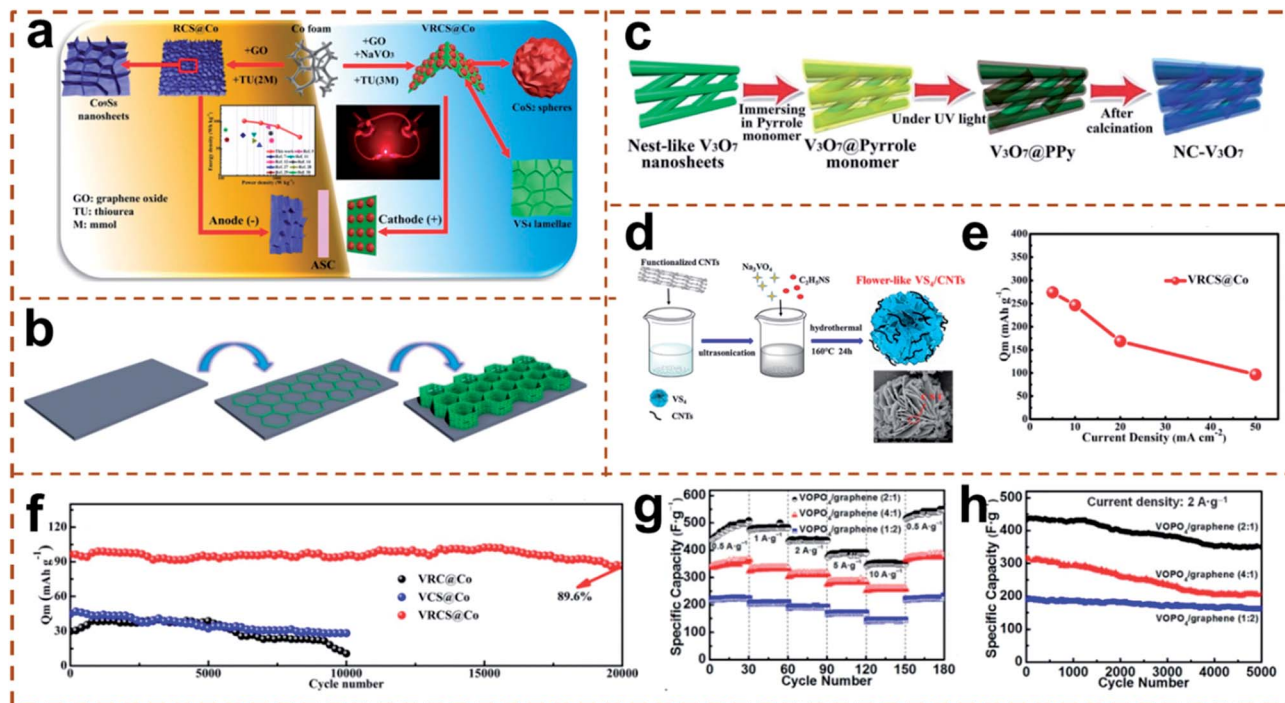


**Fig. 13** (a) Preparation of VRCS@Co cathode and RCS@Co anode, and the assembly of ASC. (b) Schematic synthesis process for nest-like  $V_3O_7$ . (c) Schematic illustration of the formation procedure of the nest-like NC- $V_3O_7$  nanosheets self-assembled by NWs. (d) Schematic illustration of the preparation of  $VS_4/CNTs$  composites. (e) Discharge rate curves of VRCS@Co. (f) GCD tests of VRCS@Co. (g) Rate performance of  $VOPO_4/graphene$  composites. (h) Cycling performance of  $VOPO_4/graphene$  composites. (a, e and f) Reprinted with permission.<sup>135</sup> Copyright 2019, Elsevier. (b) Reprinted with permission.<sup>142</sup> Copyright 2018, The Royal Society of Chemistry. (c, g and h) Reprinted with permission.<sup>163</sup> Copyright 2017, Elsevier. (d) Reprinted with permission.<sup>151</sup> Copyright 2019, Elsevier.

(specific capacitance of  $2565.7 \text{ F g}^{-1}$  at  $5 \text{ mV s}^{-1}$ , wide potential window, and good rate capability).<sup>143</sup> Fig. 12c shows a schematic illustration of the synthesis of electrode materials as well as device fabrication. Size- and shape-controlled nickel oxide/nickel vanadate ( $NiO/Ni_3V_2O_8$ ) nanocomposites were obtained by the solvothermal method; the electrode afforded specific capacitance of  $653 \text{ F g}^{-1}$  at a current density of  $1 \text{ A g}^{-1}$  due to the regular arrangement of nanorods with uniform size distribution.<sup>144</sup> Co-incorporated  $NiV_2O_6/Ni(HCO_3)_2$  nanoflakes grown on Ni foam showed superior long-term durability, retaining 106.2% of the initial capacity after 10 000 charge/discharge cycles at  $100 \text{ mA cm}^{-2}$ .<sup>145</sup>

Cobalt vanadate and nickel vanadate afford good electrochemical performances (Table 7). Therefore, what are the properties obtainable by combining cobalt vanadate and nickel vanadate. Our group reported the synthesis of 2D hierarchical porous  $M_3V_2O_8$  ( $M = Co, Ni, \text{ and } Co-Ni$ ) thin sheets and the obtained thin sheets-based electrode possessed specific capacitance of  $2617.5 \text{ F g}^{-1}$ .<sup>36</sup> As shown in Fig. 12g, the  $Co_3V_2O_8-Ni_3V_2O_8$  nanocomposite demonstrated higher capacity retention (91.4%) after 10 000 cycles in comparison to those of  $Co_3V_2O_8$  and  $Ni_3V_2O_8$ . In addition, mesoporous  $Co_3V_2O_8-Ni_3V_2O_8$  thin layers@porous CNFs were fabricated by Hosseini *et al.* for use in flexible all-solid-state SCs.<sup>146</sup> They showed cycling stability of 88.5% capacitance retention after 3000 cycles at  $5.0 \text{ A g}^{-1}$ .

### 7.3 Other mixed metal vanadates

Other mixed metal vanadates have rarely been studied for use in SCs in the past, such as zinc vanadate, aluminum vanadate, bismuth vanadate, and so on. Zinc vanadate has been studied and affords good performances with regard to several characteristics, namely, photocatalytic properties,<sup>147,148</sup> luminescence characteristics,<sup>149</sup> properties in lithium batteries,<sup>13</sup> hydrogen storage properties,<sup>148</sup> and magnetic properties.<sup>150</sup> However, there are challenges in the study of the pseudocapacitive properties of zinc vanadate, such as complex and time-consuming synthesis,<sup>150</sup> as well as poor electrochemical properties (low specific capacitance and poor cycling performance).<sup>151</sup> Zinc vanadate was particularly studied due to its different morphologies (hierarchical microspheres, nanosheets, NWs, and so on) and its various binding modes ( $Zn_3V_2O_8$ ,  $Zn_3(OH)_2V_2O_7 \cdot 2H_2O$ ,  $Zn_2V_2O_7$ , and so on).

$Zn_3(OH)_2V_2O_7 \cdot 2H_2O$  NWs were successfully synthesized *via* a facile, rapid, and green microwave-assisted hydrothermal method; its electrode afforded specific capacitance of  $207.8 \text{ F g}^{-1}$  at a scan rate of  $1 \text{ mA cm}^{-2}$ , but could only retain 53.50% of its initial capacitance.<sup>151</sup> As-synthesized  $Zn_2V_2O_7$  elliptical nanoparticles as the electrode afforded superior specific capacitance of  $427.7 \text{ F g}^{-1}$  (at  $1 \text{ mA cm}^{-2}$ ) and enhanced cycling performance, with 83.71% capacitance retention after 1000 cycles. Low *et al.* reported that graphene- $Zn_3V_2O_8$  nanocomposites were subjected to a facile solvothermal process and

then thermal annealing.<sup>152</sup> The synthesis of this nanocomposite is shown in Fig. 12f. The specific capacitance of this nanocomposite was  $564 \text{ F g}^{-1}$  at  $0.8 \text{ A g}^{-1}$  in  $2 \text{ M KOH}$  aqueous electrolyte. Furthermore, the materials showed outstanding rate capability and good cycling stability even after 5000 cycles.

$\text{BiVO}_4$ , an n-type semiconducting material, is abundant, relatively inexpensive, and offers a broad range of oxidation states, and therefore, it has become a superior candidate for SC applications. Packiaraj *et al.* synthesized  $\text{BiVO}_4$  nanoparticles by a simple hydrothermal method.<sup>153</sup> When used as an electrode for use in SCs,  $\text{BiVO}_4$  nanoparticles yielded the maximum capacitance value of  $1166 \text{ F g}^{-1}$  at  $1 \text{ A g}^{-1}$ . However,  $\text{BiVO}_4$  has the disadvantage of poor electrical conductivity as a metal oxide. It is very important to combine carbon-based materials with high electrical conductivity with  $\text{BiVO}_4$ . Graphene/bismuth vanadate composites were introduced *via* a hydrothermal process by Deng *et al.*<sup>154</sup> The specific surface area was  $36 \text{ m}^2 \text{ g}^{-1}$  and the average pore size was about  $23.5 \text{ nm}$ . The GR/ $\text{BiVO}_4$  monolith composite yielded impressive specific capacitance of  $479 \text{ F g}^{-1}$  in a potential window from  $-1.1$  to  $0.7 \text{ V}$ . Similarly, fabricating rGO/ $\text{BiVO}_4$  hybrid nanostructures, obtained by Patil *et al.*, afforded outstanding volumetric energy density of  $1.6 \text{ mW h cm}^{-3}$  ( $33.7 \text{ W h kg}^{-1}$ ) and ensured rapid energy delivery with a power density of  $391 \text{ mW cm}^{-3}$  ( $8.0 \text{ kW kg}^{-1}$ ).<sup>155</sup>

Amorphous TMOs may exhibit unique physical and chemical properties with more active sites and isotropic active sites due to their disordered structures. Further, aluminum vanadate is one of the few species used in SCs. Amorphous aluminum vanadate with hierarchical microspheres were developed *via* a simple hydrothermal approach by Yan *et al.*<sup>156</sup> The electrode made of this material showed specific capacitance of  $497 \text{ F g}^{-1}$  at  $1 \text{ A g}^{-1}$  and good stability with capacity retention of 89% after 10 000 cycles.

Li-ion capacitors were introduced for the first time in 2001 and they have attracted considerable attention because they are a bridge between electrochemical capacitors and Li-ion batteries.<sup>157</sup> Wang *et al.* developed a quasi-solid-state Li-ion capacitor with  $\text{Li}_3\text{VO}_4$ -based composites as the anode and

electrochemically exfoliated graphene sheets as the cathode in a gel polymer electrolyte.<sup>158</sup> A power density of  $3870 \text{ W kg}^{-1}$  at an energy density of  $28 \text{ W h kg}^{-1}$  could be achieved even in a gel polymer electrolyte.

The synthesized mixed metal vanadates for use in SCs have afforded good electrochemical performance, and their specific capacity was higher than those of vanadium oxide, vanadium sulfides, and VNs; therefore, they are the most promising V-based material. Therefore, many mixed metal vanadates are worth developing for use in SCs.

## 8 Other V-based materials

Vanadium oxide has higher theoretical specific capacitance and wider potential window than those of other TMOs owing to the multiple oxidation states of V ( $\text{V}^{2+}$ ,  $\text{V}^{3+}$ ,  $\text{V}^{4+}$ , and  $\text{V}^{5+}$ ). Nest-like  $\text{V}_3\text{O}_7$  was comprehensively investigated with regard to its energy storage mechanism. Evidently,  $\text{V}_3\text{O}_7$  was converted into  $\text{V}_6\text{O}_{13}$  at the lowest potential of  $-0.6 \text{ V}$  and into  $\text{V}_2\text{O}_5$  at the highest potential of  $0.2 \text{ V}$  (Table 8). By annealing the precursor of  $\text{V}_3\text{O}_7$ @PPy prepared by an *in situ* photopolymerization method, NC-coated nest-like  $\text{V}_3\text{O}_7$  (NC- $\text{V}_3\text{O}_7$ ) was fabricated by Zhao *et al.*<sup>159</sup> The synthesis of NC- $\text{V}_3\text{O}_7$  NWs is shown in Fig. 12b. NC- $\text{V}_3\text{O}_7$  retained 80.47% of the initial capacitance at  $10 \text{ A g}^{-1}$  after 4000 cycles, which was much higher than that of  $\text{V}_3\text{O}_7$  (23.16%). It was found that this superior capacitance and stability could be attributed to the unique three-layered structure (C was bonded to both V and N) stabilized by  $\text{V}_3\text{O}_7$  and it consequently supported high-speed ionic and electronic transmission channels.

$\text{V}_6\text{O}_{13}$  has aroused widespread interest because of its high specific capacitance and good cycling ability for lithium batteries, but it is rarely used in SCs. Meanwhile,  $\text{V}_6\text{O}_{13}$  has the blended valence of  $\text{V}(\text{iv})$  and  $\text{V}(\text{v})$ , thereby increasing the electronic conductivity of the material. Zeng *et al.* utilized a thermal decomposition and quenching method with  $\text{NH}_4\text{VO}_3$  as the starting material, affording  $\text{V}_6\text{O}_{13}$  sheets with an average size of  $2 \mu\text{m}$  and thickness of about  $200 \text{ nm}$ .<sup>160</sup> The  $\text{V}_6\text{O}_{13}$  electrode

Table 8 The comparison of other vanadium-based materials as electrode materials for SCs

Nano-structures (Dimension)	Synthetic method	Electrolyte	Potential window (V)	Maximum SC	Current density	Cycling stability (%)	Ref.
Sulfur-doped $\text{V}_6\text{O}_{13-x}\text{NW}$ (1D)	Two-step process	5 M LiCl	$-1.0-0.0$	$1353 \text{ F g}^{-1}$	$1.9 \text{ A g}^{-1}$	47.7% (10 000 cycles)	161
$\text{V}_6\text{O}_{13}$ sheets (2D)	Thermal decomposing and quenching method	1 M $\text{NaNO}_3$	$-0.2-0.8$	$285 \text{ F g}^{-1}$	$50 \text{ mA g}^{-1}$	98% (300 cycles)	160
$\text{VOPO}_4 \cdot 2\text{H}_2\text{O}$ (2D)	Reflux method	6 M $\text{H}_3\text{PO}_4$	$0.0-1.0$	$184 \text{ F g}^{-1}$	$0.2 \text{ A g}^{-1}$	—	162
NC- $\text{V}_3\text{O}_7$	<i>In situ</i> photopolymerization method	1 M $\text{Na}_2\text{SO}_4$	$-0.6-0.2$	$660.63 \text{ F g}^{-1}$	$0.5 \text{ A g}^{-1}$	80.47% (4000 cycles)	159
$\text{VOPO}_4$ /graphene composite	Hydrothermal method,	1 M $\text{H}_2\text{SO}_4$	$-0.1-0.9$	$508 \text{ F g}^{-1}$	$0.5 \text{ A g}^{-1}$	80% (5000 cycles)	163
$\text{VOPO}_4$ /graphene film	Ultrasonication method	PVA/LiCl	$0.0-1.2$	—	—	96% (2000 cycles)	164
Vanadyl phosphate/rGO nanosheet	Controllable nanosheet reassemble technology	0.5 M $\text{K}_2\text{SO}_4$	$-0.5-0.3$	$378 \text{ F g}^{-1}$	$0.5 \text{ mV s}^{-1}$	64% (1000 cycles)	165
Vanadyl phosphate/carbon nanocomposites	—	6 M KOH	$-0.2-0.7$	$469 \text{ F g}^{-1}$	$1 \text{ A g}^{-1}$	77% (5000 cycles)	166

maintained obvious capacitance performance in the voltage range from  $-0.2$  to  $0.8$  V in  $1$  M  $\text{NaNO}_3$  electrolyte. Moreover, Zhai *et al.* reported the fabrication of sulfur-doped, oxygen-deficient  $\text{V}_6\text{O}_{13-x}$  via a two-step process and used it as the anode.<sup>161</sup> Capacitance of  $1353$   $\text{F g}^{-1}$  could be achieved at a current density of  $1.9$   $\text{A g}^{-1}$  in  $5$  M  $\text{LiCl}$  solution since the  $\text{Li}^+$  diffusion coefficient and charge transfer efficiency of the  $\text{V}_6\text{O}_{13-x}$  electrode were improved. However,  $\text{V}_6\text{O}_{13-x}$  was dissolved to form  $\text{V(III)}$  oxide as soluble vanadate ions during cycling in aqueous electrolytes, which resulted in rapid capacitance degradation. To suppress the irreversible chemical dissolution of  $\text{V}^{3+}$ , sulfur-doped, oxygen-deficient  $\text{V}_6\text{O}_{13-x}$  was deposited on a layer of carbonaceous thin film, which afforded outstanding capacitance retention of  $92.3\%$  after  $10\,000$  cycles.

$\text{VOPO}_4 \cdot 2\text{H}_2\text{O}$  was considered as a promising electrode material, which could be attributed to its peculiar layered structure (comprising  $\text{VO}_6$  octahedra and  $\text{PO}_4$  tetrahedra), safety, low cost, and environment-friendliness, and it possessed better potential than vanadium oxide. Luo *et al.* used reflux and hydrothermal methods to fabricate  $\text{VOPO}_4 \cdot 2\text{H}_2\text{O}$ , and they found that the material synthesized by the reflux method had better capacitance ( $202$   $\text{F g}^{-1}$  at  $2$   $\text{mV s}^{-1}$ ) than that obtained by the hydrothermal method ( $100$   $\text{F g}^{-1}$  at  $2$   $\text{mV s}^{-1}$ ), because the former electrode material had smaller resistance and faster pseudocapacitance reaction.<sup>162</sup> To prepare an amorphous  $\text{VOPO}_4/\text{graphene}$  composite, Chen *et al.* exfoliated bulk layered  $\text{VOPO}_4 \cdot 2\text{H}_2\text{O}$  crystals and then performed hydrothermal treatment with GO.<sup>163</sup> The amorphous  $\text{VOPO}_4$  structure shortened the ion transport path, offered more reversible and fast faradic reaction sites, and improved the unique layer-on-sheet nano-hybrid structure. The synthesis of amorphous  $\text{VOPO}_4/\text{graphene}$  composites is shown in Fig. 13c. Further, when compared with different masses of  $\text{VOPO}_4/\text{graphene}$  composites,  $\text{VOPO}_4/\text{graphene}$  ( $2:1$ ) composite electrodes exhibited good cycling stability (capacity retention of  $80\%$  after  $5000$  cycles at  $2$   $\text{A g}^{-1}$ ) than those of  $\text{VOPO}_4/\text{graphene}$  ( $1:2$ ) composites and  $\text{VOPO}_4/\text{graphene}$  ( $4:1$ ) composites. As shown in Fig. 13g, it is evident that the amorphous  $\text{VOPO}_4/\text{graphene}$  ( $2:1$ ) composite as an electrode material for use in SCs showed high specific capacitance ( $508$   $\text{F g}^{-1}$  at  $0.5$   $\text{A g}^{-1}$ ) and excellent rate capability ( $359$   $\text{F g}^{-1}$  at  $10$   $\text{A g}^{-1}$ ). By comparison,  $\text{VOPO}_4/\text{graphene}$  ( $2:1$ ) composite electrode still retained  $\sim 80\%$  of its original value after  $5000$  cycles, as shown in Fig. 13h. Wu *et al.* fabricated  $\alpha_1$ -vanadyl phosphate ultrathin nanosheets with less than six atomic layers and an inorganic graphene analog, which was constructed for use in flexible ultrathin-film SCs; it could afford high areal capacitance of  $8360.5$   $\text{mF cm}^{-2}$ .<sup>164</sup> In addition, the hybrid  $\text{VOPO}_4/\text{graphene}$  film was also prepared, demonstrating excellent long-term cycling stability ( $96\%$  after  $2000$  cycles). Similarly, different mass ratios of  $\text{VOPO}_4/\text{rGO}$  hybrids were introduced by He *et al.* by using a deintercalation–intercalation reaction process.<sup>165</sup> The electrode with a mass ratio of  $\text{VOPO}_4/\text{rGO} = 1$  showed high specific capacitance. Chen *et al.* synthesized vanadyl phosphate/carbon nanocomposites by a simple two-step approach, in which dodecylamine was intercalated with layered  $\text{VOPO}_4 \cdot 2\text{H}_2\text{O}$  and then *in situ* carbonization was performed at  $400$   $^\circ\text{C}$ .<sup>166</sup> According to the electrochemical

results, this nanocomposite electrode afforded high specific capacitance of  $469$   $\text{F g}^{-1}$  at a current density of  $1$   $\text{A g}^{-1}$  as well as excellent rate performance.

Vanadium carbide ( $\text{V}_2\text{CT}_x$ )-based MXenes have a wide working potential window and sloping charge/discharge when used in Li-ion batteries.  $\text{V}_2\text{CT}_x$  was proposed for Na-ion capacitors by Dall'Agnese *et al.*, which showed a potential window ranging from  $1$  to  $3.5$  V vs.  $\text{Na}^+/\text{Na}$ ; therefore, it has attractive applications as a positive electrode in Na-ion capacitors.<sup>167</sup>

## 9 Conclusion and outlook

Overall, this article describes the applications of V-based materials in SCs. Meanwhile, their syntheses, morphologies, and electrochemical performances are presented. V-based materials have attracted tremendous attention in electrochemistry due to their different valences, abundant resources, and low costs. However, their poor electrical conductivities, low structural stabilities, inferior rate performances, and low specific capacitances and energy densities limit their practical applications. Therefore, it is critical to design stable, porous, electrically conductive materials for use in SCs. According to various published articles, the future development direction of the material is as follows.

First, the development of new materials is still an important task in energy storage. So far, novel structures and hybrid materials have been mainly explored, which can enrich the library of materials and create good conditions for the further development of their properties. In this review, apart from  $\text{V}_2\text{O}_5$ , the remaining V-based materials should be fully combined with metal/metal compounds, carbon-based materials, and conductive polymers because these materials can correspondingly increase their specific surface areas, conductivities, and further increase their specific capacities, rate performances, cycling stabilities, and energy and power densities. Further,  $\text{V}_2\text{O}_5$  should further explore its corresponding novel composite materials. Moreover, for the same material, different synthesis methods can produce same or different morphologies, and the corresponding electrochemical properties are also very different. At present, there is no specific synthesis method or specific set of synthesis conditions for V-based materials such that they can have good performance. Therefore, a large number of experiments to explore new materials and synthesis methods are particularly important in future development.

Second, fabricating porous structured materials improves the specific surface area and active sites. High specific surface area can offer more active sites, increase the contact between the material and electrolyte, generate more redox reactions, and shorten the electron and ion transport paths. As mentioned above, these can considerably improve the energy storage performance of materials. Excellent electrochemical behavior, which is related to the nature of the material, is also correlated to the morphology and synthesis method. Porous materials can effectively improve the utilization rate of materials and accelerate the transmission of ions/electrons. However, according to the large number of reported publications, there are only a few materials with a high specific area. In order to resolve this

problem, nanoscale materials with a porous structure should be synthesized in future research.

Third, ASCs are assembled by developing new electrode materials and electrolytes. In ASCs, V-based materials are used as the positive/negative electrode, while new electrode materials are utilized as the negative/positive electrode; this can broaden the operating voltage window and enhance the electrochemical performance. Therefore, it is important to choose and develop new electrodes. Besides, the electrolyte has an influence on the electrochemical behavior. For some V-based materials, organic electrolytes exhibit better electrochemical performance than inorganic electrolytes. However, organic electrolytes are generally toxic and are not environmentally friendly for some applications. Environmentally friendly, deep, eutectic solvents (such as ULP) are a new, low-cost, neutral gel electrolyte and can promote the application of V-based materials in supercapacitors, which is worthy of reference and development. Meanwhile, the pH value of the electrolyte can affect the structure of V-based electrode materials, resistivity and proton transmission rates, and even pollute the environment. Therefore, it is still challenging and important to study the optimal pH in subsequent studies.

Lastly, in the research process of V-based materials, advanced characterization techniques are rarely mentioned. In order to understand the changes in the morphologies of V-based materials during the electrochemical process and enhance the understanding of its mechanism, advanced characterization techniques should be used.

In short, V-based materials are still challenging for use in SCs, such as the application of pure  $V_2O_3$  and pure  $VS_4$ , synthesis mechanism of VNs, research of various vanadates, and so on. These problems should be studied and discussed in depth in the future. Nowadays, V-based materials have shown huge potential in practical applications. Although there are many problems, it can become a hot research area.

## Conflicts of interest

The authors declare no competing financial interest.

## Acknowledgements

This work is financially supported by the National Natural Science Foundation of China (No. 21101176 and 21676036), the Fundamental Research Funds for the Central Universities of Chongqing University (No. 2018CDQYCH0028, 2018CDXYHG0028 and 2019CDXYHG0013), the Graduate Research and Innovation Foundation of Chongqing (No. CYS18032), and the Large-scale Equipment Sharing Fund of Chongqing University (No. 201903150149 and 202003150020). S. W. C. thanks the National Science Foundation for partial support of the work (CHE-2003685 and CHE-1900235).

## References

- 1 T. Brousse, O. Crosnier, D. Bélanger and J. Long, in *Metal Oxides in Supercapacitors*, Elsevier, 2017, pp. 1–24.
- 2 D. Dubal, O. Ayyad, V. Ruiz and P. Gomez-Romero, *Chem. Soc. Rev.*, 2015, **44**, 1777–1790.
- 3 M. Wu, J. Gao, S. Zhang and A. Chen, *J. Porous Mat.*, 2006, **13**, 407–412.
- 4 H. Hwang, D. Shin, T. Kim, S. Park, T. Yeo and W. Choi, *J. Mater. Chem. A*, 2018, **6**, 22998–23009.
- 5 C. Zhong, Y. Deng, W. Hu, J. Qiao, L. Zhang and J. Zhang, *Chem. Soc. Rev.*, 2015, **44**, 7484–7539.
- 6 M. Yu, Z. Wang, Y. Han, Y. Tong, X. Lu and S. Yang, *J. Mater. Chem. A*, 2016, **4**, 4634–4658.
- 7 X. Zhao, L. Mao, Q. Cheng, J. Li, F. Liao, G. Yang, L. Xie, C. Zhao and L. Chen, *Chem. Eng. J.*, 2020, **387**, 124081.
- 8 J. Theerthagiri, R. Senthil, P. Nithyadharseni, S. Lee, G. Durai, P. Kuppusami, J. Madhavan and M. Choi, *Ceram. Int.*, 2020, **46**, 14317–14345.
- 9 J. Shi, B. Jiang, C. Li, F. Yan, D. Wang, C. Yang and J. Wan, *Mater. Chem. Phys.*, 2020, **245**, 122533.
- 10 M. Manikandan, K. Subramani, M. Sathish and S. Dhanuskodi, *RSC Adv.*, 2020, **10**, 13632–13641.
- 11 C. Zhao, X. Jia, K. Shu, C. Yu, G. Wallace and C. Wang, *J. Mater. Chem. A*, 2020, **8**, 4677–4699.
- 12 J. Yin, W. Zhang, N. Alhebshi, N. Salah and H. Alshareef, *Small Methods*, 2020, **4**, 1900853.
- 13 S. Vijayakumar, S. Lee and K. Ryu, *RSC Adv.*, 2015, **5**, 91822–91828.
- 14 W. Wang, B. Jiang, L. Hu, Z. Lin, J. Hou and S. Jiao, *J. Power Sources*, 2014, **250**, 181–187.
- 15 C. Wu, F. Feng and Y. Xie, *Chem. Soc. Rev.*, 2013, **42**, 5157–5183.
- 16 D. Wegkamp and J. Staehler, *Prog. Surf. Sci.*, 2015, **90**, 464–502.
- 17 C. Armer, J. Yeoh, X. Li and A. Lowe, *J. Power Sources*, 2018, **395**, 414–429.
- 18 N. Chernova, M. Roppolo, A. Dillon and M. Whittingham, *J. Mater. Chem.*, 2009, **19**, 2526–2552.
- 19 E. Kianfar, *Microchem. J.*, 2019, **145**, 966–978.
- 20 Y. Wang and G. Cao, *Chem. Mater.*, 2006, **18**, 2787–2804.
- 21 R. Franz and C. Mitterer, *Surf. Coat. Technol.*, 2013, **228**, 1–13.
- 22 B. Gao, X. Li, K. Ding, C. Huang, Q. Li, P. Chu and K. Huo, *J. Mater. Chem. A*, 2019, **7**, 14–37.
- 23 V. Sharygin, G. Ripp, G. Yakovlev, Y. Seryotkin, N. Karmanov, I. Izbrodin, V. Grokhovsky and E. Khromova, *Minerals*, 2020, **10**, 1–19.
- 24 Y. Zhong, X. Xia, F. Shi, J. Zhan, J. Tu and H. Fan, *Adv. Sci.*, 2017, **4**, 1500286.
- 25 X. Xu, F. Xiong, J. Meng, X. Wang, C. Niu, Q. An and L. Mai, *Adv. Funct. Mater.*, 2020, **30**, 1904398.
- 26 Q. Wang, K. Kalantar-Zadeh, A. Kis, J. Coleman and M. Strano, *Nat. Nanotechnol.*, 2012, **7**, 699.
- 27 C. Rout, B. Kim, X. Xu, J. Yang, H. Jeong, D. Odkhuu, N. Park, J. Cho and H. Shin, *J. Am. Chem. Soc.*, 2013, **135**, 8720–8725.
- 28 H. Fuess, E. Bertaut, R. Pauthenet and A. Durif, *Acta Crystallogr., Sect. B: Struct. Crystallogr. Cryst. Chem.*, 1970, **26**, 2036–2046.

- 29 J. Xie, P. Yang, Y. Wang, T. Qi, Y. Lei and C. Li, *J. Power Sources*, 2018, **401**, 213–223.
- 30 R. Devan, R. Patil, J. Lin and Y. Ma, *Adv. Funct. Mater.*, 2012, **22**, 3326–3370.
- 31 R. Rakhi, D. Nagaraju, P. Beaujuge and H. Alshareef, *Electrochim. Acta*, 2016, **220**, 601–608.
- 32 Y. Zhang, X. Jing, Y. Cheng, T. Hu and C. Meng, *Inorg. Chem. Front.*, 2018, **5**, 2798–2810.
- 33 T. Hu, Y. Liu, Y. Zhang, Y. Nie, J. Zheng, Q. Wang, H. Jiang and C. Meng, *Microporous Mesoporous Mater.*, 2018, **262**, 199–206.
- 34 X. Lu, M. Yu, T. Zhai, G. Wang, S. Xie, T. Liu, C. Liang, Y. Tong and Y. Li, *Nano Lett.*, 2013, **13**, 2628–2633.
- 35 Z. Zhang, X. Huang, H. Wang, S. Teo and T. Ma, *J. Alloys Compd.*, 2019, **771**, 274–280.
- 36 B. Huang, W. Wang, T. Pu, J. Li, C. Zhao, L. Xie and L. Chen, *Chem. Eng. J.*, 2019, **375**, 121969.
- 37 J. Nag and R. Haglund Jr, *J. Phys.: Condens. Matter*, 2008, **20**, 264016.
- 38 R. Kiruthiga, C. Nithya and R. Karvembu, *Electrochim. Acta*, 2017, **256**, 221–231.
- 39 Y. Wu, G. Gao, H. Yang, W. Bi, X. Liang, Y. Zhang, G. Zhang and G. Wu, *J. Mater. Chem. A*, 2015, **3**, 15692–15699.
- 40 A. Mauger and C. Julien, *AIMS Mater. Sci.*, 2018, **5**, 349–401.
- 41 R. Basu, S. Ghosh, S. Bera, A. Das and S. Dhara, *Sci. Rep.*, 2019, **9**, 1–11.
- 42 L. Yu, Y. Yi, T. Yao, Y. Song, Y. Chen, Q. Li, Z. Xia, N. Wei, Z. Tian, B. Nie, L. Zhang, Z. Liu and J. Sun, *Nano Res.*, 2019, **12**, 331–338.
- 43 G. Wee, H. Soh, Y. Cheah, S. Mhaisalkar and M. Srinivasan, *J. Mater. Chem.*, 2010, **20**, 6720–6725.
- 44 N. Ndiaye, T. Masikhwa, B. Ngom, M. Madito, K. Oyedotun, J. Dangbegnon and N. Manyala, *Mater. Chem. Phys.*, 2018, **214**, 192–200.
- 45 N. Ndiaye, M. Madito, B. Ngom, T. Masikhwa, A. Mirghni and N. Manyala, *AIP Adv.*, 2019, **9**, 1–9.
- 46 I. Reddy, A. Sreedhar, J. Shim and J. S. Gwag, *J. Electroanal. Chem.*, 2019, **835**, 40–47.
- 47 S. Fleischmann, M. Zeiger, N. Jaekel, B. Kruener, V. Lemkova, M. Widmaier and V. Presser, *J. Mater. Chem. A*, 2017, **5**, 13039–13051.
- 48 S. Kaipannan, K. Govindarajan, S. Sundaramoorthy and S. Marappan, *ACS Omega*, 2019, **4**, 15798–15805.
- 49 M. Ates, M. Yildirim, O. Kuzgun and H. Ozkan, *J. Alloys Compd.*, 2019, **787**, 851–864.
- 50 S. Shuang, L. Girardi, G. Rizzi, A. Sartorel, C. Marega, Z. Zhang and G. Granozzi, *Nanomaterials*, 2018, **8**, 544.
- 51 Y. Zhang, J. Zheng, T. Hu, F. Tian and C. Meng, *Appl. Surf. Sci.*, 2016, **371**, 189–195.
- 52 J. Wang, X. Zhang, Y. Zhang, A. Abas, X. Zhao, Z. Yang, Q. Su, W. Lan and E. Xie, *RSC Adv.*, 2017, **7**, 35558–35564.
- 53 W. Lv, C. Yang, G. Meng, R. Zhao, A. Han, R. Wang and J. Liu, *Sci. Rep.*, 2019, **9**, 1–8.
- 54 G. Ren, R. Zhang and Z. Fan, *Appl. Surf. Sci.*, 2018, **441**, 466–473.
- 55 X. Xia, D. Chao, C. Ng, J. Lin, Z. Fan, H. Zhang, Z. Shen and H. Fan, *Mater. Horiz.*, 2015, **2**, 237–244.
- 56 Y. Fan, D. Ouyang, B. Li, F. Dang and Z. Ren, *Nanoscale Res. Lett.*, 2018, **13**, 1–8.
- 57 X. Pan, Y. Zhao, G. Ren and Z. Fan, *Chem. Commun.*, 2013, **49**, 3943–3945.
- 58 M. Yu, Y. Zeng, Y. Han, X. Cheng, W. Zhao, C. Liang, Y. Tong, H. Tang and X. Lu, *Adv. Funct. Mater.*, 2015, **25**, 3534–3540.
- 59 G. Wang, X. Lu, Y. Ling, T. Zhai, H. Wang, Y. Tong and Y. Li, *ACS Nano*, 2012, **6**, 10296–10302.
- 60 X. Li, J. Fu, Z. Pan, J. Su, J. Xu, B. Gao, X. Peng, L. Wang, X. Zhang and P. Chu, *J. Power Sources*, 2016, **331**, 58–66.
- 61 X. Liu, R. Liu, L. Zeng, X. Huang, X. Chen, C. Zheng, Y. Xu, Q. Qian, M. Wei and Q. Chen, *New J. Chem.*, 2017, **41**, 5380–5386.
- 62 J. Zheng, Y. Zhang, X. Jing, X. Liu, T. Hu, T. Lv, S. Zhang and C. Meng, *Colloids Surf., A*, 2017, **518**, 188–196.
- 63 X. Zhang, Z. Bu, R. Xu, B. Xie and H. Li, *Funct. Mater. Lett.*, 2017, **10**, 1750077.
- 64 J. Zheng, Y. Zhang, C. Meng, X. Wang, C. Liu, M. Bo, X. Pei, Y. Wei, T. Lv and G. Cao, *Electrochim. Acta*, 2019, **318**, 635–643.
- 65 Z. Hou, Z. Wang, L. Yang and Z. Yang, *RSC Adv.*, 2017, **7**, 25732–25739.
- 66 B. Saravanakumar, K. Purushothaman and G. Muralidharan, *ACS Appl. Mater. Interfaces*, 2012, **4**, 4484–4490.
- 67 J. Yang, T. Lan, J. Liu, Y. Song and M. Wei, *Electrochim. Acta*, 2013, **105**, 489–495.
- 68 A. Qian, K. Zhuo, M. Shin, W. Chun, B. Choi and C. Chung, *ChemSusChem*, 2015, **8**, 2399–2406.
- 69 Y. Liu, M. Clark, Q. Zhang, D. Yu, D. Liu, J. Liu and G. Cao, *Adv. Energy Mater.*, 2011, **1**, 194–202.
- 70 M. Deng, L. Yeh, Y. Lin, J. Chen and T. Chou, *ACS Appl. Mater. Interfaces*, 2019, **11**, 29838–29848.
- 71 B. Pandit, D. Dubal and B. Sankapal, *Electrochim. Acta*, 2017, **242**, 382–389.
- 72 Y. Shao, M. El-Kady, J. Sun, Y. Li, Q. Zhang, M. Zhu, H. Wang, B. Dunn and R. Kaner, *Chem. Rev.*, 2018, **118**, 9233–9280.
- 73 N. Choudhary, C. Li, J. Moore, N. Nagaiyah, L. Zhai, Y. Jung and J. Thomas, *Adv. Mater.*, 2017, **29**, 1605336.
- 74 Z. Liu, H. Zhang, Q. Yang and Y. Chen, *Electrochim. Acta*, 2018, **287**, 149–157.
- 75 A. Choudhury, J. Bonso, M. Wunch, K. Yang, J. Ferraris and D. Yang, *J. Power Sources*, 2015, **287**, 283–290.
- 76 L. Yao, C. Zhang, N. Hu, L. Zhang, Z. Zhou and Y. Zhang, *Electrochim. Acta*, 2019, **295**, 14–21.
- 77 D. Nagaraju, Q. Wang, P. Beaujuge and H. Alshareef, *J. Mater. Chem. A*, 2014, **2**, 17146–17152.
- 78 G. Yilmaz, X. Lu and G. Ho, *Nanoscale*, 2017, **9**, 802–811.
- 79 H. Ghaly, A. El-Deen, E. Souaya and N. Allam, *Electrochim. Acta*, 2019, **310**, 58–69.
- 80 C. Foo, A. Sumboja, D. Tan, J. Wang and P. Lee, *Adv. Energy Mater.*, 2014, **4**, 1400236.
- 81 S. Balasubramanian and K. Purushothaman, *Electrochim. Acta*, 2015, **186**, 285–291.

- 82 C. Zhu, D. Hu and Z. Liu, *Electrochim. Acta*, 2017, **229**, 155–165.
- 83 M. Tian, R. Li, C. Liu, D. Long and G. Cao, *ACS Appl. Mater. Interfaces*, 2019, **11**, 15573–15580.
- 84 Z. Chen, V. Augustyn, J. Wen, Y. Zhang, M. Shen, B. Dunn and Y. Lu, *Adv. Mater.*, 2011, **23**, 791–795.
- 85 B. Kim, C. Kim, K. Yang, A. Rahy and D. Yang, *Electrochim. Acta*, 2012, **83**, 335–340.
- 86 I. Shakir, Z. Ali, J. Bae, J. Park and D. Kang, *Nanoscale*, 2014, **6**, 4125–4130.
- 87 D. Kim, J. Yun, G. Lee and J. Ha, *Nanoscale*, 2014, **6**, 12034–12041.
- 88 W. Sun, G. Gao, K. Zhang, Y. Liu and G. Wu, *Carbon*, 2018, **132**, 667–677.
- 89 W. Sun, G. Gao, Y. Du, K. Zhang and G. Wu, *J. Mater. Chem. A*, 2018, **6**, 9938–9947.
- 90 T. Qian, N. Xu, J. Zhou, T. Yang, X. Liu, X. Shen, J. Liang and C. Yan, *J. Mater. Chem. A*, 2015, **3**, 488–493.
- 91 J. Wang, H. Liu, H. Liu, W. Hua and M. Shao, *ACS Appl. Mater. Interfaces*, 2018, **10**, 18816–18823.
- 92 W. Bi, J. Huang, M. Wang, E. Jahrman, G. Seidler, J. Wang, Y. Wu, G. Gao, G. Wu and G. Cao, *J. Mater. Chem. A*, 2019, **7**, 17966–17973.
- 93 M. Zhi, C. Xiang, J. Li, M. Li and N. Wu, *Nanoscale*, 2013, **5**, 72–88.
- 94 A. Lo, Y. Jheng, T. Huang and C. Tseng, *Appl. Energy*, 2015, **153**, 15–21.
- 95 Y. Huang, Y. Li, Z. Hu, G. Wei, J. Guo and J. Liu, *J. Mater. Chem. A*, 2013, **1**, 9809–9813.
- 96 Y. Zhang, Y. Zhao, S. Cao, Z. Yin, L. Cheng and L. Wu, *ACS Appl. Mater. Interfaces*, 2017, **9**, 29982–29991.
- 97 T. Sun, Z. Li, X. Liu, L. Ma, J. Wang and S. Yang, *J. Power Sources*, 2017, **352**, 135–142.
- 98 J. Xu, F. Zheng, C. Xi, Y. Yu, L. Chen, W. Yang, P. Hu, Q. Zhen and S. Bashir, *J. Power Sources*, 2018, **404**, 47–55.
- 99 Y. Yang, D. Kim, M. Yang and P. Schmuki, *Chem. Commun.*, 2011, **47**, 7746–7748.
- 100 G. Nie, X. Lu, J. Lei, Z. Jiang and C. Wang, *J. Mater. Chem. A*, 2014, **2**, 15495–15501.
- 101 X. Wang, B. Shi, X. Wang, J. Gao, C. Zhang, Z. Yang and H. Xie, *J. Mater. Chem. A*, 2017, **5**, 23543–23549.
- 102 X. Zhong, L. Zhang, J. Tang, J. Chai, J. Xu, L. Cao, M. Yang, M. Yang, W. Kong and S. Wang, *J. Mater. Chem. A*, 2017, **5**, 17954–17962.
- 103 R. Manikandan, C. Raj, M. Rajesh, B. Kim, S. Park, B. Cho and K. Yu, *Electrochim. Acta*, 2017, **230**, 492–500.
- 104 M. Jayalakshmi, M. Rao, N. Venugopal and K. Kim, *J. Power Sources*, 2007, **166**, 578–583.
- 105 C. Guo, G. Yilmaz, S. Chen, S. Chen and X. Lu, *Nano Energy*, 2015, **12**, 76–87.
- 106 A. Glushenkov, D. Hulicova-Jurcakova, D. Llewellyn, G. Lu and Y. Chen, *Chem. Mater.*, 2010, **22**, 914–921.
- 107 A. Djire, P. Pande, A. Deb, J. Siegel, O. Ajenifujah, L. He, A. Sleightholme, P. Rasmussen and L. Thompson, *Nano Energy*, 2019, **60**, 72–81.
- 108 D. Zhang, J. Li, Z. Su, S. Hu, H. Li and Y. Yan, *J. Adv. Ceram.*, 2018, **7**, 246–255.
- 109 F. Ran, Z. Wang, Y. Yang, Z. Liu, L. Kong and L. Kang, *Electrochim. Acta*, 2017, **258**, 405–413.
- 110 W. Zhang, Y. Yang, M. Ravi, L. Kong, L. Kang and F. Ran, *Electrochim. Acta*, 2019, **306**, 113–121.
- 111 Q. Li, Y. Chen, J. Zhang, W. Tian, L. Wang, Z. Ren, X. Ren, X. Li, B. Gao, X. Peng, P. Chu and K. Huo, *Nano Energy*, 2018, **51**, 128–136.
- 112 N. Ouldhamadouche, A. Achour, R. Lucio-Porto, M. Islam, S. Solaymani, A. Arman, A. Ahmadpourian, H. Achour, L. Le Brizoual, M. Djouadi and T. Brousse, *J. Mater. Sci. Technol.*, 2018, **34**, 976–982.
- 113 J. Zhao, C. Li, Q. Zhang, J. Zhang, X. Wang, Z. Lin, J. Wang, W. Lv, C. Lu, C. Wong and Y. Yao, *J. Mater. Chem. A*, 2017, **5**, 6928–6936.
- 114 Y. Su and I. Zhitomirsky, *J. Power Sources*, 2014, **267**, 235–242.
- 115 C. Ghimbeu, E. Raymundo-Pinero, P. Fioux, F. Beguin and C. Vix-Guterl, *J. Mater. Chem.*, 2011, **21**, 13268–13275.
- 116 G. An, D. Lee and H. Ahn, *J. Mater. Chem. A*, 2017, **5**, 19714–19720.
- 117 Q. Zhang, X. Wang, Z. Pan, J. Sun, J. Zhao, J. Zhang, C. Zhang, L. Tang, J. Luo, B. Song, Z. Zhang, W. Lu, Q. Li, Y. Zhang and Y. Yao, *Nano Lett.*, 2017, **17**, 2719–2726.
- 118 X. Jiang, W. Lu, Y. Li, Y. Yu, X. Zhou, X. Liu and Y. Xing, *ChemElectroChem*, 2019, **6**, 3445–3453.
- 119 T. He, Z. Wang, X. Li, Y. Tan, Y. Liu, L. Kong, L. Kang, C. Chen and F. Ran, *J. Alloys Compd.*, 2019, **781**, 1054–1058.
- 120 J. Liu, F. Li, W. Liu and X. Li, *Inorg. Chem. Front.*, 2019, **6**, 164–171.
- 121 J. Balamurugan, G. Karthikeyan, T. Tran Duy, N. Kim and J. Lee, *J. Power Sources*, 2016, **308**, 149–157.
- 122 C. Ji, J. Bi, S. Wang, X. Zhanga and S. Yang, *J. Mater. Chem. A*, 2016, **4**, 2158–2168.
- 123 X. Jiang, W. Lu, Y. Yu, M. Yang, X. Liu and Y. Xing, *Electrochim. Acta*, 2019, **302**, 385–393.
- 124 X. Zhou, C. Shang, L. Gu, S. Dong, X. Chen, P. Han, L. Li, J. Yao, Z. Liu, H. Xu, Y. Zhu and G. Cui, *ACS Appl. Mater. Interfaces*, 2011, **3**, 3058–3063.
- 125 B. Wei, C. Shang, L. Shui, X. Wang and G. Zhou, *Mater. Res. Express*, 2019, **6**, 025801.
- 126 B. Pandit, L. Bommeneedi and B. Sankapal, *J. Energy Chem.*, 2019, **31**, 79–88.
- 127 J. Feng, X. Sun, C. Wu, L. Peng, C. Lin, S. Hu, J. Yang and Y. Xie, *J. Am. Chem. Soc.*, 2011, **133**, 17832–17838.
- 128 Z. Guo, L. Yang, W. Wang, L. Cao and B. Dong, *J. Mater. Chem. A*, 2018, **6**, 14681–14688.
- 129 P. Zhang, L. Wang, F. Wang, D. Tan, G. Wang, S. Yang, M. Yu, J. Zhang and X. Feng, *Batteries Supercaps*, 2019, **2**, 918–923.
- 130 L. Fang, Z. Zhang, X. Li, H. Zhou, K. Ma, L. Ge and K. Huang, *Colloids Surf., A*, 2016, **501**, 42–48.
- 131 X. Wang, Y. Zhang, J. Zheng, X. Liu and C. Meng, *J. Colloid Interface Sci.*, 2019, **554**, 191–201.
- 132 S. Ratha, S. Marri, N. Lanzillo, S. Moshkalev, S. Nayak, J. Behera and C. Rout, *J. Mater. Chem. A*, 2015, **3**, 18874–18881.

- 133 S. Ratha, S. Marri, J. Behera and C. Rout, *Eur. J. Inorg. Chem.*, 2016, 259–265.
- 134 M. Ramu, J. Chellan, N. Goli, P. Joaquim, V. Cristobal and B. Kim, *Adv. Funct. Mater.*, 2020, **30**, 1906586.
- 135 S. Wang, Y. Song, Y. Ma, Z. Zhu, C. Zhao and C. Zhao, *Chem. Eng. J.*, 2019, **365**, 88–98.
- 136 H. Sun, X. Chen, H. Chai, Y. Wang, D. Jia, Y. Cao and A. Liu, *Appl. Surf. Sci.*, 2019, **469**, 118–124.
- 137 Y. Teng, Y. Li, D. Yu, Y. Meng, Y. Wu, X. Zhao and X. Liu, *ChemistrySelect*, 2019, **4**, 956–962.
- 138 M. Liu, L. Kong, L. Kang, X. Li, F. Walsh, M. Xing, C. Lu, X. Ma and Y. Luo, *J. Mater. Chem. A*, 2014, **2**, 4919–4926.
- 139 W. Zhang, L. Kong, X. Ma, Y. Luo and L. Kang, *J. Power Sources*, 2014, **269**, 61–68.
- 140 M. Guo, J. Balamurugan, N. Kim and J. Lee, *Appl. Catal., B*, 2018, **239**, 290–299.
- 141 R. Kumar, P. Rai and A. Sharma, *J. Mater. Chem. A*, 2016, **4**, 9822–9831.
- 142 R. Kumar, T. Bhuvana, P. Rai and A. Sharma, *J. Electrochem. Soc.*, 2018, **165**, B1–B8.
- 143 X. Liu, J. Wang and G. Yang, *ACS Appl. Mater. Interfaces*, 2018, **10**, 20688–20695.
- 144 P. Vishnukumar, B. Saravanakumar, G. Ravi, V. Ganesh, R. Guduru and R. Yuvakkumar, *Mater. Lett.*, 2018, **219**, 114–118.
- 145 S. Zhao, K. Tao and Y. Gong, *Dalton Trans.*, 2019, **48**, 5315–5326.
- 146 H. Hosseini and S. Shahrokhian, *Chem. Eng. J.*, 2018, **341**, 10–26.
- 147 L. Pei, N. Lin, T. Wei, H. Liu and H. Yu, *J. Alloys Compd.*, 2015, **631**, 90–98.
- 148 F. Butt, C. Cao, F. Idrees, M. Tahir, R. Hussain, R. Ahmed and W. Khan, *Int. J. Hydrogen Energy*, 2015, **40**, 9359–9364.
- 149 S. Pitale, M. Gohain, I. Nagpure, O. Ntwaeaborwa, B. Bezuidenhout and H. Swart, *Phys. B*, 2012, **407**, 1485–1488.
- 150 S. Ni, S. Lin, Q. Pan, K. Huang, F. Yang and D. He, *J. Alloys Compd.*, 2009, **477**, L1–L3.
- 151 Y. Li, Y. Teng, Z. Zhang, Y. Feng, P. Xue, W. Tong and X. Liu, *New J. Chem.*, 2017, **41**, 15298–15304.
- 152 W. Low, P. Khiew, S. Lim, C. Siong, C. Chia and E. Ezeigwe, *J. Alloys Compd.*, 2019, **784**, 847–858.
- 153 R. Packiaraj, P. Devendran, S. Bahadur and N. Nallamuthu, *J. Mater. Sci.: Mater. Electron.*, 2018, **29**, 13265–13276.
- 154 L. Deng, J. Liu, Z. Ma, G. Fan and Z. Liu, *RSC Adv.*, 2018, **8**, 24796–24804.
- 155 S. Patil, D. Dubal, V. Deonikar, M. Tamboli, J. Ambekar, P. Gomez-Romero, S. Kolekar, B. Kale and D. Patil, *ACS Appl. Mater. Interfaces*, 2016, **8**, 31602–31610.
- 156 Y. Yan, H. Xu, W. Guo, Q. Huang, M. Zheng, H. Pang and H. Xue, *Inorg. Chem. Front.*, 2016, **3**, 791–797.
- 157 F. Yu, T. Huang, P. Zhang, Y. Tao, F. Cui, Q. Xie, S. Yao and F. Wang, *Energy Storage Mater.*, 2019, **22**, 235–255.
- 158 F. Wang, Z. Liu, X. Yuan, J. Mo, C. Li, L. Fu, Y. Zhu, X. Wu and Y. Wu, *J. Mater. Chem. A*, 2017, **5**, 14922–14929.
- 159 D. Zhao, Q. Zhu, D. Chen, X. Li, Y. Yu and X. Huang, *J. Mater. Chem. A*, 2018, **6**, 16475–16484.
- 160 H. Zeng, Y. Zhao, Y. Hao, Q. Lai, J. Huang and X. Ji, *J. Alloys Compd.*, 2009, **477**, 800–804.
- 161 T. Zhai, X. Lu, Y. Ling, M. Yu, G. Wang, T. Liu, C. Liang, Y. Tong and Y. Li, *Adv. Mater.*, 2014, **26**, 5869–5875.
- 162 Z. Luo, E. Liu, T. Hu, Z. Li and T. Liu, *Ionics*, 2015, **21**, 289–294.
- 163 N. Chen, J. Zhou, Q. Kang, H. Ji, G. Zhu, Y. Zhang, S. Chen, J. Chen, X. Feng and W. Hou, *J. Power Sources*, 2017, **344**, 185–194.
- 164 C. Wu, X. Lu, L. Peng, K. Xu, X. Peng, J. Huang, G. Yu and Y. Xie, *Nat. Commun.*, 2013, **4**, 1–7.
- 165 Y. He, X. Yang, Y. Bai, J. Zhang, L. Kang, Z. Lei and Z. Liu, *Electrochim. Acta*, 2015, **178**, 312–320.
- 166 N. Chen, J. Zhou, G. Zhu, Q. Kang, H. Ji, Y. Zhang, X. Wang, L. Peng, X. Guo, C. Lu, J. Chen, X. Feng and W. Hou, *Nanoscale*, 2018, **10**, 3709–3719.
- 167 Y. Dall'Agnese, P. Taberna, Y. Gogotsi and P. Simon, *J. Phys. Chem. Lett.*, 2015, **6**, 2305–2309.